Volume 10 | Number 5 | 2 March 2026

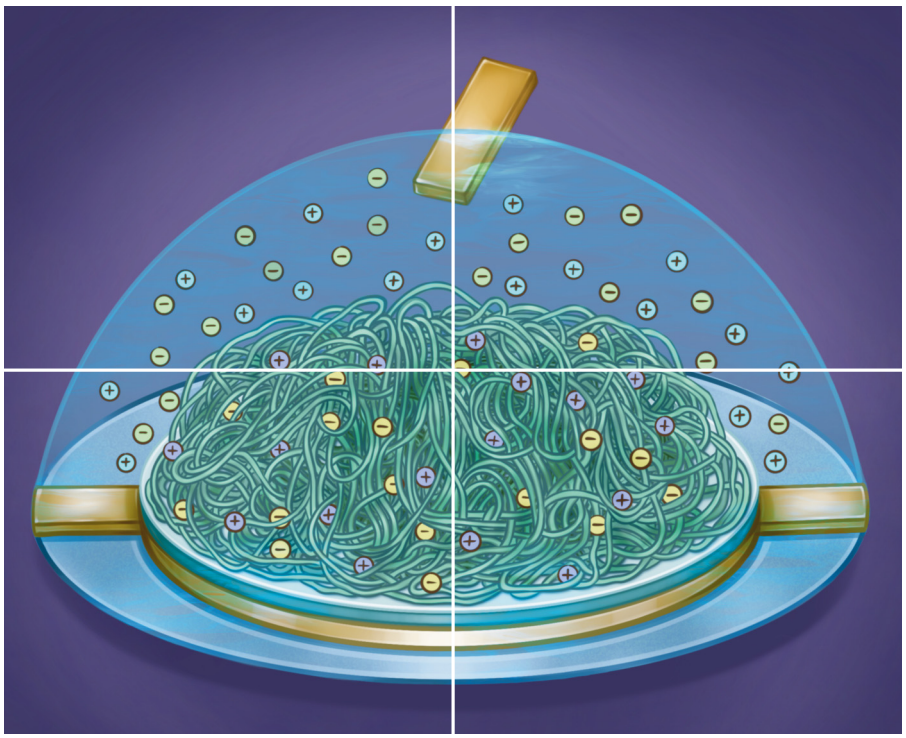

MATERIALS CHEMISTRY

FRONTIERS

CCS 中国化学会 CHINESE CHEMICAL SOCIETY
ICCAS 1956
ROYAL SOCIETY OF CHEMISTRY
rsc.li/frontiers-materials

MATERIALS CHEMISTRY FRONTIERS

REVIEW

View Article Online
View Journal | View Issue

Cite this: *Mater. Chem. Front.*, 2026, **10**, 694

Electrochemical QCM-D for insights into organic mixed ionic–electronic conductors and transistors (OECTs)

Nikolay Mukhin, [a] Andreas Dietzel, [b] Vadim Issakov[a] and Liubov Bakhchova*[a]

Recent progress in the synthesis of high-performance organic mixed ionic–electronic (semi)conductors (OMIECs) has given impetus to the development of organic electrochemical transistors (OECTs), which are key components for next-generation bioelectronics, neuromorphic devices, and flexible sensors. To ensure operational stability and enhanced performance of OECTs, it is essential to gain insight into the internal processes occurring within the transistor layers during electrochemical doping/de-doping, including mass exchange between the OMIEC and the electrolyte, interaction of the OECT channel with the substrate, its morphological changes, and so on. One method to address this problem *in situ* is an electrochemical quartz microbalance with dissipation monitoring (EQCM-D). This review aims to demonstrate how EQCM-D can facilitate the study of OMIECs and their interfacial interactions relevant to the operation and further development of OECT devices. EQCM-D allows real-time investigation of ion injection and charge carrier transport, water uptake, morphological changes and swelling (both passive and active), ion-to-electron coupling, the impact of oxygen reduction reactions, adhesion, degradation mechanisms, adsorption, OECT channel and gate electrode functionalisation, thereby shedding light on the mechanisms underlying electrochemical processes in the OMIEC–electrolyte system and OECT operation. This review unifies existing knowledge and offers guidance for effective use of EQCM-D, pointing to future interdisciplinary opportunities in OMIEC and OECT studies.

Received 21st October 2025,
Accepted 5th January 2026

DOI: 10.1039/d5qm00754b

rsc.li/frontiers-materials

1. Introduction

With major advances in the development of a new generation of high-performance organic mixed ionic–electronic (semi)conductors (OMIECs) in recent years,[1,2] the organic electrochemical transistor (OECT) is becoming a promising platform for bioelectronic[3,4] and biosensor[5,6] applications. OECTs exhibit outstanding transconductance values,[7] the highest among electrolyte-gated transistors,[8] record-high sensitivities,[5] excellent selectivity,[9] biocompatibility,[10] mechanical flexibility,[11] low-voltage operation,[12] and cost-effective fabrication.[9] However, at present, long-term operation stability remains one of the key factors limiting the widespread commercialisation of OECT devices.[13,14] Moreover, success in achieving high stability of OECTs is often accompanied by low efficiency in modulating the conductivity of their channel layer during the electrochemical doping/de-doping process,[15–17] and *vice versa*.[18] An additional limitation of OECTs is their low response time. Other challenges include trade-offs between transconductance and speed,[19] and between ionic charge accumulation effectiveness and high electron mobility of OMIECs.[20] Therefore, there is ongoing research into the design of new OMIEC materials and the modification of existing ones to simultaneously meet stringent requirements for electrical and dynamic performance as well as long-term stability.[18,21–23] Among OMIECs for OECTs, the largest number of works is devoted to the development of those types of conjugated polymers (CPs) that are capable of significant modulation of their conductivity with small injections of ions from the electrolyte;[24–26] also of interest is the development of alternatives to CPs, such as small organic molecule semiconductors (SOMSs),[27] CP-SOMS hybrids,[28] and organic–inorganic hybrids.[29]

At its core, from the point of view of typical electrical measurements, an OECT can be likened to a "black box" that transforms input electrical signals into output responses. While electrical measurements provide important information about device performance,[30,31] they offer limited insight into the intricate processes occurring within the transistor layers. Understanding the inner workings of OECTs requires complementary, *in situ* techniques. One such method is the electrochemical quartz crystal microbalance with dissipation monitoring (EQCM-D).[32,33]

[a] *Institute for CMOS Design, Technical University of Braunschweig, 38106 Braunschweig, Germany, liubov.bakhchova@tu-braunschweig.de*
[b] *Institute of Microtechnology, Technical University of Braunschweig, 38106 Braunschweig, Germany*

A quartz crystal microbalance (QCM) is a well-established, cost-effective, and highly sensitive mass sensor that operates on the principle of the piezoelectric effect. When an alternating voltage is applied to the quartz crystal, it oscillates at its resonance frequency. The resonance frequency shifts are proportional to small quartz surface mass changes, making the QCM a simple and powerful tool for measuring minute changes in mass at the sensor surface. Its modified version, the quartz crystal microbalance with dissipation monitoring (QCM-D), additionally provides information about the energy loss within the oscillating system, reflecting the viscoelastic properties of the deposited layers. This method is instrumental in understanding the behaviour of polymer films and complex biomolecular systems, both in the dry state and at the solid–liquid interface.[34,35] To study electrochemical processes during the interaction of thin organic films (particularly OMIECs) with electrolytes at the nanoscale, the EQCM-D technique is used.[30,34]

Under an applied electrical potential, ions and water molecules from the electrolyte are transported into and out of the OMIEC film, resulting in changes in its mass. These mass changes modulate the resonance frequency of the quartz crystal. The electrochemical activity and the associated morphological and relaxation changes of the organic layer are also reflected in the dissipation shift. By combining the QCM-D with the OECT setup, researchers can

Nikolay Mukhin

Nikolay Mukhin is a Researcher at the Institute of CMOS Design, Technical University of Braunschweig, Germany. He received the MSc degree in microelectronics and solid-state electronics in 2010, and the PhD degree in Physics in 2014 from Saint Petersburg Electrotechnical University, St.-Petersburg. From 2016 to 2023 he worked as a postdoc researcher at the Institute of Micro and Sensor Systems, Otto-von-Guericke-University Magdeburg, Germany. From 2022 to current he works as a researcher at the Technical University of Braunschweig, Germany. His research interests include bio- and chemosensors, metamaterials and composite structures, computer modelling of processes in solids and fluids. He has 50 scientific publications indexed in Scopus and 2 patents. Dr Mukhin is a Reviewer Board Member and a Guest Editor of Special Issue of Journal of Comp. Sci., and a Topical Advisory Panel Member of Crystals (Switzerland).

Andreas Dietzel

Andreas Dietzel is a Professor and Director of the Institute of Microtechnolgy at the Technical University of Braunschweig, Germany. He received the MSc degree in 1986, and the PhD degree in Physics in 1989 from Georg-August-Universität Göttingen, Germany. From 1989 to 1990 he was a post-doctoral researcher in the Institute for Medical Physics and Biophysics, Georg-August-Universität Göttingen, Germany. From 1990 to 1994 he was a Team leader of TEM Group IBM Microelectronics Division, Laboratory for Surface and Structural Analysis Sindelfingen. From 1994 to 1996 he was a Researcher of IBM Research Division, Zürich Research Laboratory Rüschlikon, Switzerland. From 1996 to 2003 he was a Department Manager of IBM Storage Technology Division, Laboratory for Analytics and Technology Projects, Mainz, Germany. From 2003 to 2004 he was a Project Coordination ''Basic development of inertial sensors of the 3rd generation'', Robert Bosch GmbH, Reutlingen. From 2004 to 2011 he was a Full Professor for Micro and Nano Scale Engeneering, Head of MNSE Section, TU Einhoven, Netherlands. From 2007 to 2011 he was a Program Manager of Holst Center TNO, Eindhoven Niederlande. Since 2012 he is a Chair (W3) of Institute of Microtechnolgy, Technische Universität Braunschweig, director of IMT. He is a Board Member ''PVZ'' (Center of Pharmaceutical Engineering) at the Technische Universität Braunschweig since its founding in May 2012. He is a Representative of the double degree programme between the TU Braunschweig and the Université de Technologie de Compiègne set within the German-French University Saarbrücken since 2012. He is a member of the professional association ''AMA-Fachverbandes für Sensorik e.V.'' since 2012. He is also a Reviewer for scientific journals (Sensors & Actuators, Journal of Microelectromechanical Systems, Journal of Applied Physics, Applied Physics A und Micro- and Nanofluidics et al.) and Program Committee Member of several international conferences (IEEE MEMS, Transducers, 3 M Nano et al.).

simultaneously monitor the electrical current and the dynamic changes in mass and dissipation at the OMIEC–electrolyte interface and within the OMIEC bulk under different OECT operating modes, defined by varying the gate voltage. This allows real-time investigation of ion penetration and water uptake,[36] passive and active swelling,[37] ion-to-electron coupling,[33] transient responses,[32] adhesion,[22] adsorption,[38] functionalisation,[39] the impact of oxygen reduction reactions (ORR),[40] and reversible and irreversible processes,[41] thereby shedding light on the working mechanisms of OECTs. Additionally, EQCM-D data can be correlated with OECT performance characteristics to optimize device operation. This knowledge aids in the design of tailored organic materials for improved OECT performance and stability.

The purpose of this review is to demonstrate how (E)QCM-D can facilitate the study of the behaviour of OMIEC materials and OECT components to support their further development.

2. Organic mixed ionic–electronic (semi)conductors for OECT applications: materials, characteristics and challenges

OMIECs enable simultaneous transport of electronic and ionic species. Their operation is governed by reversible electrochemical doping and de-doping processes that involve ionic

Vadim Issakov

Vadim Issakov is a Full Professor at the Institute of CMOS Design, Technical University of Braunschweig, Germany. He received the MSc degree in microwave engineering from the Technical University of Munich, Munich, Germany, in 2006, and the PhD degree (summa cum laude) from the University of Paderborn, Paderborn, Germany, in 2010. In March 2010, he joined Infineon Technologies AG, Neubiberg, Germany. Afterward, he was with imec, Leuven, Belgium, and Intel Corporation, Duisburg, Germany. In August 2015, he came back to Infineon Technologies AG as the Millimeter-Wave (mm-wave) Design Lead and a Lead Principal Engineer leading a research group working on predevelopment of mm-wave radar and communication products. Since 2014, he has been a Guest Lecturer with Ruhr University Bochum, Bochum, Germany, and the University of Erlangen-Nuremberg, Erlangen, Germany. In September 2019, he joined the University of Magdeburg, Magdeburg, Germany, as a Full Professor holding the Chair of Electronics. Since April 2021, he has been a Full Professor with the Technical University of Braunschweig, Braunschweig, Germany. He has authored or coauthored over 150 peer-reviewed articles and one book and holds 11 patents. His research interests include mm-wave circuits, RF systems, mm-wave measurement techniques, and radio-frequency electrostatic discharge (RF-ESD). Dr Issakov was a recipient of the 2010 University of Paderborn Best Dissertation Award, the 2011 VDI/VDE Distinguished Dissertation Award, and the 2019 IEEE MTT Outstanding Young Engineer Award. He currently serves on the Technical Program Committee for Symposium on Radio Frequency Integrated Circuits (RFIC) and Custom Integrated Circuits Conference (CICC). He served as an Associate Editor for IEEE Transactions on Microwave Theory and Techniques and Microwave and Wireless Components Letters (MWCL). He also serves as a Distinguished Lecturer for the IEEE Microwave Theory and Technique Society for the term of 2023–2025.

Liubov Bakhchova

Liubov Bakhchova is the Group Leader of ''Biomedical Systems'' at the Institute of CMOS Design, Technical University of Braunschweig, Germany. Liubov Bakhchova received her BSc and MSc degrees in material science for micro- and nanoelectronics from Kharkiv University of Technology, Ukraine, in 2017. She completed her PhD in electrical engineering at Otto-von-Guericke University Magdeburg, Germany, in 2023. During her PhD, she focused on engineering for biomedical applications and served as a research associate at the University Hospital Magdeburg for three years. Dr Bakhchova is currently a group leader of the ''Biomedical Systems'' research group at Braunschweig University of Technology, Germany. Her PhD research contributed to the development of Organ-on-chip systems, specifically in the integration of sensors to enhance functionality. Her current research interests include the integration of microfluidics, sensors, and electronics to develop advanced drug screening models. She is particularly focused on the microstructuring of conductive polymers, biosensor development, and the design of circuit elements.

exchange between the electrolyte and the OMIEC to maintain electroneutrality.[42–44] These processes are schematically illustrated in Fig. 1.

In Fig. 1, the top row illustrates the initial states of p-type and n-type OMIECs in the absence of any externally applied potential. The bottom row shows the modulation of OMIEC conductivity induced by the application of an appropriate potential, accompanied by the penetration of electrolyte ions into the bulk of the semiconducting film. The simplest electrochemical configuration consists of a two-electrode cell, in which an OMIEC-coated working electrode is immersed in an electrolyte and biased with respect to a counter electrode.

In p-type OMIECs operating in accumulation mode (Fig. 1a), electrochemical oxidation of the neutral state ($OMIEC^0$) results in the formation of hole carriers (h^+) and uptake of electrolyte anions (A^-) into the film (Fig. 1a), as in general can be described by the equilibrium:

$$OMIEC^0 + A^- + h^+ \leftrightarrow OMIEC^+A^-. \quad (1)$$

This p-doping process leads to an increase in hole concentration, enhancing the electronic conductivity of the film. The mode of operation can be either accumulation or depletion, depending on the initial doping state of the OMIEC. In accumulation mode, applying a potential difference between the electrodes enhances doping, further increasing conductivity. In contrast, in depletion mode, the OMIEC channel is initially doped and an applied bias drives de-doping, reducing conductivity (Fig. 1b).

N-type OMIECs, in contrast to the eqn (1), operate in accumulation mode through a reduction mechanism, described by:

$$OMIEC^0 + C^+ + e^- \leftrightarrow OMIEC^-C^+, \quad (2)$$

where electron (e^-) injection is compensated by cation (C^+) uptake from the electrolyte (Fig. 1c). This enables electron transport and n-type conduction. In accumulation mode, the applied potential-induced reduction introduces additional electrons and cations, increasing conductivity. In depletion mode, applied bias removes free electronic charge carriers from OMIEC bulk, suppressing conductivity.

The coupled electronic and ionic transport, enabling electrochemical modulation of charge carrier density throughout the bulk of the OMIEC materials, makes them particularly well suited for OECT-based sensors and bioelectronic applications. While Fig. 1 (bottom row) shows a simplified schematic of a

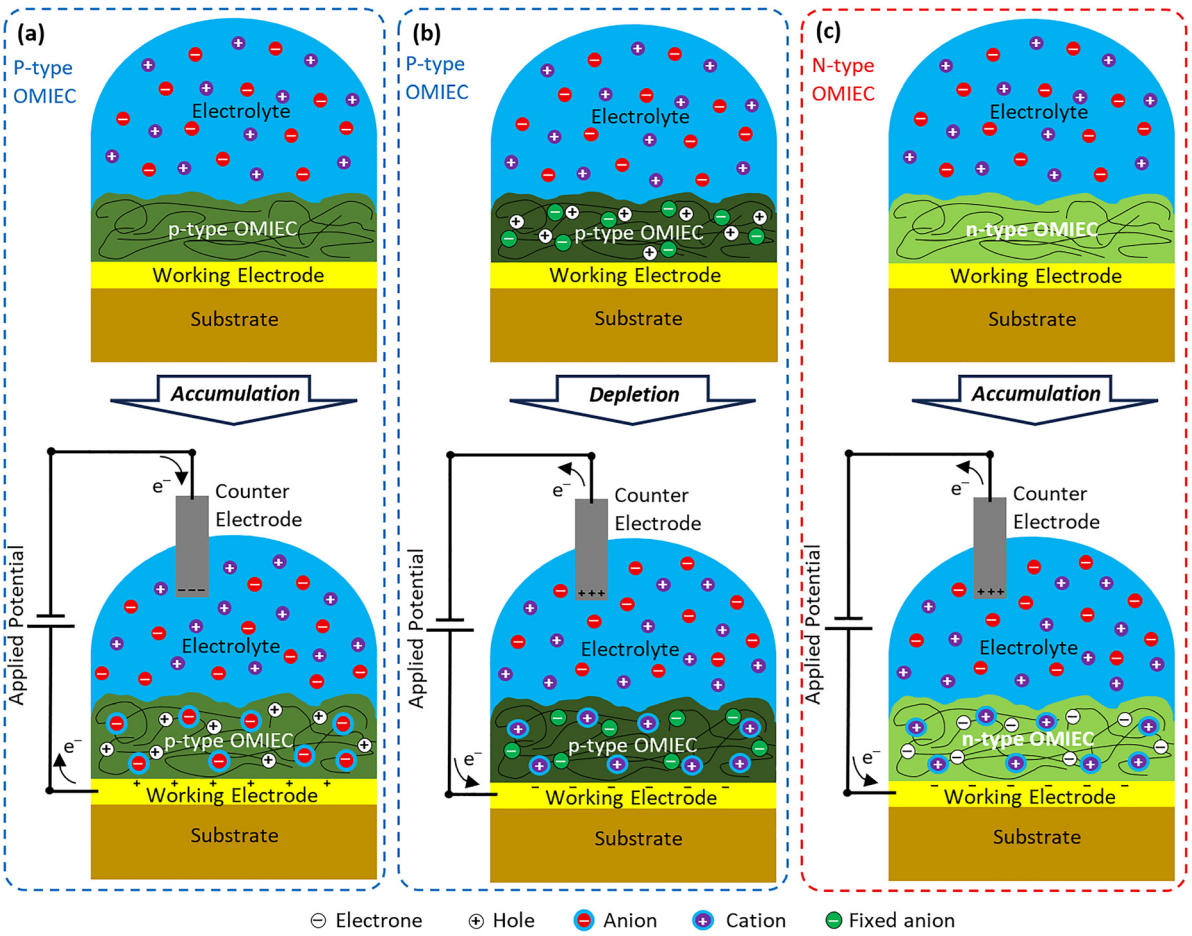

Fig. 1 Simplified schematic of electrochemical processes in an OMIEC–electrolyte system, illustrating ion penetration from the electrolyte into the OMIEC film and the resulting modulation of its conductivity under an applied potential for three cases: p-type OMIEC operating in accumulation mode (a), p-type OMIEC operating in depletion mode (b), and n-type OMIEC operating in accumulation mode (c).

two-electrode OMIEC–electrolyte configuration, commonly used to study fundamental ion–electron interactions in OMIECs, an OECT features three terminals: source, drain, and gate (Fig. 2a–c). The gate-source voltage controls the doping state of the OMIEC channel *via* ion exchange with the electrolyte. This doping modulation affects the channel conductivity and, consequently, changes the drain current, which is measured by applying a small voltage between source and drain. Fig. 2a–c schematically illustrate several common OECT architectures, though this list is not exhaustive. Fig. 2a depicts a planar OECT, where the channel lies laterally between the source and drain electrodes. Fig. 2b shows a vertical OECT configuration, in which a part of channel extends perpendicular to the substrate. Fig. 2c presents a vertical OECT with the channel sandwiched directly between the source and drain electrodes. OECTs utilise the electrochemical responses of OMIECs to achieve signal amplification and switching behaviour. The operation of an OECT is accompanied by a complex interplay of processes, including ion penetration from the electrolyte into the OMIEC film, electronic charge

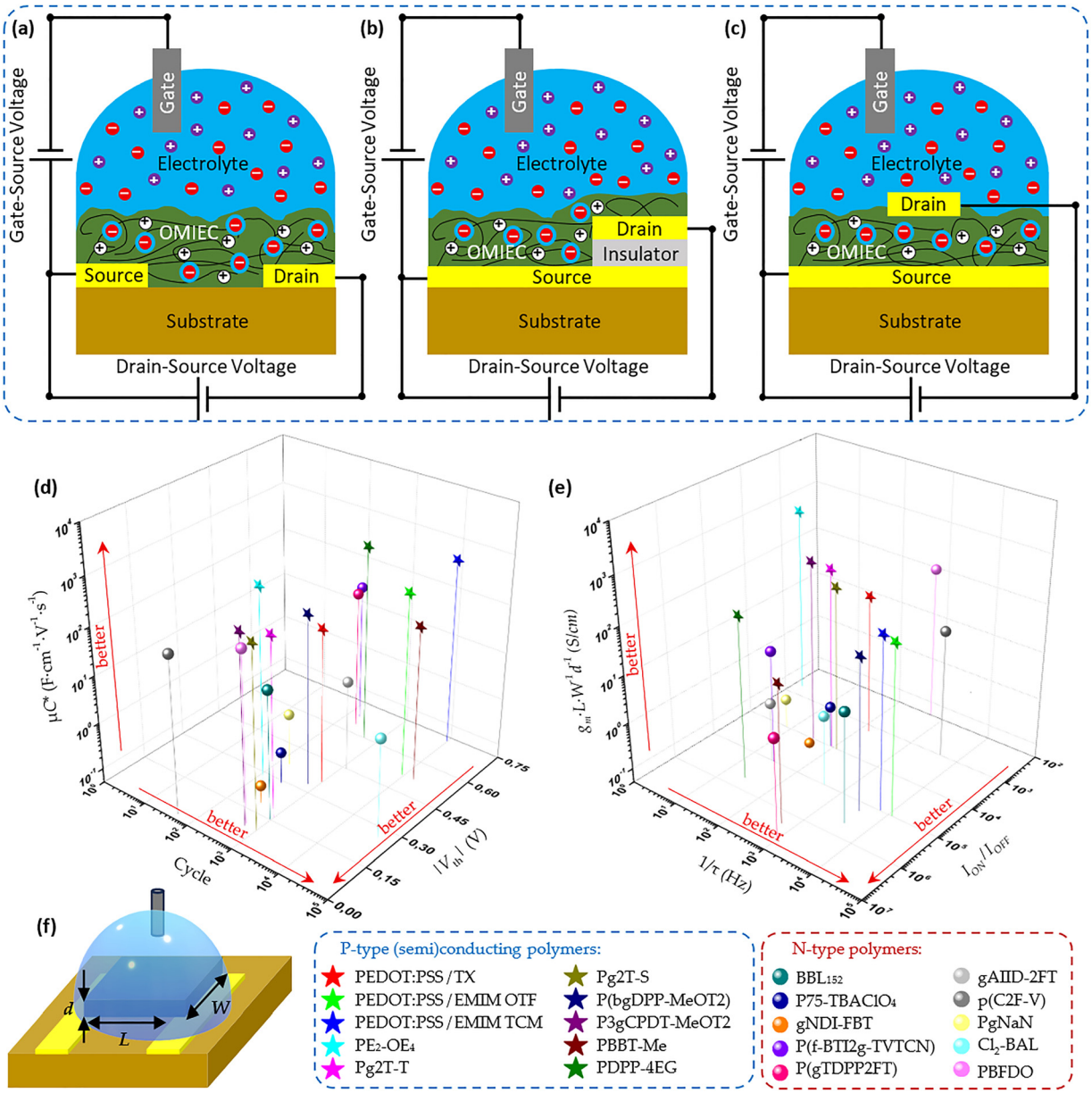

Fig. 2 Schematic illustrations of several possible OECT architectures (not exhaustive): planar OECT (a); vertical OECT (b); vertical OECT with the channel sandwiched between the source and drain electrodes (c). (Semi)conducting polymer materials and their characteristics for OECT application (d) and (e): electron mobility multiplied by volumetric capacitance (μC^*); number of switching cycles; absolute value of threshold voltage ($|V_{th}|$); inverse response time ($1/\tau$); on/off drain current ratio (I_{ON}/I_{OFF}), and normalized transconductance ($g_m L W^{-1} d^{-1}$), where g_m is transconductance, W is width, d is thickness, and L is length of OMIEC film (f). Diagrams (d) and (e) are plotted based on experimental data for p-type[50,53–59] and n-type[15,26,60–67] (semi)conducting polymers. The axes of the three-dimensional plots are oriented so that improvements in each parameter are directed towards the viewer. These directions of parameter improvement are shown by red arrows (d) and (e). For clarity, the corresponding numerical values are summarised in Table 1.

injection at the electrode–OMIEC interface,[23,45] electronic and ionic charge carrier transport within the OMIEC bulk,[43,46] ion-to-electron charges coupling,[47,48] OMIEC film morphology changes,[49,50] energy dissipation,[51] and chemical reactions involving the accumulation or removal of reaction products.[17,52] During electrochemical doping and de-doping, OMIECs undergo both reversible and irreversible processes, which critically affect the electrical and dynamic performance, stability, and long-term reliability of OECT devices.

Currently, CPs are the most widely used OMIECs. Among them, poly(3,4-ethylenedioxythiophene) (PEDOT), a p-type CP, is commonly blended with polystyrene sulfonate (PSS), which acts as a charge-balancing dopant. The resulting complex, PEDOT:PSS, is the most widely employed p-type channel material in OECTs due to its commercial availability, effective charge storage and transport, biocompatibility, optical transparency, relative stability in aqueous electrolytes and mechanical flexibility.[68–70] Pristine PEDOT:PSS typically exhibits moderate properties and is therefore modified through post-processing or additive incorporation. For example, the addition of the surfactant Triton X-100 (TX) improves the self-healing properties,[53] while ionic liquid additives, specifically 1-ethyl-3-methylimidazolium (EMIM) as the cation and the anions chloride (Cl), trifluoromethanesulfonate (OTF) and tricyanomethanide (TCM), improve the PEDOT:PSS morphology and mixed ionic–electronic transport.[50] However, the acidity of PSS may negatively affect adjacent materials.[71] To address this issue, other PEDOT-based CPs have been developed, including PEDOT with tosylate (PEDOT:Tos),[72] dodecylbenzenesulfonic acid (PEDOT:DBSA),[73] as well as ammonium salt complex (PEDOT-S:$(Oct)_2NH_2$),[16] *etc.* Side-chain and backbone engineering offer opportunities for further development of advanced polymers such as PE_2-OE_4, a copolymer of 3,4-propylenedioxythiophene (ProDOT) and 2,2′-bis(3,4-ethylenedioxy)thiophene (biEDOT) backbone bearing linear oligo(ethylene oxide) side chains.[54] Most PEDOT-based materials operate in depletion mode, exhibiting significant conductivity at zero gate bias. This has motivated the development of alternative CPs to enable different operating modes and meet application-specific requirements.

Many studies have focused on the development and investigation of CPs for OECTs based on polythiophene derivatives. A variety of molecular building blocks are employed in their synthesis to tailor the electronic, structural, and ionic transport properties of the resulting polymers. These building blocks include benzodithiophene (BDT); thiophene (T); bithiophene (T2); thienothiophene (TT); various glycolated bithiophenes (*e.g.*, g2T, gT2, g3T2, *etc.*); cyclopentadithiophene (CPDT); 3,30-dimethoxy-2,20-bithiophene (MeOT2). Additionally, other commonly used units such as diketopyrrolopyrrole (DPP), isoindigo (IID), naphthalene diimide (NDI), benzotriazole (BTz), benzothiadiazole (BT), and fluorinated thiophene derivatives further modulate energy levels, improve planarity, and optimize mixed ionic–electronic conduction in thiophene-based CPs. As a result, many p-type thiophene-based CPs have been synthesized, including poly(3-hexylthiophene) (P3HT),[74] poly[3-(6-hydroxy)hexylthiophene] (P3HHT),[75] p(g2T-TT),[76] P($g_4$2T-TT),[77] p(g2T2-g4T2),[78] Pg2T-T,[55] Pg2T-S,[55] P3gCPDT-MeOT2,[56] *etc.* Some of these thiophene-based CPs exhibit higher transconductance (g_m) than PEDOT:PSS, but usually show lower long-term stability (Fig. 2d and e).

Heteroaromatic ladder polymers have rigid, fully fused backbones that enhance planarity and charge transport. PBBT-Me, a methylated pyrrole-benzothiazine ladder polymer, exhibits high p-type OECT performance with increased hole mobility, and operational stability.[58]

Several n-type CPs with satisfactory characteristics have been developed, including ladder-type polymers such as poly(benzimidazobenzophenanthroline) (BBL)[26] and poly(benzimidazoanthradiisoquinolinedione) (BAL) tuned *via* chlorine-substitution

Table 1 Comparative summary of (semi)conducting polymer properties and OECT metrics in 0.1 M NaCl aqueous electrolyte

OECT channel material	Type	C^*, F cm^{-3}	μC^*, F cm^{-1} V^{-1} s^{-1}	$g_m L/(Wd)$, S cm^{-1}	V_{th}, V	I_{ON}/I_{OFF}	τ_{ON}; τ_{OFF}, ms	N_C; I_{dR}/I_{d0}	Year, ref.
PEDOT:PSS/TX	p	38	91	49	0.36	1.5×10^3	6.8	10^3; 98%	2020,[53]
PEDOT:PSS/EMIM OTF	p	78	354	188	0.52	$\sim 10^5$	0.034	10^4; 92.8%	2022,[50]
PEDOT:PSS/EMIM TCM	p	89	426	218	0.73	$\sim 10^5$	0.059	10^4; 97.6%	2022,[50]
PE_2-OE_4	p	207	830	453	0.24	10^2–10^3	16.9; 1340	200; 104%	2025,[54]
p(g2T-T)	P	332	288.9	118	-0.161	$\sim 10^4$	14.2; 7.6	10^3; 100%	2024,[55]
p(g2T-S)	p	254	332.7	157	-0.094	$\sim 10^4$	10.8; 5.9	10^3; 100%	2024,[55]
P(bgDPP-MeOT2)	p	120	195	83	-0.33	1.7×10^5	0.52; 0.03	700; 98.8%	2021,[57]
P3gCPDT-MeOT2	p	145	449	344	-0.09	$\sim 10^4$	49.3; 8.8	600; 98%	2022,[56]
PBBT-Me	p	259	92.3	40.6	-0.52	2×10^6	3.19; 0.16	1.8×10^4; 90%	2023,[58]
PDPP-4EG	p	105	684	137.1	-0.6	10^5–10^6	39	600; 88%	2024,[59]
BBL_{152}	n	589	25.9	11.1	0.15	4.4×10^5	0.38; 0.15	103; 95%	2022,[26]
P75-TBAClO_4	n	41	0.24	0.39	0.29	$\sim 10^4$	7.4; 15.6	360; 79%	2023,[60]
gNDI-FBT	n	197	0.12	0.036	0.19	$\sim 10^4$	45.5; 26.8	360; 100%	2022,[61]
P(f-BTI2g-TVTCN)	n	170	41.3	12.8	0.68	$\sim 10^5$	52; 17	240; 70%	2022,[62]
P(gTDPP2FT)	n	156	42.2	7	0.64	5×10^6	1.75; 0.15	400; 54%	2022,[63]
gAIID-2FT	n	99.8	4.09	0.941	0.45	$\sim 10^5$	58.5; 18.2	1200; 100%	2023,[64]
p(C2F-V)	n	118	107.6	25.67	0.02	$\sim 10^4$	0.34; 0.11	60; 77.2%	2024,[65]
PgNaN	n	100	0.66	0.212	0.37	$\sim 10^4$	127	>200; 75%	2021,[66]
Cl_2-BAL	n	442	6.2	1.6	0.26	$\sim 10^5$	2.4	5×10^4; 99%	2024,[15]
PBFDO	n	357	196.6	~90	-0.1	$\sim 10^2$	1.81; 1.96	600; 92%	2023,[67]

(Cl_2-BAL),[15] as well as thiophene-based CPs such as PgNaN,[66] P(*g*TDPP2FT),[63] P75-TBAClO_4,[60] *etc.* However, compared with most p-type CPs, n-type CPs still show lower electron mobility and g_m, and lower long-term stability (Fig. 2d and e).

Further performance improvements have been achieved through the design of donor–acceptor (D–A) polymers. Such materials enable precise tuning of energy levels and enhanced charge transport.[79] Depending on their molecular structure, D–A CPs can operate as p-type, n-type, or ambipolar materials. Representative examples include p-type P(bgDPP-MeOT2),[57] and PDPP-4EG,[59] and n-type gNDI-FBT,[61] and P(f-BTI2g-TVTCN),[62] p(C2F-V),[65] PBFDO[67] D–A polymers (Fig. 2d and e).

Due to the large number and chemical diversity of (semi)-conducting polymers, their molecular structures, classifications and material design strategies are not discussed in detail here; instead, corresponding comprehensive review articles are cited.[2,80,81]

Fig. 2d and e summarises key performance metrics of various CPs used in OECTs, including g_m, which reflects the efficiency of voltage-to-current conversion and is proportional to the product of electronic charge carrier mobility (μ) and volumetric capacitance (C^*); response time (τ), indicating the device's switching speed; number of stable switching cycles, representing operational stability; threshold voltage (V_{th}), defining the gate bias required to activate the device; and the on/off drain current ratio (I_{ON}/I_{OFF}), characterising the device's modulation capability. The Fig. 2d and e demonstrates that no single material simultaneously achieves optimal values across all metrics. For instance, materials with high μC^* often suffer from slower τ or larger $|V_{th}|$, and *vice versa*. Likewise, high-performance materials may compromise long-term stability. These trade-offs highlight the need for continued development of new CPs and refinement of existing ones to achieve balanced characteristics.[82]

In addition to CPs, OECT channels can also be made using biopolymers, SOMSs, CP–SOMS and organic–inorganic hybrid materials.

Biopolymers offer biodegradable, biocompatible options for OECTs. For example, PEDOT–cellulose nanocomposites show good conductivity and water dispersibility,[83] and adapt OECTs for environmentally conscious wearables.[84]

SOMSs offer high charge carrier mobility, high purity, precise structure–property control, high switching currents ratio, and fast response time.[27,85,86] However, some CPs still outperform them in key metrics. SOMSs in combination with CPs are used for some improvements, including passivation to enhance stability,[87] tuning conductivity type,[88] and structure ordering.[89]

Inorganic nanosized components integrated into organic matrices can enhance their performance. Metallic and oxide nanoparticles can improve sensitivity, charge transport, and stability: hydrophilic polyEG-coated gold nanoparticles enhanced mixed ionic–electronic transport in hydrophobic P3HT;[90] iron oxide in PEDOT:PSS boosted sensitivity and selectivity,[91] while plasmonic gold nanoparticles increased conductivity and, with photo-annealing, improved μC^* and stability.[92] Nafion nanoinclusions in PEDOT:PSS create phase-separated, proton-permeable domains that enlarge the internal ion-accessible interfacial area, thereby accelerating ion penetration and improving channel doping/de-doping efficiency, which enhances the OECT g_m and response speed.[93,94] Carbon nanotubes were used to enhance charge mobility in BBL,[29] and to decrease contact resistance in PEDOT:PSS.[23] MXenes offer high conductivity and surface area; their interaction with PEDOT:PSS improves both μ and C^*.[95]

The chemical and structural diversity of OMIECs enables tuning of multiple device-relevant properties, but optimisation often involves trade-offs and complexities in understanding their mechanisms, requiring direct, real-time, label-free insights into material layer behaviour, for example *via* techniques such as (E)QCM-D.

3. Basic principles of (E)QCM-D. Opportunities for OMIECs and OECT study

Within the broad class of acoustic resonant sensors, QCM represents a particularly well-developed platform for probing mass and viscoelastic loading at surfaces.[96–99] Its widespread adoption stems from its exceptional mass sensitivity and the inherently high quality factor of quartz resonators, which together enable detection limits on the order of 10^{-6} to 10^{-9}, defined as the ratio of the added mass to the resonator mass per unit area. A QCM is a piezoelectric device comprising a thin quartz crystal plate with a defined crystallographic orientation, most commonly the AT-cut operated in the thickness shear mode.[100–102] In more specialised applications, other cuts such as SC,[103,104] BT,[105] and others may also be employed. Variations in electrode design, such as their shape, morphology, thickness, and configuration, can influence the device sensitivity, energy dissipation, and stability of the resonant mode. The conventional QCM architecture employs circular metal electrodes on both faces of the quartz crystal to achieve uniform excitation of the thickness-shear mode. Nevertheless, several electrode design variants, differing in shape,[106,107] morphology,[108] thickness,[109] and configuration,[110] have been developed, which influence the spatial distribution of the shear field, energy dissipation, and overall device sensitivity. Various quartz plate–electrode architectures have been developed, including configurations with electrodes on one or both sides of the crystal, supporting different excitation schemes.[98,110] Additionally, highly sensitive electrodeless techniques have been introduced.[111] Although numerous configurations are possible, the following discussion focuses on the standard QCM technique to ensure clarity and emphasise its fundamental use in studying OMIECs.

QCM operates based on the principle of the converse piezoelectric effect, where the application of an alternating electric potential leads to the generation of quartz crystal vibrational oscillations.[101,112] For a theoretical analysis of microacoustic sensors, a wave description can be applied,[113] in which the medium in contact with the resonator acts as an

acoustic load impedance. The further developed acoustic load concept[96,114–117] extends the mass load by an acoustic factor, wherein the so-called Sauerbrey[118] and Kanazawa[119] equations are just two special cases. In particular, in the Sauerbrey rigid mass case $\Delta f \sim \Delta m$ applies, in case a Newtonian liquid is in direct contact to the quartz crystal surface $\Delta f \sim (\rho\eta)^{1/2}$, where Δf is frequency change, m is mass, ρ is density, η is viscosity. Measurements or resonance frequency changes of the quartz crystal sensor become a wonderful tool to measure minute changes in equivalent mass or acoustic load impedance at the sensor surface. This simple method is particularly effective when measuring rigid uniform thin coatings. The analysis of the QCM response when interacting with layers with a more complex nature like suspensions[120] and other heterogeneous materials, soft and biological materials,[121,122] *etc.*, exhibits more intricate behaviour and in some cases cannot be satisfied only by measuring the frequency changes, but also requires an analysis of changes in scattering (or losses). QCM modified version with dissipation monitoring (QCM-D) in addition to measuring frequency change provides information about the energy loss of the oscillating system, reflecting the viscoelastic properties of the deposited layers.[123–125] The most important advantages of the QCM-D characterisation technique include accurately measures series and parallel resonance, simultaneous frequency (f) and dissipation (D) tracking capability and overtones excitation;[126] moreover, contactless setup is available.[111] Speaking for easier understanding, in QCM-D approach the changes in f and D can be related to the mass associated with the deposited material and its viscoelastic properties. What is especially important for this review, this method is instrumental in understanding the behaviour of organic material layers,[127,128] especially when such films interacting with a liquid solution.[34,129]

Regarding OMIEC layers analysis, if the material deposited on the quartz sensor surface is rigid, the changes in dissipation are small, so QCM is often sufficient for measuring the thickness of thin dry OMIEC films. However, if a film has a sufficient viscous component, which is typical for thick soft polymer films, or OMIEC films have interacted with an electrolyte, the dissipation can change significantly and the QCM-D method is preferable.

In most cases, the EQCM-D setup used to study electrochemical processes in polymer and OMIEC film-electrolyte systems involves a quartz crystal that is coated with a thin film containing a nanosized metal (Me) sublayer deposited on the quartz surface (Fig. 3a and b). This Me/OMIEC-coated quartz crystal is then immersed in an electrolyte solution (Fig. 3c).

A typical EQCM-D setup employs a three-electrode configuration consisting of a working electrode (WE), a counter electrode (CE), and a reference electrode (RE), as illustrated in Fig. 3c. The coated quartz crystal acts as a WE. A typical CE is made of Pt. The RE is usually made of Ag/AgCl for aqueous-based electrolytes (in some cases, the RE material may be different, especially for non-aqueous electrolytes). The electrolyte solution is usually pumped into the chamber with a controlled flow rate.

The three-electrode configuration enables precise control and stabilisation of the working electrode's potential, independently of current fluctuations and resistance changes in the cell. In a two-electrode system, the WE potential is defined by the voltage difference between the WE and CE (see Fig. 1a–c); however, the CE can experience a variable voltage drop

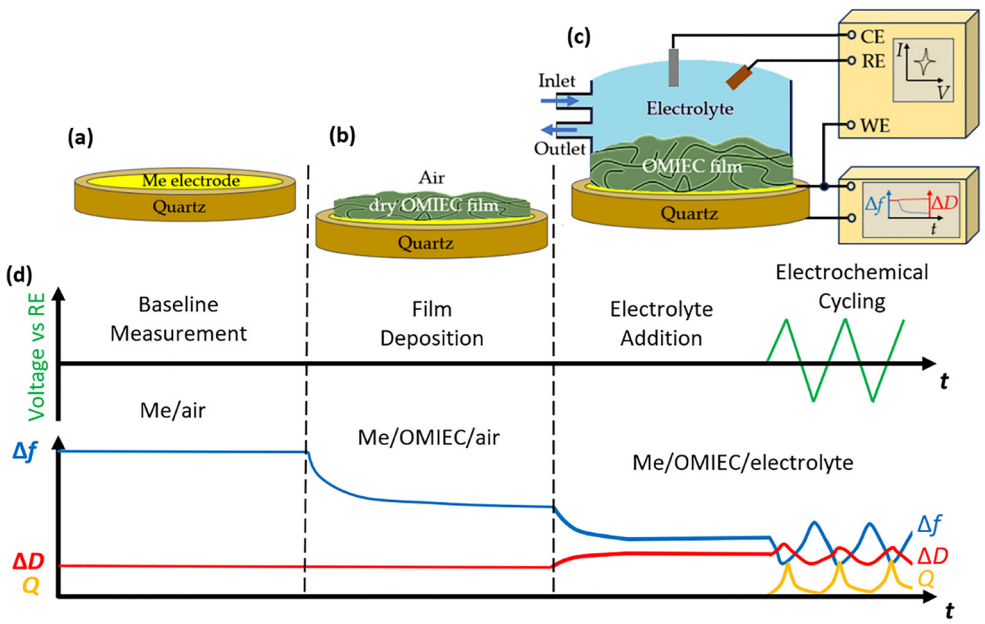

Fig. 3 Schematic of a bare QCM-D sensor (a), an OMIEC-coated sensor in air (b), and a swollen OMIEC-coated sensor in electrolyte in an EQCM-D setup (c) using a three-electrode configuration of working (WE), counter (CE) and reference (RE) electrodes. Typical QCM-D and EQCM-D responses showing changes in frequency (Δf), dissipation (ΔD) and charge (Q) during four stages: baseline measurement, OMIEC film deposition, electrolyte introduction and electrochemical cycling (d).

depending on the current, which may lead to inaccurate control of the WE potential, especially at higher currents or with unstable electrolytes. The three-electrode setup allows the WE potential to be measured and controlled relative to a stable and well-defined RE, while the CE only serves to carry the current. This ensures more accurate and reproducible control of the electrochemical processes at the WE, which is critical for detailed studies using EQCM-D.

The described configuration of EQCM-D setup completely reproduces all the processes that occur when the OECT operates in the mode when the potentials at the source and drain of the OECT are the same. The electrolyte has an interface with an OMIEC film into which its ions can penetrate into material bulk under the action of an applied electric field. The ion activity in the electrolyte and their penetration into the OMIEC film are controlled by the electric field. The applied voltage can promote ion injection from the electrolyte into the OMIEC layer, and thus modulate the OMIEC film conductivity. Cyclic voltammetry is a common electrochemical method combined with EQCM-D to quantify changes in mass and viscoelasticity during the oxidation and reduction processes of OMIECs.[130] Specifically, the current is recorded along with changes in frequency and dissipation in response to changes in voltage.

A typical EQCM-D experiment begins with taking baseline measurements of the bare sensor in both air (Fig. 3a), as well in the electrolyte, followed by similar baseline measurements of the coated sensor (Fig. 3b) to determine the dry coating's thickness (Fig. 3d). Next, the electrolyte is pumped into the chamber with the coated sensor, and then the cell is kept for some time (usually >15 min) to equilibrate with the electrolyte (Fig. 3d). In some cases, to achieve a more complete equilibration of the OMIEC, additional conditioning is performed through repeated electrochemical cycling. Following this, EQCM-D measurements are carried out by combining quartz crystal sensor data with cyclic voltammetry (CV) at various scan rates. Once the raw data are collected, the user must analyze the relationships between frequency shift (f), dissipation (D), and the transferred charge (Q) (Fig. 3d). The CV modulation features of OMIEC depend on the material. Some OMIECs with p-type conductivity initially have mobile carriers (named holes) without any voltages on the electrodes. However, if we apply a positive voltage to the CE, it allows electrolyte cations to enter the OMIEC film. This makes the holes disappear in OMIEC layer and reduce electrical conductivity. In other OMIECs, films show nonconductive properties even with no applied voltage. When the voltage makes anions (for the case of a OMIEC with p-type conductivity) or cations (for the case of n-type) penetrate into the OMIEC layer, this generates respectively holes or electrons that switch the film in conductive state.

For OMIEC films, EQCM-D applications have included monitoring the evolution of the viscoelastic properties and swelling characteristics,[131–133] quantifying ion/solvent transport, and ionic-to-electronic coupling efficiency.[33] Besides, EQCM-D has also been applied to characterize and optimize electropolymerisation/deposition of CPs.[134] In the area of biosensors, where bio-molecules adsorb onto the surface, EQCM-D has been utilized while biasing the surface to monitor the biomolecular response of proteins, cells, DNA, and other species.[135] Some specific cases are discussed below.

Table 2 provides examples of the use of (E)QCM-D for OMIEC and OECT studies.

Table 2 shows that most works focus on EQCM-D studies of OMIECs in aqueous electrolytes. It is due to their biocompatibility, safety and environmental friendliness in OECT applications. For aqueous electrolytes, Ag/AgCl reference electrodes are typically used due to their stable and well-defined potential. However, non-aqueous systems are sometimes employed for improved electrochemical stability, where OECT device longevity is crucial. For example, the use of PEDOT-S:$(Oct)_2NH_2$/$BMIMBF_4$ achieved high OECT cycling stability.[16] In this work a standard Ag/AgCl RE was also used. Other work compared Ag/AgCl and Pt electrodes in PEDOT:PSS with [BMIM][OTf] and [EMIM][DCA] ionic liquids, finding similar transconductance but lower threshold voltages with Ag/AgCl.[168] Both electrodes suit non-aqueous electrolytes, though Ag/AgCl offers slight advantages. In some cases, Ag/Ag^+ electrodes are preferred for stable potentials in organic solvents. *E.g.*, it was shown that 0.1 M TBAHFP in acetonitrile enhances electrochemical stability and device performance with P3HT channels and Ag/Ag^+ gate electrode compared to aqueous electrolytes.[169]

4. OMIEC layers mass (thickness) change, viscoelastic properties and depth-sensitive analysis: the cases of dry films and immersed in electrolyte solution

Understanding the behaviour of OMIEC layers in different environments is important for applications in organic electronics and neuromorphic devices because their performance and stability are highly sensitive to external conditions. OMIEC films properties can change significantly when moving from a dry state to an electrolyte-immersed environment,[33] and are further influenced by the specific type and composition of electrolyte.[36,132] In the dry state, OMIEC films typically exhibit a stable and well-defined thickness, with mechanical properties primarily determined by their molecular structure, packing density, and intermolecular interactions. The viscoelastic response in this state usually reflects the intrinsic characteristics of the material. When immersed in an electrolyte solution, OMIEC layers undergo hydration, swelling, and ion uptake, resulting in an increase in mass and thickness.[37,170] These changes can be dynamic and depend on factors such as the type of electrolyte ions, ionic strength, pH, OMIEC charge density, film hydrophilicity, OMIEC-electrolyte interfacial conditions and *etc.*[36,87,171] The hydration process affects the viscoelastic behaviour, often making the film more compliant and changing its mechanical moduli. QCM-D is a powerful tool for analyzing these properties in real time, providing insight into mass absorption, viscoelastic and morphological changes. In

Table 2 Examples of the use of (E)QCM-D for OMIEC and OECT studies[a]

OMIEC material; conductivity type; original thickness	Electrolyte/solution; flow rate	Microbalance technique; electrode materials	Objectives and applications of (E)QCM-D study	Measurement data acquisition and processing aspects	Ref., year
PEDOT:PSS and PEDOT-PC; p-type	0.5–10 mM Ca^{2+} in HEPES buffer; 1 mg mL^{-1} BSA and FBS in PBS buffer; 30 μL min^{-1}	QCM; 5 MHz QSX 301; Q-Sense AB system (Biolin Scientific); Au WE.	Observing the nonspecific interactions of OMIEC materials with proteins.	Resonance frequencies were measured simultaneously at 5 MHz and its harmonics (15, 25, 35, 45, 55, and 65 MHz). Protein-OMIEC interactions study was performed at 25 °C.	[68]2025
PEDOT:PSS and PEDOT:ClO_4; p-type; ∼100 nm	0.1 M NaCl AS	EQCM-D; BluQCM QSD-300 with SP-200 PS (Bio-Logic); Au WE, Pt CE, Ag/AgCl RE.	Investigating the doping and de-doping mechanisms; mass transport during electrochemical processes.	Prior to measurements, the CP-coated sensors were soaked in electrolyte for 1 h to reach equilibrium, and 20 repeated electrochemical cycles were applied for conditioning. Samples were measured at different scan rates from 20 to 100 mV s^{-1}. Sauerbrey and viscoelastic models used to fit 3th, 5th, and 7th overtones data.	[136]2025
p(g2T-TT) and $PrC_{60}MA$; p/n-type; 60 nm	0.1 M KCl AS; 100 μL min^{-1}	EQCM-D; 5 MHz Q-sense E1/E4, RenLux Crystal Ltd, QWEM 401, Q-sense Explorer (Biolin Scientific); Au WE, Pt CE, Ag/AgCl RE.	Monitoring the mass uptake/ejection during electrochemical process.	Only the 3rd overtone was used in calculations. Δm was calculated based on the Sauerbrey equation.	[88]2025
p(C2F-z); n-type; 79 ± 15 nm	0.1 M NaCl AS	EQCM-D; QWEM 401, QCM5140TiAu120-050-Q (Quartz Pro), Autolab PGstat128N PS; 0.7854 cm^2 AA, Au WE, Pt CE, Ag/AgCl RE	Ion penetration and water uptake monitoring. Swelling analysis.	The analyzer measured f and D shifts of the 1st, 3rd, 5th, 7th, 9th, and 11th harmonics, which provide information about the changes in sample mass and softness. The films are approximated to behave as Kelvin–Voigt elements.	[137]2025
BBL/PCBM; n-type; ∼40 nm	0.1 M NaCl or NaOH AS	QCM coupled with CV; 8.94 MHz ± 30 kHz QCM922A and VersaSTAT PS (AMETEK Scientific Instruments); Au WE, Pt CE, Ag/AgCl RE	Control of polymer layer passivation to prevent ORR. Swelling and mass changes control.	The electrolyte comprised N_2-purged 0.1 m NaCl, and calibration of the QCM was ensured by determining the linear sensitivity factor using the Sauerbrey equation with galvanostatic deposition of silver.	[87]2025
Polythiophene-based CPs; p-type; ∼50 nm	0.1 M NaCl AS; 34 μL min^{-1}; 1 mg mL^{-1} BSA solution	EQCM-D; 5 MHz quartz; Q-sense E4 system (Gothenburg, Sweden); Pt CE, Ag/AgCl RE	Evaluation of the modulation characteristics of CPs in relation to the penetration/removal of ions into/from the films. Testing CP films for delamination resistance. Studying protein adsorbtion/desorbtion.	QCM-D measurements were conducted through a three-step process: step 1 was initial stabilisation in 0.1 M NaCl AS, step 2 involved 5 cycles of CV scans in the range of −0.5 and +0.5 V, and step 3 for subsequent washing. Δf and ΔD were monitored at 37 °C.	[22]2024
P-30; n-type; ∼50 nm	0.1 M NaCl AS	EQCM-D; CHI400C Evoltammetric PS; Au WE, Pt CE, Ag/AgCl RE	Thickness variation monitoring. Passive and active swelling analysis.	The change in frequencies was converted to the change in mass using the Sauerbrey equation.	[138]2024
P3HT; p-type; ∼50 nm	0.1 M KTFSI AS	EQCM-D; SRS QCM-200 Crystals, Phillip Technologies; Au WE, Pt CE, Ag/AgCl RE	Irreversible ion trap-ping study.	Data were collected on the NOVA pro-gram. All data analysis was done on MATLAB. The mass calculations were obtained using the Sauerbrey equation.	[74]2024
ETE-S:PC based; <70 nm	0.01 M NaCl AS/3 M KCl	EQCM-D; QSense E4 Analyzer (Biolin Scientific), IPC ISMATEC, μAutolab III PS; Au WE, Pt CE, Ag/AgCl RE	Control of polymerisation of polymer samples.	Results were obtained and analyzed using QSoft, QTools, QSense Dfind 1.2.7, Nova 2.1, and origin 2024 software. Kelvin–Voigt viscoelastic modelling (overtones 3, 5, 7, and 9).	[139]2024
p(gNDI-gT2); n-type; ∼95 nm	0.1 M NaCl AS	EQCM-D; QSense Analyzer (Biolin Sci entific), QEM 401, VSP-300 PS; Au WE, Pt CE, Ag/AgCl RE	Evaluation of the ion uptake ability. Swelling analysis.	Voigt viscoelastic modeling built into the QTools software. Various overtones, including 3rd, 5th, 7th and 9th.	[140]2024

Table 2 (*continued*)

OMIEC material; conductivity type; original thickness	Electrolyte/solution; flow rate	Microbalance technique; electrode materials	Objectives and applications of (E)QCM-D study	Measurement data acquisition and processing aspects	Ref., year
p(*jg*-NDI-T2), where *j* = 1–4; n-type; 52–65 nm	0.1 M NaCl AS	EQCM-D; QCM5140TiAu120-050-Q (Quartz Pro), Q-sense Analyzer, QWEM 401 (Biolin Scientific), Autolab PGstat128N; 0.7854 cm^2 AA, Au WE, Pt CE, Ag/AgCl RE	Swelling and shrinkage analysis of CPs during doping/de-doping cycles.	Q-Tools software was used for the modeling and data analysis. The films are approximated to behave as Kelvin–Voigt elements. Several overtones' data (N = 3, 5, 7, 9, 11) were processed.	[37]2024
PE2gT, PT2gTT, PT2gT; p-type; 61–127 nm	0.1 M KCl AS	EQCM-D; QCM200 (Stanford Research System, SRS) 5 MHz; Metrohm Autolab PGSTAT204; Au WE, Pt CE, Ag/AgCl RE	Swelling analysis of CPs during doping/de-doping cycles.	The change in frequencies was converted to the change in mass using the Sauerbrey equation.	[141]2024
P3HT:TCB; p-type; 18–26 nm	0.1 M NaCl AS	EQCM-D; QWEM Biolin Scientific; Au WE, Pt CE, Ag/AgCl RE	Testing films adhesion. Monitoring mass (thickness) changes. Measuring of capacitance.	The change in frequencies was converted to the change in mass using the Sauerbrey equation.	[89]2024
PBFDO; n-type; 60–80 nm	0.01–5 M NaCl AS	EQCM-D; QCM-D instrument (Biolin Scientific AB, Sweden); Au WE, Pt CE, Ag/AgCl RE	Tracking mass variations arising from the doping and de-doping processes under different potentials.	Several overtones' data (N = 3, 5, 7, 9, 11, 13) were processed. Viscoelastic modeling was utilized to fit the data.	[67]2024
Poly(EDOT-COOH-*co*-EDOT-PC)/PEDOT:PSS; p-type; 90–103 nm	DI water, 0.1 M NaCl AS, Biomolecule AS; 30 μL min^{-1}	QCM; QSX 301 5 MHz sensor and Q-Sense AB (Biolin Scientific)	Swelling characterisation of polymer films. Testing the anti-adhesion properties to a variety of proteins (BSA, FBS, fibrinogen, fibronectin, lysozyme).	The resonance frequencies at 5 MHz and its five harmonics (15, 25, 35, 45, 55, and 65 MHz) were simultaneously measured. The adsorbed Δm were estimated from Δf using the Sauerbrey equation.	[69]2024
PEDOT:PSS/Parylene; p-type/insulator; 72 nm	Buffer solutions with proteins (BSA, FNG, and FBS); 30 μL min^{-1}	QCM-D; QSX 301 5 MHz sensor and Q-Sense AB (Biolin Scientific)	Monitoring the protein (BSA, FBS, fibrinogen) adsorption of polymer films.	The resonance frequencies were measured simultaneously at 5 MHz and its five harmonics (15, 25, 35, 45, 55, and 65 MHz) at 25 °C.	[38]2024
P(ProDOT)s; p-type; 80–100 nm	0.5 M $TBA^+PF_6^-$/PC; 0.1 mL min^{-1}	EQCM-D; 5 MHz QSX 301 and QSense Analyzer (Biolin Scientific), Gamry Reference 3000; Au WE, Pt CE, Ag/Ag^+ RE.	Swelling characterisation.	The change in frequencies was converted to the change in mass using the Sauerbrey equation. N = 3, 5, 7, 9 overtones were monitored.	[142]2024
p(N-T); n-type; 83–104 nm	0.1 M NaCl AS; 0.1 mL min^{-1}	EQCM-D; Q-sense analyzer (QE 401, Biolin Scientific, Gothenburg, Sweden), Metrohm Autolab PGSTAT101 PS; Au WE, Pt CE, Ag/AgCl RE.	Study of the correlation between swelling and stability of films during electrochemical processes.	The data were modeled using the Sauerbrey equation within the QSense Dfind software (Biolin Scientific).	[143]2024
PEDOT-PBA; p-type	AS for electropolymerisation, 20 μL min^{-1}/glucose sensing, 100 μL min^{-1}	QCM-D; Q-sense analyzer (QE401, Biolin Scientific), PalmSens PS; Au WE, Pt CE, Ag/AgCl RE.	Monitoring of the electrodeposition of PEDOT-PBA films. Analysis of the speed and amount of glucose uptake.	The Sauerbrey equation was used to quantify Δm on the sensor resulting from glucose uptake based on the 5th, 7th, and 9th overtones data.	[144]2024
PEDOT:PSS; p-type; ~200 nm	NH_4Cl, KCl, NaCl, $CaCl_2$, $MgCl_2$ AS	EQCM-D; Stanford Research Systems, 5 MHz, SRS QCM200 instrument coupled with the K2636B; Au WE, Ag/AgCl RE.	Correlate electrical parameters with film swelling.	The change in frequencies was converted to the change in mass using the Sauerbrey equation.	[36]2024
DTP-based CPs; p-type; 49–66 nm	0.1 M NaCl AS	EQCM-D; Q-sense analyzer (QE401, Biolin Scientific), PalmSens PS; Au WE, Pt CE, Ag/AgCl RE.	Monitoring mass (thickness) changes. Swelling measurements.	To calculate Δm, complex shear modulus was analyzed and fitted using three different overtones (3rd, 5th and 7th). QTools and D-find software were used for modeling and data analysis. The Kelvin–Voigt viscoelastic model was used to fit the data.	[145]2023
BBL; n-type; ~100 nm	100 mmol L^{-1} KCl AS	EQCM-D; SRS QCM200 instr. 5 MHz, Metrohm Autolab PDSTAT204 PS; 0.4 cm^2 AA, Au WE, Pt CE, Ag/AgCl RE.	Study of irreversible and reversible mass uptake. Evaluation of the ORR impact.	Evaluating of the ORR impact, the charge calculations in the QCM measurement were based on the de-doping current. CP films were considered as rigid, so Δm was calculated using the Sauerbrey model.	[41]2023

Table 2 (*continued*)

OMIEC material; conductivity type; original thickness	Electrolyte/solution; flow rate	Microbalance technique; electrode materials	Objectives and applications of (E)QCM-D study	Measurement data acquisition and processing aspects	Ref., year
PEDOT:PSS; p-type	PBS buffer and LCB1 (57 μM); 50 μL min^{-1} and 40 μL min^{-1}	QCM-D; Qsense E4 QCM.	Quantifying the mass of LCB1 adsorbed onto the CP surface.	The experiment consisted of three steps, when PBS buffer, LCB1, and PBS buffer were injected sequentially into the chamber. Change in mass was calculated by using the Sauerbrey equation.	[146]2023
NDI-T2-based P-75; n-type; 46–105 nm	0.1 M NaCl AS; 100 μL min^{-1}	EQCM-D; Q-sense analyzer (QE401, Biolin Scientific AB), Autolab PGstat128N; 0.7854 cm^2 AA, Au WE, Pt CE, Ag/AgCl RE.	Evaluation of passive and active swelling. Calculation of water and cation species injected into the films upon electrochemical doping.	Measurements were conducted before (used as reference) and after coating with the CPs in the degassed electrolyte to prevent any effect of ORR on the current values. Q-Soft was used to calculate the respective films' areal mass in dry and swollen states based on several overtones' data (N = 5, 7, 9).	[60]2023
PEDOT:PSS and p(g2T-TT); p-type; 150 nm	0.1 M NaCl AS; 0.2 mL min^{-1}	EQCM-D; QWEM Biolin Scientific, Autolab PGSTAT128N PS; Au WE, Pt CE, Ag/AgCl RE.	Study water uptake and CP films swelling. Quantifying the number of water molecules entering the films operated at different biases.	Data acquiring *via* QSoft program. To quantify the mass and viscoelastic property changes the Voight element was used. Several overtones' data (N = 3, 5, 7, 9) were processed.	[76]2023
PgBT(F)2gTT, PgBT(Ion)2gTT, PgBT(TriEG)2gTT; p-type; 60 nm	0.1 M KCl AS	EQCM-D; QCM200 SRS, Metrohm Autolab PGSTAT302N PS; Au WE, Pt CE, Ag/AgCl RE.	Monitoring the mass change of the films during electrochemical processes.	The change in frequencies was converted to the change in mass using the Sauerbrey equation.	[79]2023
PEDOT-PC; p-type; 45 nm	Biomolecules buffer solutions; 30 μL min^{-1}	QCM, Q-Sense AB system, Biolin Scientific.	Monitoring the PEDOT films' nonspecific and specific interaction with proteins (BSA, FBS, CRP). PEDOT based OECT gate electrode functionalisation measurement.	The resonance frequencies were measured simultaneously at 5 MHz and its five harmonics (15, 25, 35, 45, 55, and 65 MHz).	[147]2023
P3HT; p-type; 60 nm	NaCl and $NaClO_4$ AS	QCM; QCM200 (Stanford Research Systems) on the 10 MHz Au-coated AT quartz crystal, tungsten probe.	CP film quality change estimation. Analysis the penetration of the ions into the film during the electrochemical doping depending on the electrolyte and anion type.	The voltage bias was applied between the Au on the quartz crystal and a tungsten probe immersed in the salt solution. After applying different voltage, Δf was converted to a mass change using the Sauerbrey equation.	[148]2023
gAIID-2FT and gAIID-T; n-type; 35 and 50 nm	0.1 M NaCl AS	EQCM-D; QWEM, Autolab PGstat128N PS; Au WE, Pt CE, Ag/AgCl RE.	Monitoring the mass uptake/ejection during electrochemical process.	Q-Tools and D-find software were used for the modeling and data analysis. CP films to behave like a Kelvin–Voigt element were approximated. The f and D data of three different overtones (N = 5, 7, 9) were used.	[64]2023
P3CAT; p-type; 28–94 nm	0.1 M NaCl AS	QCM-D; QSense Explorer Analyzer (Biolin Scientific AB, Sweden); Au WE.	Passive swelling measurements.	The f difference between the bare and the Ti/Au/CP coated sensors was compared using the Q-Soft. Δm was calculated based on the Sauerbrey model.	[149]2023
P3MEEET; p-type; 170 nm	0.1 M NaCl/0.02 M KTFSI	EQCM-D; QCM chips (Quartz PRO, 5 MHz, 14 mm Ti/Au); 0.785 cm^2 AA, Au WE, Pt CE, Ag/AgCl RE	Analysis the role of electrolyte composition on the molecular weight dependence of mixed conduction.	The mass change was modeled with the Sauerbrey equation using a Pythonscript.	[150]2023
g2T2-gBTj, where j = 2, 4, 6; p-type; 35–150 nm	0.1 M NaCl AS	EQCM-D; Q-sense analyzer (QE401, Biolin Scientific), SP-300 (BioLogic Science Instruments); Au WE, Pt CE, Ag/AgCl RE	Passive and active swelling measurements.	The f difference between the bare and coated sensors was compared using the Q-Soft. Δm was calculated based on the Sauerbrey equation.	[151]2023

Table 2 (*continued*)

OMIEC material; conductivity type; original thickness	Electrolyte/solution; flow rate	Microbalance technique; electrode materials	Objectives and applications of (E)QCM-D study	Measurement data acquisition and processing aspects	Ref., year
P-75, P-90, P-100, P-ZI; n-type; 60–80 nm	GOx solution, 10 mg mL^{-1}/PBS, 20 μL min^{-1}	QCM-D; Q-sense analyzer (QE401, Biolin Scientific AB) with Cr/Au-coated quartz crystals.	Monitoring enzyme adsorption and characterisation of the adsorbed layer.	The adsorbed mass values are calculated from the Sauerbrey equation and the Voigt model, fitting the 5th, 7th, and 9th harmonic of f and D data.	[152]2023
p(C_6NDI-T); n-type; 45 nm	0.1 M NaCl AS	QCM-D; Q-sense analyzer (QE401, Biolin Scientific) with Au-coated quartz crystal.	Quantifying polymer film electrolyte uptake.	The f difference between the bare and coated sensors was compared using the Q-Soft. Δm was calculated based on the Sauerbrey equation.	[153]2023
PEDOT:PSS (CE); p-type; and Au/aptamer (gate, WE); ~100 nm	Electrolyte with TGF-β_1 aptamer	EQCM-D; QWEM, Ivium PS; Quartz PRO 5 MHz Ti/Au WE, Ag/AgCl RE, PEDOT:PSS CE.	Monitoring the equivalent functionalisation process (Au gate electrode measurements).	Non-standard organisation of the measurement setup, in which PEDOT:PSS OECT channel is used as CE. The mass change was modeled with Sauerbrey equation.	[39]2023
P(gPzDPP-CT2), P(gPzDPP-T2); n-type; 68 and 655 nm	0.1 M NaCl AS	QCM-D; Q-sense analyzer (QE401, Biolin Scientific) with Au-coated quartz crystal.	Passive swelling measurements.	The f difference between the bare and coated sensors was compared using the Q-Soft. Δm was calculated based on the Sauerbrey equation.	[154]2022
p(g2T-TT)/PrC_{60}MA blend; p/n-type; 60 nm	0.1 M KCl AS; 100 μL min^{-1}	EQCM-D; 5 MHz Q-sense E1/E4, RenLux Crystal Ltd, QWEM 401, Q-sense Explorer (Biolin Scientific); Au WE, Pt CE, Ag/AgCl RE.	Monitoring the mass uptake/ejection during electrochemical process. Evaluation of the ORR impact.	Only the 3rd overtone was used in calculations. Δm was calculated based on the Sauerbrey equation.	[40]2022
PEDOT–PAH/PSS/PDDA; p-type; 22 nm	0.1 M KCl + 0.1 mg mL^{-1} PSS and PDDA	QCM; QCM200 setup (Stanford Research Systems); 5 MHz QCM25 Au WE.	Monitoring of layer-by-layer assembly process.	The thickness estimation was performed applying Sauerbrey equation. The motion resistance was analyzed in order to identify either elastic or viscoelastic behaviour of the architecture.	[155]2022
PEDOT:PSS; p-type; 40 and 220 nm	0.1 M RbBr/0.1 M NaCl AS	EQCM-D; QWEM, Ivium PS; 0.785 cm^2 AA, Au WE, Pt CE, Ag/AgCl RE.	Understanding the mass uptake, morphological changes, and charge transport in CP during electrochemical process.	All data analysis and model simulation were performed with Matlab software based on the Sauerbrey equation (dry thin films) and viscoelastic model (soft and thick films).	[32]2022
P4gNDI and P4gNDTI; n-type; ~80–90 nm	0.1 M NaCl AS	EQCM-D; Q-sense analyzer (QE401, Biolin Scientific) and Autolab PGstat128N PS; Au WE, Pt CE, Ag/AgCl RE.	Study of passive and active swelling of polymer films.	The modeling and data analysis was carried out using Q-Tools and D-find software. CPs thickness was calculated by using the Sauerbrey model. The Kelvin–Voigt viscoelastic model was used to fit the data of soft films. To quantify the mass, the data of three overtones (N = 3, 5, 7) were used.	[156]2022
P3gCPDT-based CPs; p-type; 39–57 nm	0.1 M NaCl AS	EQCM-D; Q-sense analyzer (QE401, Biolin Scientific), SP-300 (BioLogic Science Instruments); Au WE, Pt CE, Ag/AgCl RE.	CPs thickness change measurements. Investigation of the correlation between film morphology and ion penetration.	The f difference between the bare and coated sensors was compared using the Q-Soft. Δm was calculated based on the Sauerbrey equation. The 5th overtone was used. 3 CV cycles from 0 to 0.8 V were performed for the ions and water absorption calculations.	[56]2022
P(NDITEG-T), P(NDIDTEG-T); n-type; 42–110 nm	0.1 M NaCl AS	QCM-D; QCM200 System; Au WE.	Passive swelling study depending on polymer materials and their EG content.	Δm was calculated based on the Sauerbrey equation (dry films) and viscoelastic model (soft films).	[157]2022
p(g_3C_2T2-T); p-type and p(C_6NDI-T); n-type; 85 nm	0.1 M NaCl AS; 100 μL min^{-1}	EQCM-D; Q-Sense analyzer (QE401, Biolin Scientific), Autolab PGstat128N PS; 0.7854 cm^2 AA, Au WE, Pt CE, Ag/AgCl RE.	Using as an additional investigation of stability.	Δm were calculated using the Sauerbrey Equation.	[158]2022

Table 2 (*continued*)

OMIEC material; conductivity type; original thickness	Electrolyte/solution; flow rate	Microbalance technique; electrode materials	Objectives and applications of (E)QCM-D study	Measurement data acquisition and processing aspects	Ref., year
P3HT; p-type; 215 nm	0.5 M $LiCF_3SO_3$ propylene carbonate	EQCM-D; Q-sense E1 module (Biolin scientific), Interface 1000, Gamry Instruments and Solartron 1260/1280 PS; Au WE, Pt CE, Ag RE.	Identifying the time scale at which the doping reaction transitions from kinetic to diffusion control.	Δm was quantified using the Sauerbrey model in Qtools software. Modelling was carried out using the 3rd, 5th and 7th overtones	[159]2022
PEDOT:Tos; p-type; ~65 nm	0.1 M NaCl AS	EQCM-D; QSense QSX301; Au WE, Pt CE, Ag/AgCl RE.	Study of water uptake and ion exchange in PEDOT:Tos films. Investigation on the effect of ORR on the frequency changes.	The frequency to mass conversion was done with the Smartfit viscoelastic modeling function of QSense Dfind including overtones (N = 3, 5, 7, 9, 11). To study the ORR impact on the mass changes, independent investigations with CVs were performed.	[72]2021
p(NDI-g3T2); n-type; 71–169 nm	0.1 M NaCl AS; 50 μL min^{-1}	EQCM-D; Q-sense analyzer (QE401, Biolin Scientific), Autolab PGstat128N PS; Au WE, Pt CE, Ag/AgCl RE.	Monitoring the water uptake. Investigating the electrochemical stability of polymers.	Measurements were performed at low O_2 concentrations to limit Faraday side reactions between CP and molecular oxygen. Δm was calculated using Sauerbrey equation and viscoelastic model.	[160]2021
p(C3-gNDI-gT2), p(C6-gNDI-gT2); n-type; 70 and 91 nm	0.1 M NaCl AS	EQCM-D; Q-sense analyzer (QE401, Biolin Scientific), Autolab PGstat128N PS; 0.7854 cm^2 AA, Au WE, Pt CE, Ag/AgCl RE.	Investigating the effect of functionalisation with alkyl spacers on the swelling ability of the polymers.	The modelling and data analysis was carried out using Q-Tools and D-find software. To quantify the mass correctly (*via* Kelvin–Voigt viscoelastic model), the f and D data of three different overtones (5th, 7th, and 9th) were used.	[161]2021
P-90, BBL; n-type; 40 and 44 nm	0.1 M NaCl AS	EQCM-D; QSensors QSX 338 and QEM 401 (Biolin Scientific), Autolab PGstat128N PS; 0.7854 cm^2 AA, Au WE, Pt CE, Ag/AgCl RE.	Elucidating the amount of mass loaded in the films during electrochemical doping. Estimation for ion-to-electron coupling efficiency.	Measurements were performed with de-oxygenated electrolytes. The f and D data of the 3rd, 5th, 7th, 9th, and 11th harmonics were measured. Δm was calculated based on the Sauerbrey equation (dry films) and viscoelastic model (soft films).	[46]2021
p(NDI-T2-L2); n-type; 56 nm	PBS; 0.1 mL min^{-1}	QCM-D; Qsense Analyzer system (Biolin Scientific AB, Sweden);	Thickness evaluation. Characterizing lipid bilayer formation on polymer film.	QSoft software. Sauerbrey equation.	[162]2020
p(g2T-TT): p(a2T-TT); p-type; 50–60 nm	0.1 M NaCl AS	EQCM-D; Q-sense analyzer (QE401, Biolin Scientific), Autolab PGstat128N PS; 0.7854 cm^2 AA, Au WE, Pt CE, Ag/AgCl RE.	Investigating the swelling behaviour upon doping.	The mass change was modeled with Sauerbrey equation (for rigid films) and viscoelastic Kelvin–Voigt model (for hydrated films) using 5, 7, 9th overtones data.	[20]2020
P-90:TBAF; n-type; 72–160 nm	0.1 M NaCl AS	EQCM-D; Q-sense analyzer (QE401, Biolin Scientific), PS; Au WE, Pt CE, Ag/AgCl RE.	Measuring water/cation uptake due to electrochemical doping. Studying the impact of molecular n-doping on electrochemical doping.	No information.	[163]2020
p(g3T2), p(g2T2-g4T2), p(g1T2-g5T2), p(g0T2-g6T2); p-type; 45–75 nm	0.1 M NaCl AS	EQCM-D; Q-Sense Analyzer (QE401 system, Biolin Scientific) with QSensors (QSX 338), Autolab PGstat128N PS; 0.7854 cm^2 AA, Au WE, Pt CE, Ag/AgCl RE.	Quantifying the changes in mass and viscoelasticity from the influx of ions and water into the organic semiconductor.	The data analysis was carried out using QSoft401. The mass change was modeled with Sauerbrey equation (for rigid films) and viscoelastic Kelvin–Voigt model (for hydrated films) using 1st–11th overtones data.	[78]2020
P3MEET, P3MEEMT, P3MEEET; p-type; 92, 122, 143 nm	0.1 M NaCl AS	EQCM-D; Q-Sense Analyzer (QE401 system, Biolin Scientific), Autolab PGstat128N PS; Au WE, Pt CE, Ag/AgCl RE.	Measuring thickness changes and water uptake.	Q-Tools and D-find software was used for the modeling and data analysis of three different overtones (3rd, 5th, and 7th).	[164]2020
p(g2T-TT); p-type; 54–59 nm	0.01–6 M NaCl AS	EQCM-D; Q-sense electrochemistry module, Autolab	Study of polymer film swelling when doped with low and high	The mass change was modeled with Sauerbrey equation (for rigid films) and viscoelastic	[165]2019

Table 2 (*continued*)

OMIEC material; conductivity type; original thickness	Electrolyte/solution; flow rate	Microbalance technique; electrode materials	Objectives and applications of (E)QCM-D study	Measurement data acquisition and processing aspects	Ref., year
		PGstat128N PS; Au WE, Pt CE, Ag/AgCl RE.	concentration electrolyte solutions.	Kelvin–Voigt model (for hydrated films) using 5, 7, 9th overtones data.	
$PTHS^{-}TMA^{+}$-*co*-P3HT; p-type; 21–90 nm	0.1 M NaCl AS	QCM-D; Q-sense analyzer (QE401, Biolin Scientific); Au WE.	Dry and wet thicknesses of the copolymer films after swelling evaluation.	The thickness was calculated using Sauerbrey equation. The 5th overtone was used for calculation. Q-soft software was used for overtones (N = 3, 5, 7) data processing.	[166]2019
P-90; n-type; 62 and 88 nm	0.1 M NaCl AS	EQCM-D; Q-sense analyzer (QE401, Biolin Scientific), Autolab PGstat128N PS; Au WE, Pt CE, Ag/AgCl RE.	Swelling measurements of CPs with different solvents to determine the optimal solvent composition.	Q-Tools and D-find software were used for the modeling and data analysis. The mass change was modeled with Sauerbrey equation (for rigid films) and viscoelastic Kelvin–Voigt model (for hydrated films) using 5, 7, 9th overtones data.	[167]2019
p(g2T-TT); p-type; ~60 nm	0.1 M NaCl/NaF/NaBr/$NaBF_4$/$NaSbF_6$; 50 μL min^{-1}	EQCM-D; Q-sense analyzer (QE 401), QWEM, Autolab PGstat128 PS; 1 cm^2 AA, Au WE, Pt CE, Ag/AgCl RE.	Studying the role of the anion on the swelling characteristics of the CP film.	To calculate the mass changes in CP, experimental f and D of three different overtones (3rd, 5th, and 7th, or 5th, 7th, and 9th) were fit with Q-Tools and D-Find software using a viscoelastic model.	[132]2019
PEDOT:PSS; p-type; 170 and 300 nm	0.1 M NaCl AS/0.1 M KCl AS, in air/in N_2; 100 μL min^{-1}	EQCM-D; QX-338 Ti–Au QCM, Q-sense analyzer (QE401, Biolin Scientific AB, Sweden), Autolab PGstat128N PS; Au WE, Pt CE, Ag/AgCl RE.	Studying the efficiency of coupling between ions and electrons in polymer films. Analysis of stability during cyclic measurements. Analysis of the impact of ORR. Swelling and shrinkage analysis.	The mass change was modeled with Sauerbrey equation (for rigid films) and viscoelastic Kelvin–Voigt model (for hydrated films) using 5, 7, 9th overtones data.	[33]2018

[a] CP is the conjugated polymer; AS is the aqueous solution; QWEM is Q-sense window electrochemistry module; AA is the active area; WE is the working electrode; CE is the counter electrode; RE is the reference electrode; PS is potentiostat; PBS is phosphate-buffered saline; BSA is bovine serum albumin; FBS is fetal bovine serum; LCB1 is the engineered protein minibinder; PCBM is 6,6-phenyl-C61-butyric acid methyl ester.

particular, in OECT studies (Table 2), QCM-D is most often used to measure OMIEC channel thickness both after fabrication (in the dry state) and after immersion in electrolyte, as well as during electrochemical processes.

The QCM-D sensor simultaneously monitors the frequency of oscillations (f) and energy dissipation factor (D) across various overtones, usually $2N - 1$ of the resonance frequency, where N is natural number from 1 to 7.[76] The shear wave generated by the quartz resonator propagates into the adjacent viscoelastic medium, such as polymers, and/or viscous liquids, where its dissipation is influenced by the material's viscosity. As the wave penetrates viscous medium, its amplitude decays exponentially, reaching $1/e$ of its initial value at the penetration depth (δ):

$$\delta = \sqrt{\frac{\eta}{\pi n f_0 \rho}}, \quad (3)$$

where ρ and η are density and viscosity of the layer or medium interfacing with a QCM sensor; f_0 is the fundamental resonant frequency of the quartz crystal; n is the overtone number. Eqn (3) is the basis of the depth-sensitive QCM-D analysis. With an increasing overtone number, the penetration depth is reduced, facilitating the examination of distinct vertical sections of the investigated layer covering the sensor surface.

The changes in f and D parameters are measured for unloaded and loaded cases of QCM-D sensor. This gives shifts in the values of oscillation frequency (Δf) and dissipation (ΔD). These shifts are used to estimate the thickness and viscoelastic properties of polymer films.

In the simplest case, when changes in the acoustic energy loss of the shear wave before and after film deposition can be neglected ($\Delta D \approx 0$), the mass change is directly proportional to the shift in the resonant frequency of the sensor, in accordance with the Sauerbray relation:[118,172]

$$\frac{\Delta m}{A} = -\Delta f_n \frac{\rho_q v_q}{2 f_0^2 n}, \quad (4)$$

where (Δm) is mass change of the QCM surface load; A is the sensor active area; Δf_n is the nth harmonic oscillation frequency shift due to mass add; ρ_q and v_q are the density and the shear wave velocity of quartz crystal. The eqn (4) is applicable to thin rigid films, the characteristics of which correspond to thin dry OMIEC layers. Eqn (4) can be used if inequality $|n\,\Delta D_n/\Delta f_n| < < 4 \times 10^{-7}$ 1 Hz^{-1} is true.[173] To calculate the desired film

thickness, the measured change in the areal mass related to the QCM sensor loading should be divided by the coating density.

When interacting with an electrolyte solution, the QCM-D will measure an additional frequency shift (Δf_{liq}), which in the case of a Newtonian liquid can be accounted for using the Kanazawa equation:[119,174] $\Delta f_{liq} = -C_K\sqrt{\rho_{liq}\eta_{liq}}$, where ρ_{liq} and η_{liq} are the density and viscosity of liquid; C_K is the constant of the Kanazawa equation. It can be used for viscosity definition of electrolyte solutions. The combination of Sauerbrey and Kanazawa models is particularly useful when dealing with liquid-loaded rigid films in QCM-D measurements. This hybrid approach helps separate the effects of a rigidly attached film and the influence of the surrounding liquid's viscosity and density. However, due to hydration, a typical OMIEC film becomes soft and the approximation of the rigid film (eqn (4)) ceases to work for assessing its thickness. In some cases, at open circuit, thin hydrophobic OMIEC layers, immersed into liquid electrolytes, generally behave as rigid, compact films with minimal water uptake. However, when a sufficiently high electrochemical potential is applied, even these materials can absorb water and ions, leading to swelling and the emergence of soft-film characteristics.[41]

For a more general case, when the measured layer is sufficiently thick and/or soft ($|\Delta D_n/\Delta f_n| > 10^{-8}$ 1 Hz^{-1}),[124] it will move with a delay compared to the shear wave movement of the quartz crystal surface, which leads to additional losses in the oscillating system. As a result, the dependence of the loaded QCM resonant frequency shift on the mass change becomes nonlinear. For relatively thick and/or soft films, including OMIECs interacting with electrolytes, viscoelastic models[32,175–177] are used in most cases instead of eqn (4) to estimate their thickness, assuming that films are characterized by both elastic and viscous properties. Thus, the complex shear modulus of the OMIEC film (G^*) can be given:[178]

$$G^* = \mu + i\cdot 2\pi f\eta, \quad (5)$$

where i is imaginary unit; η and μ are film viscosity and shear modulus.

In viscoelastic model, f and D depend on of the thickness of the quartz crystal covering film, its density, viscosity, and shear modulus. In the case where the measuring film is immersed in an electrolyte, the density and viscosity of the electrolyte also influence f and D and must be taken into account in the model. To correctly determine the thickness of the OMIEC film, it is necessary to use f and D data from several overtones. Usually, a minimum of three overtones is required,[60,64,145] but to increase the accuracy of the model's agreement with experimental data, it is better to use a larger number of overtones.[32,72,147] Typically, a simplified viscoelastic Kelvin–Voigt model[178,179] is used based on eqn (5). The Kelvin–Voigt model is a parallel connection of an elastic element (a spring with a certain Young's modulus) and a viscous element (a damper described by viscosity). This is due to the parallel connection in Voigt element that the terms appear as a sum in the constitutive relation and hence in the complex modulus written in eqn (5). In QCM-D measurements, this complex modulus enters the boundary condition at the quartz–film interface through the acoustic impedance of the film $Z = (\rho G^*)^{1/2}$. To determine the relationship between the f and D shifts of a quartz sensor and the parameters of a viscoelastic film, it is necessary to solve the wave equation for the propagation of bulk shear waves in a viscoelastic medium. Even approximate solutions are quite cumbersome and can be found in ref. 172, 176 and 180.

The Kelvin–Voigt model well describes relatively homogeneous OMIEC films, including swelled OMIEC films due to the uptake of ions and water from the electrolyte. When assessing the errors in approximating the viscoelastic properties of polymer films by the model, it was shown,[177] that the most accurate measurements were made for layers with a thickness-to-wavelength ratio of shear mechanical oscillation from 0.05 to 0.20.

In the vast majority of OECT studies, listed in Table 2, authors resort to the Sauerbrei equation for thin dry OMIEC films after fabrication and to the viscoelastic Voigt model for these films after immersion in electrolyte. Indeed, in most cases the simplicity of the models used is justified by the sufficient homogeneity of the film structure, used as OECT channels. However, in some special cases, researchers propose rather complex promising structures of organic semiconductors, for example: a composite mixture of polymer (PEDOT:PSS) and Nafion inclusions;[93] CP film with ion-selective membrane interface with electrolyte;[181,182] composites of CPs and SOMSs (*e.g.*, p(g2T-TT) and $PrC_{60}MA$ mixture);[40] CPs doped by nanoparticles (*e.g.*, Au-doped PEDOT:PSS,[92] and P3HT[90]); porous CP films;[6,24] *etc.* Moreover, an initially homogeneous film, with significant active water uptake, may be subject to heterogeneous swelling.[165,183] More complex models may be required to approximate the behaviour of such films.

If the film under study has a composite structure or exhibits viscoelastic relaxation in the studying frequency range, then the extended viscoelastic Voight model should be used, where in eqn (3) the viscosity and complex shear modulus G^* of the modeled film depend on frequency.[177,184]

As an alternative to the Kelvin–Voigt model, the Maxwell model approximates viscoelastic material by a series connection of an elastic spring, and a viscous damper, elements. It describes materials with dominant fluid-like viscoelastic behaviour,[176,185] and noticeably slow stress relaxation, meaning they gradually lose stored mechanical stress over time. *E.g.*, polymer electrolytes, ionic gels, polymers in a highly hydrated state are relatively close to this approximation. Table 3 lists some models that can be used.

For OMIEC films exhibiting more complex viscoelastic behaviour or a clearly defined two-component composite or layered structure, simple Kelvin–Voigt and Maxwell models may not be sufficient for accurate approximation. These models can be enhanced by adding additional spring and damper elements, forming systems with series and parallel connections, or more complex arrangements. The three-element Zener standard linear solid model accounts for both relaxation and retardation processes.[187–189] The four-element

Table 3 Models for approximating solid and liquid layers behaviour *via* QCM-D sensor response: applications to polymers, OMIECs, biolayers, and electrolytes

Model, ref.	Main parameters	Key features	Applicability limits	Examples of materials suitable for approximation
Sauerbrey[118]	Film mass change	– Simplest model – Works only for rigid thin films – Assumes no interaction with liquid	Thin rigid films	Dry thin polymer and SOMS layers; metal(oxide) electrodes
Kanazawa[119,174]	Liquid density and viscosity	– Takes into account the influence of liquid (electrolyte) on the quartz resonator	Newtonian liquids	Electrolyte solutions
Kelvin–Voigt[178,179,186]	Film shear modulus, elasticity, viscosity	– Model of parallel connection of an elastic and a viscous element – Works for solid and viscoelastic materials – Can account for liquid interactions with the polymer film	Homogeneous viscoelastic films	Soft and/or thick polymer and biomolecular layers; OMIECs immersed in electrolytes
Maxwell[172,180,185]	Relaxation time, viscosity, elastic modulus	– Model of series connection of a spring and a viscous element – Describes materials with dominant fluid-like viscoelastic behaviour – Describes slow material relaxation	Homogeneous fluid-like viscous films. Not applicable for highly elastic or rigid films	Polymer electrolytes, ionic gels, polymers in a highly hydrated state
Zener (standard linear solid)[187–189]	Two elastic moduli, one viscosity	– In Kelvin representation consists of two systems in series: spring and dashpot in parallel; and spring – Describes both the relaxation and retardation	Suitable for materials with complex viscoelastic behaviour	Polymers with a high degree of water swelling, soft hydrogels, two-component composite/layered films
Burgers[190,191]	Two elastic and two viscous parameters	– Model of parallel and series connections of 2 spring and 2 viscous elements – Accounts for both fast and slow relaxation processes	Best for materials with dual relaxation mechanisms	Polymers with dual relaxation mechanisms, two-component composite/layered films
Extended Voigt viscoelastic model[177,192,193]	Frequency-dependent complex shear modulus	– Voigt model improved by frequency-dependent complex shear modulus – Models inhomogeneous films and liquid interactions. – Suitable for multilayer structures	Suitable for inhomogeneous or multilayer films	Polymers with varying hydration across thickness, layered OMIECs
Acoustic impedance concept[32,96,114]	Complex acoustic impedance components	– Describes the overall acoustic load on sensor from layered structure – Universal method for multilayer solid structures and liquid interactions	Suitable for multilayer and complex structures	Polymers, OMIECs on various substrates, multilayer films, interaction with electrolytes
Hydrodynamic model[194,195]	Density, viscosity, hydrodynamic force	– Describes liquid interactions with pores, particles and film fragments, including liquid trapping	Suitable for thin films-liquid interactions	Porous or fragmented polymers and membranes in electrolyte

Burgers model describes systems with two distinct relaxation mechanisms, capturing more complex time-dependent behaviour.[190,191]

A more general approach to analyzing the QCM-D response can be framed through the concept of acoustic impedance,[96,114] and suitable for multilayer structures description. In this concept, the surface acoustic impedance represents the total acoustic load (Z_L) at the interface between the resonant sensor and the film.[96] For example, for a bilayer arrangement the total acoustic load impedance is determined by the acoustic loads of the first layer (Z_{L1}), the next layer after quartz, and the subsequent layer (Z_{L2}), which is not just the sum of the impedances:

$$Z_L = \frac{Z_{L1} + Z_{L2}}{1 + Z_{L1}Z_{L2}/Z_{c1}^2}; \quad Z_{Lj} = iZ_{cj} \cdot \tan\left(2\pi f \sqrt{\frac{\rho_j}{G_j}} h_j\right), \quad (6)$$

where $Z_{cj} = \sqrt{\rho_j G_j}$ is the characteristic impedance of the j load layer; ρ_j and G_j are its density and shear modulus; h_j is thickness the j load layer. The differences in the layer's impedances (Z_{Lj}) and their characteristic impedances (Z_{cj}) are due to the reflection of acoustic waves from inter-faces of materials and interference of waves within layers. Eqn (6) can be simplified to a single-layer acoustic load model by setting $Z_L = Z_{L1}$ and $Z_{L2} = 0$, or, conversely, can be complicated by adding more Z_{Lj} layers.

The imaginary and the real parts of the acoustic load impedance change contributes to resonant frequency and dissipation factor shifts of the QCM-D sensor:[114,179]

$$\frac{\Delta f}{f} = -\frac{\mathrm{Im}(\Delta Z_L)}{n\pi Z_{cq}}; \quad \frac{\Delta D}{2} = \frac{\mathrm{Re}(\Delta Z_L)}{n\pi Z_{cq}}, \quad (7)$$

where Z_{cq} is the characteristic impedance of quartz crystal; n is the overtone number. In this approach, elastic and viscous properties of OMIECs are described by complex shear modulus based on eqn (5). In fact, the Sauerbray equation (as a special case), and the mentioned viscoelastic models can be expressed in terms of acoustic impedance with the corresponding Z_L to approximate the response of a quartz sensor (eqn (7)).

In conventional QCM-D measurements, energy dissipation is commonly expressed by D, a dimensionless quantity that

describes the ratio of energy dissipated per oscillation cycle to the energy stored in the resonator. In impedance-based QCM-D and EQCM-D implementations, however, dissipation-related losses are often quantified *via* the motional resistance of the quartz resonator (R_m), obtained from equivalent circuit modelling. The motional resistance, expressed in ohms, provides an electrical representation of mechanical and interfacial energy losses and is directly proportional to the dissipation factor.

Rarely used, the hydrodynamic model[194,195] should be involved to interpret the experimental data when the film under study is porous or fragmented and it is necessary to take into account the interaction of the electrolyte liquid with pores and film fragments. This model takes into account liquid that is trapped by the complex relief of the film.

More detailed information on the modeling of QCM-D and EQCM-D measurement results can be found in the relevant reviews,[34,131] and research papers.[96,173,180,196]

QCM-D and EQCM-D techniques allow for determination of the thickness and density of organic thin films with good accuracy by analysing f and D shifts across multiple overtones. By fitting these multi-overtone data with viscoelastic models, it is possible to extract the film's viscoelastic properties, thickness, and density. This approach provides a self-consistent and reliable method to characterise both the mechanical and mass properties of thin organic films.

Although QCM-D and EQCM-D can independently determine film density through multi-overtone viscoelastic modelling, complementary techniques such as surface plasmon resonance (SPR),[155,197] atomic force microscopy (AFM),[74] and others are sometimes employed to validate these results. SPR offers an independent and highly sensitive measurement of mass changes at the interface, enabling cross-verification of density values when combined with QCM-D data. AFM provides precise topographical mapping and direct measurements of film thickness with nanoscale spatial resolution, which is particularly useful for heterogeneous or rough films. Other commonly used methods to determine film thickness and density include ellipsometry, profilometry, and X-ray reflectometry (XRR).[198] Ellipsometry is a non-destructive optical technique that enables rapid thickness measurements for uniform thin films. Profilometry offers a straightforward mechanical approach to assess film thickness by scanning surface step heights. XRR provides detailed information on film thickness and density through analysis of X-ray reflectivity patterns.[198] Each of these techniques offers unique advantages in terms of spatial resolution, sensitivity, or compatibility with different film types. Combining these measurements with QCM-D measurements allows to increase the reliability of the extracted physical parameters.[74,155,197]

A typical example of determining changes in the mass and thickness of CP films before and during an electrochemical process is shown in Fig. 4 (adapted from ref. 145). The authors[145] performed EQCM-D studies of DTP-based semiconducting polymer (Fig. 4a and b) layers deposited on the Au-coated quartz crystal sensors as substrates and interacted with 0.1 M NaCl aqueous electrolyte. Frequency shifts (Δf) for the 5th

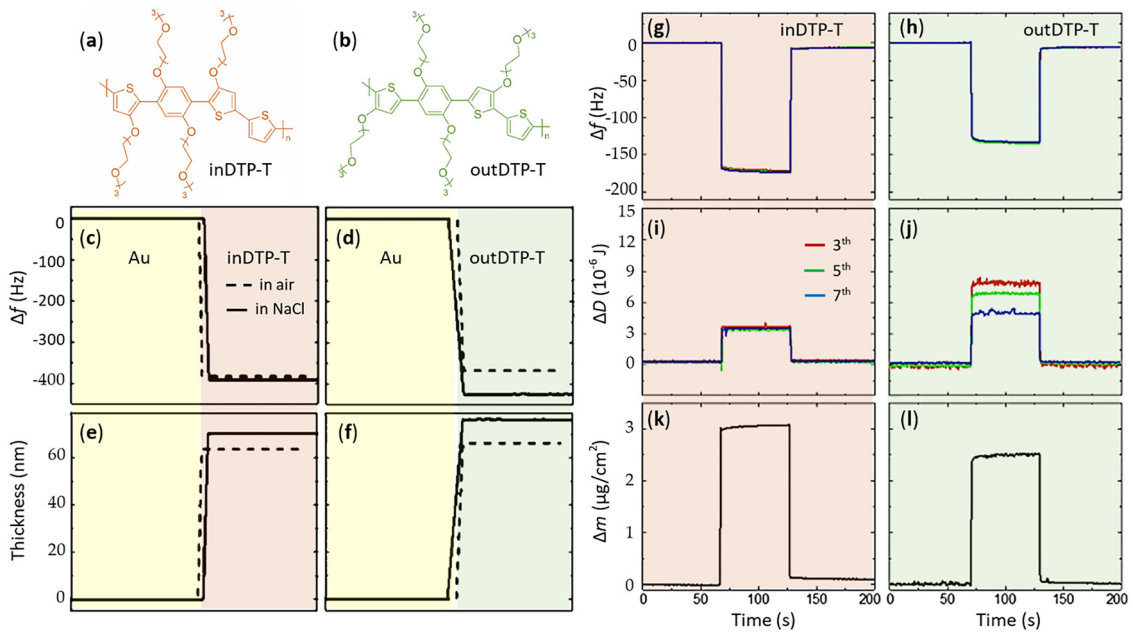

Fig. 4 Chemical structures of the studied polymers: inDTP-T (a) and outDTP-T (b). Frequency shifts (Δf) for the 5th overtone (c) and (d) and the corresponding calculated thicknesses (e) and (f) of the polymer films cast on Au coated sensors (the unloaded sensor is taken as the reference point, yellow area on the left), recorded in air (dotted line) and when immersed in 0.1 M NaCl aqueous solution (solid line), which are shown in the brown (for inDTP-T) and green (for outDTP-T) areas on the right. Measured frequency shifts (Δf) (g) and (h) and dissipation changes (ΔD) (i) and (j), and calculated mass shifts (k) and (l) for polymer films cast on Au-coated sensors, recorded in 0.1 M NaCl aqueous solution when a 60 s doping pulse is applied at a bias voltage of 0.8 V relative to the open circuit potential. The overtones shown are the 3rd (red lines), 5th (green), and 7th (blue). Adapted from ref. 145 under Creative Commons CC BY License.

overtone (n = 5) were used to calculate thicknesses of the polymer films using Sauerbrey eqn (4) before and after their immersion in electrolyte (Fig. 4c–f). The difference in the thickness of the polymer films in air and when immersed in the electrolyte indicates the passive mass uptake from the electrolyte by the films.

Applying a pulse bias of 0.8 V to oxidise the polymer layers leads to additional mass uptake (Fig. 4g–l). Authors used the 3rd, 5th, and 7th overtones to convert frequency shifts (Fig. 4g and h) and dissipation changes (Fig. 4i and j) into the mass changes (Fig. 4k and l) using the Kelvin–Voigt viscoelastic model (eqn (5)) to fit the data. It should be noted that despite the same initial thickness of the polymer films (60 nm), the same electrolyte composition (0.1 M NaCl) and the same pulse bias (60 s of 0.8 V), the change in mass turned out to be different for different polymers. The inDTP-T film increased its mass by 3.1 μg cm^{-2} upon oxidation, whereas outDTP-T only increased by 2.5 μg cm^{-2}. Authors found that the active mass uptake was in good agreement with the volumetric capacitance of the polymer layers, which were C^* = 162 and 117 F cm^{-3}, respectively. This arises from the fact that C^* reflects the amount of charge that can be stored per unit volume of the material. During electrochemical oxidation, each unit of charge stored in the OMIEC must be compensated by the ingress of counter-ions, typically accompanied by a certain amount of solvent. As a result, an OMIEC with a higher C^* will accommodate a larger quantity of ions and associated solvent molecules, leading to a proportionally greater increase in mass as detected by the EQCM. Moreover, the authors observed dissipation measurement results that could be correlated to the OECT charge carrier mobilities. This reflects the common structural origin of both charge-transport behaviour and the viscoelastic response of the conducting polymer. The microstructural features that promote efficient charge transport, such as improved backbone planarity and stronger interchain packing, also reduce viscoelastic losses, thereby giving rise to the observed correlation between mobility and the QCM sensor dissipation signal. In particular, the regiochemistry (inDTP-T *vs.* outDTP-T) influences the polymer backbone conformation, chain packing and polaron distribution, which in turn determine the mixed ionic–electronic conduction properties. InDTP-T maintains a more ordered backbone geometry and stable packing upon oxidation, which corresponds to its higher hole mobility and stable performance.[145] The inDTP-T polymer shows a substantial mass uptake during electrochemical oxidation, yet only a very small change in dissipation. The minimal dissipation shift suggests that the polymer remains mechanically robust and undergoes only limited viscoelastic softening upon doping. This behaviour is consistent with the enhanced backbone planarity and stronger interchain packing of the in-isomer, which together support more efficient polaron hopping and thus higher hole mobility. In this case, the small ΔD reflects that ionic ingress does not significantly disrupt the structural order of the film. In contrast, outDTP-T exhibits a markedly larger dissipation increase upon oxidation. This behaviour can be rationalised by the less favourable regiochemistry of the out-isomer, which results in reduced backbone planarity and weaker chain packing. Upon ionic ingress, this inherently less ordered microstructure becomes further plasticised and undergoes more pronounced viscoelastic softening. Consequently, the outDTP-T films dissipate more energy during the quartz oscillation, giving rise to a higher ΔD. This enhanced viscoelastic response is consistent with the lower charge-carrier mobility of outDTP-T, as reduced structural order and increased segmental motion hinder efficient polaron transport.

5. Water uptake and ion injection analysis during electrochemical doping/de-doping of OMIECs

Water-based electrolytes are commonly employed in OECTs due to their biocompatibility, safety and environmental friendliness. Water penetration into the OMIEC layer may occur both through direct contact with the electrolyte and as a result of electrochemical doping/de-doping, substantially affecting its characteristics. This phenomenon, commonly referred to as swelling of the OMIEC film, occurs when water molecules and electrolyte ions infiltrate the film, leading to an increase in volume and alterations in its morphology, microstructure, and ion–electron mixed transport characteristics. A distinction should be made between passive and active swelling. Passive swelling occurs as the initially dry OMIEC film transitions to a new equilibrium state upon contact with the electrolyte, driven by the spontaneous diffusion of water molecules and ions into the OMIEC matrix in the absence of an applied electric field. Active swelling, by contrast, is electrochemically induced and accompanies OMIEC doping/de-doping under an applied bias. Depending on the material properties and operating conditions, active swelling may be fully reversible upon removal of the bias or may lead to irreversible morphological and microstructural changes. Both forms of hydration have complex, sometimes controversial effects on the performance of OMIECs and play a critical role in the efficiency of conductivity modulation, and lifespan of OECT channel materials. The swelling behaviour of OMIECs is studied using EQCM-D, which provides insight into swelling mechanisms and enables quantitative, *in situ* differentiation between water and ion mass uptake during both passive and active swelling and shrinkage of OMIECs films.

Swelling analysis using EQCM-D involves several key steps. First, the frequency and dissipation response of the bare sensor is recorded in air. Next, the aqueous electrolyte solution is introduced into the measurement chamber. This step typically causes significant shifts in both frequency and dissipation due to the change in density and viscosity between air and the liquid medium. These shifts are not related to OMIEC swelling and must be accounted for or excluded to ensure accurate calculation of the swelling behaviour. After this reference measurement, the experiment is paused, and the sensors are removed. Thin OMIEC layers are then deposited directly onto

the same sensors. Once the coated sensors are reintroduced, the absolute frequency and dissipation shifts for multiple overtones are measured for both the air phase and the electrolyte phase. The Δf and ΔD shifts between the bare and OMIEC-coated sensors, under identical environmental conditions, provides a baseline for assessing mass uptake due to water and ion absorption. This procedure enables reliable quantification of swelling and allows differentiation between passive and active swelling processes when combined with electrochemical control, including parallel measurements of current, frequency shifts and dissipation under applied potential. In addition, for accurate quantitative calculations of swelling and water/ion mass uptake, it is essential to select an appropriate viscoelastic model (see Table 3) that accurately represents the behaviour of the OMIEC film during EQCM-D measurements.

Swelling of the OMIEC layer is calculated as the percentage change in total film volume (V_{total}) relative to the film volume in the dry state (V_{dry}):[37,46,140]

$$\text{Swelling} = \frac{V_{\text{total}} - V_{\text{dry}}}{V_{\text{dry}}} \times 100\%, \tag{8}$$

The mass of injected ions can be determined by calculating the number of electrons injected into the OMIEC film from the recorded working electrode transient current and assuming a 1 : 1 electron-to-ion coupling:[37,46]

$$m_{\text{ion}} = \frac{QM_{\text{ion}}}{zF}, \tag{9}$$

where m_{ion} is the mass of injected ions into the OMIEC film; Q is the total charge transferred from the working electrode; M_{ion} is the molar mass of injected ions; z is the valency number of ions; F is the Faraday constant. The value of Q can be obtained by integrating over time the current measured at the working electrode.

The amount of water uptake can be calculated by subtracting the injected ion mass from the total electrochemically absorbed mass during swelling,[37,46] assuming no other mass contributions (*e.g.*, side reactions[41]).

In the work ref. 37, the authors employed (E)QCM-D measurements to study the passive and active swelling of n-type semiconducting polymer films based on an NDI-T2 backbone and different oligoether lengths of side chains denoted here as *R*, where *R* corresponds to 1g, 2g, and 3g (Fig. 5a). Studies have shown that film swelling depends significantly on the chemical structure of p(R-NDI-T2) polymers. The authors quantified both the passive (Fig. 5b) and active (Fig. 5c and d) swelling according to eqn (8) for polymers with different R side chain lengths. Moreover, to assess passive swelling, the waiting time for the QCM-D sensor signal to stabilize took up to several hours, and the assessment of active swelling was carried out in a dynamic mode (Fig. 5d), when the polymer–electrolyte system was exposed to electric field pulses of increasing amplitude, each lasting 1 minute (Fig. 5c). The changes in mass and volume of the films in the dry and swollen states were estimated by recalculating the Δf measurements of dry films using the Sauerbrey equation, and fitting the measured Δf and ΔD data of the swollen films to the Kelvin–Voigt element. The authors also determined the injected mass of sodium ions (Fig. 5e) from a 0.1 M NaCl aqueous electrolyte based on eqn (7), assuming a 1 : 1 electron-to-ion coupling. Water uptake was estimated by subtracting the injected sodium ion mass from the total electrochemically injected mass (Fig. 5f). The results of this work highlight the importance of side chain engineering in controlling water absorption of polymer semiconductors.

In work ref. 76, electrochemical and gravimetric EQCM-D measurements were used to quantify water uptake in CP films by subtracting ion mass from the total mass gained during doping/de-doping. The authors measured the number of water molecules entering PEDOT:PSS films (Fig. 5g) at various biases in 0.1 M NaCl aqueous electrolyte. EQCM-D tracked mass changes ($\sim$1 ng cm^{-2} resolution) and viscoelastic properties ($\sim 10^{-8}$ sensitivity) by monitoring oscillation frequency and dissipation at 3rd, 5th, 7th and 9th overtones. Frequency decreases upon bias indicated significant water and ion uptake during doping/de-doping. Films with 1 wt% GOPS showed lower dissipation changes than those with 0.1 wt% GOPS, suggesting that stronger cross-linking creates a more rigid network that limits water and ion infusion. Mechanical properties influence charging dynamics, as softer, more viscous films allow faster ion uptake and capacitive charging. A viscoelastic model incorporating shear viscosity and elasticity (the Voigt element) was used to fit the data. Resulting mass changes due to ion doping and water uptake are shown in Fig. 5h and i. The study demonstrated that GOPS cross-linking enhances the structural integrity of PEDOT:PSS films. Overall, ion and water penetration increase viscosity and disorder, with water uptake having a greater impact on morphological disruption.

In many similar studies, authors have investigated swelling *via* EQCM-D and used various modifying additives and side-chain engineering approaches[60,78,164,199–201] to optimize hydration and, consequently, the morphological and mixed transport properties of CPs. Notably, the mechanisms of both passive and active swelling differ between hydrophobic, hydrophilic and amphiphilic OMIECs.[41] Hydration has both positive and negative consequences on the performance of OMIECs and significantly affects the performance and stability of OECT channel materials, which is why research into the swelling process of OECT channel materials is so important. Hydration has a positive effect if it is moderate and reversible. A hydratable OMIEC structure provides faster and easier access of ions than it occurs in close-packed structures, so swelling is necessary for more efficient injection and transport of ions in OMIECs. The negative effect of residual water in the bulk of an OMIEC film is that it prevents the formation of a relatively rich electron (hole) carrier transport paths within an organic semiconductor film.[132] Indeed, swelling of amorphous regions of the film connecting the crystalline regions will prevent the movement of charge carriers between the crystalline regions of the film. Thus, a balance must be struck in the ability of the film to absorb water. A moderate amount of hydration capacity will increase the performance of the OECT, while excess and residual water leads to electron (hole) mobility decrease and

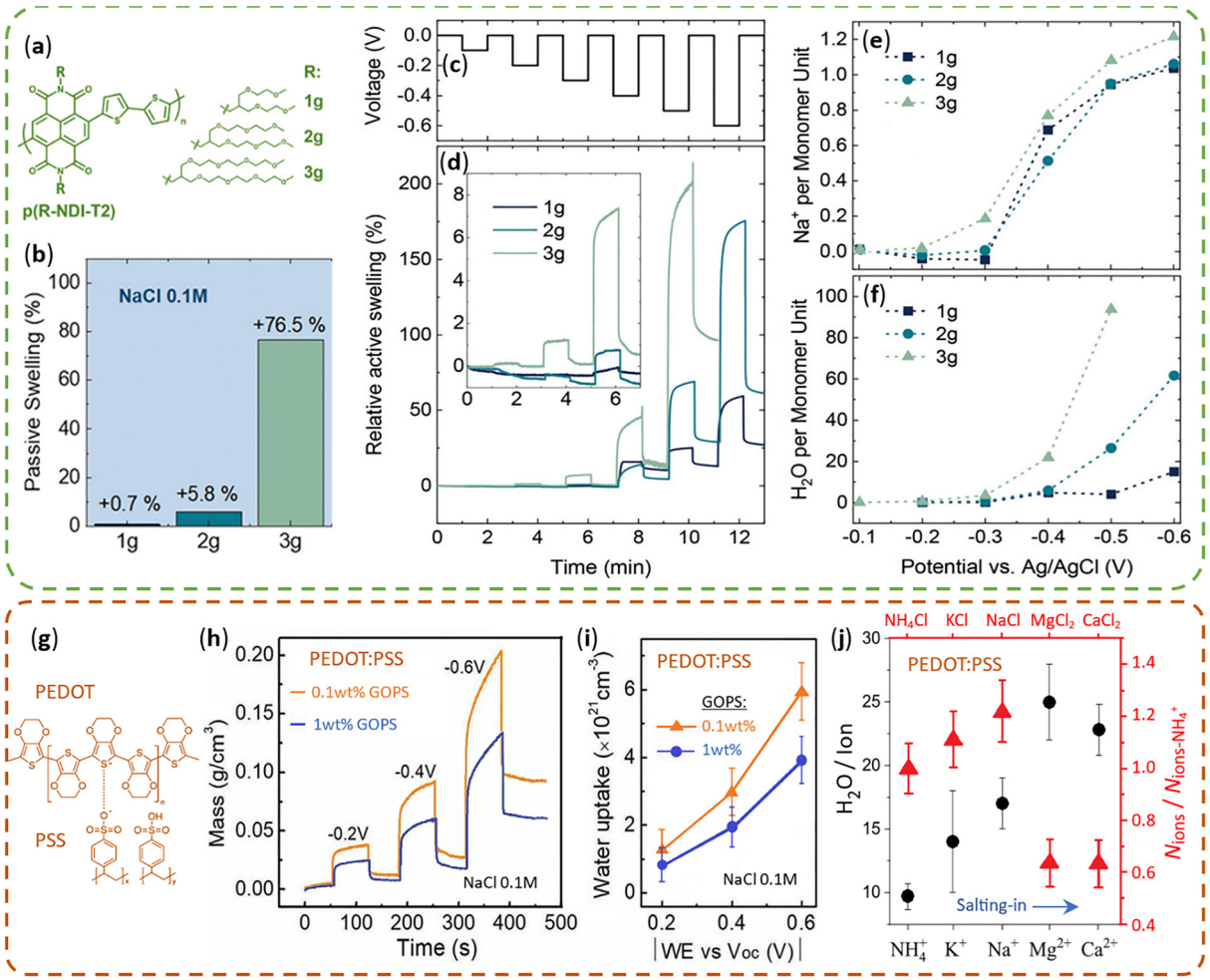

Fig. 5 The p(R-NDI-T2) polymer chemical structure with different side chain modifications (a). The p(R-NDI-T2) films passive swelling in NaCl calculated from QCM-D data (b), as well as relative active swelling during stepwise electrochemical doping (c), calculated from EQCM-D measurements (d); the inset highlights early-stage swelling. Injected Na^+ ions (e) and water uptake (f) in p(R-NDI-T2) films, calculated from EQCM-D data. Reproduced from ref. 37 with permission from John Wiley & Sons, copyright 2024. The PEDOT:PSS chemical structure (g). Mass increase (h) and water uptake (i) of the PEDOT:PSS films with different GOPS content in 0.1 M NaCl AS at different voltages calculated with the Voight model from EQCM-D data. Reproduced from ref. 76 with permission from John Wiley & Sons, copyright 2023. The number of water molecules per cation injected into the PEDOT:PSS film during the de-dope process (j, black circles), and the number of ions injected in the film normalized using the NH_4^+ as reference (j, red triangles) for the five electrolytes; adapted from ref. 36 under Creative Commons CC BY License.

irreversible morphological changes in the film and, consequently, to degradation of the device.

In other studies,[36,132,202,203] authors employed various electrolyte types and compositions to examine their effects on CP swelling and performance. Studies of ref. 202 delved into the impact of assorted potassium salts containing distinct anions on the behaviour of P3HT films and showed that anions with a more complex structure and a large effective size (*e.g.*, PF^- and $TFSI^-$) made it possible to achieve higher levels of doping compared to anions with smaller effective sizes (*e.g.*, Cl^- and ClO_4^-). It was observed that, Cl^- and ClO_4^- ions contribute about ten solvent molecules due to the formation of hydration shells; other ions such as PF^- and $TFSI^-$ penetrate the polymer film with little or no water. Using EQCM-D, the work ref. 132 showed that the electrochemical behaviour and hydration of CPs strongly depend on electrolyte–CP interaction nature. By studying p(g2T-TT) with various sodium salts, the authors found that anion size influences ion transport and structure, with doping causing irreversible changes in lattice spacing.[132] In ref. 203, a distinct study was undertaken to unravel the mechanism underlying ion-dependent charge compensation in the electrochemical doping of P3MEEMT, where the investigation unveiled the interplay of cations and anions in charge doping/de-doping processes. EQCM measurements of PEDOT:PSS films in various water-based electrolytes (NH_4Cl, KCl, NaCl, $MgCl_2$, $CaCl_2$),[36] showed that cations with greater hydration radii and bigger charge, transport into the film more water molecules per ion (Fig. 5j). These studies have contributed to understanding the swelling mechanism in which ions dissolved in water, surrounded by hydration shells, penetrate the OMIEC film and undergo drift and diffusion. This process alters the film's morphology, loosens its structure, and leads to volume

expansion. These findings help explain why different ions affect the doping/de-doping behaviour of OMIECs differently. A key factor is the amount of water accompanying each type of ion as it enters the OMIEC film. Small atomic ions with low polarizability typically enter with larger hydration shells, bringing more water into the film. In contrast, larger, more polarizable molecular ions may penetrate with fewer or no water molecules. As a result, anions with a larger effective radius (excluding hydration effects in low-polarizability ions) can enable higher doping levels in OECTs. However, active swelling is not solely attributed to the transport of water molecules within hydrated ion shells. Accurate quantification based on EQCM measurements revealed that, in the case of the BBL polymer, the amount of water absorbed exceeds the amount associated with ion hydration.[41] This indicates that, in addition to water carried by hydrated ions, the polymer matrix itself freely absorbs additional water.

6. Study the transient response, mass and charge transport kinetics during electrochemical process

Gaining insight into mass and charge transport kinetics in OMIECs during electrochemical doping/de-doping processes is essential for optimizing OECT device response time, minimizing slow relaxation processes, and improving short-term stability, that are key factors for applications in biosensing and bioelectronics. To uncover structure–property relationships under real operating conditions, recent studies have increasingly focused on the transient behaviour of OMIECs.[204,205] Direct characterisation of both charge and mass transport is particularly important for understanding OMIECs transient behaviour. However, while electronic transport is relatively accessible, mass transport kinetics remain more challenging to resolve. EQCM-D has proven effective in this task, as demonstrated in studies on P3HT films,[159] where the technique revealed slow mass transfer kinetics during electrochemical doping. The authors identified the timescale over which the doping mechanism shifts from kinetically to diffusion-controlled behaviour. Although EQCM-D cannot fully deconvolute water and ion contributions, its sub-second time resolution makes it suitable for tracking mass transport dynamics in commonly used OMIEC materials. In other works,[32,204] time-resolved EQCM-D was successfully applied to investigate charge and mass transport kinetics in both thin and thick PEDOT:PSS films.

The transient behaviour of mass and charge transport in OMIECs can be effectively studied using time-resolved EQCM-D. This technique enables simultaneous, *in situ* tracking of mass and charge changes and corresponding mechanical property variations in OMIECs under operational conditions. To perform such analysis, an OMIEC-coated piezoelectric quartz crystal should be subjected to a sequence of electrochemical potential steps while its resonant frequency and energy dissipation, as well as current through the working electrode are recorded in real time. The time-dependent frequency shifts correspond to the kinetics of mass transport (*e.g.*, ion and water uptake), while concurrent current measurements provide information on the associated charge transients. Typically, the application of a potential step results in a sharp current response followed by exponential decay, from which the resistor–capacitor (RC) time constant of the system can be extracted. The use of multiple overtones allows probing mass transport dynamics at different film depths. By normalizing mass transport and dissipation data with experimentally determined RC constants, it is possible to decouple and quantify the kinetics of ion penetration, water uptake, electrons or holes charge carrier motion, and viscoelastic properties changes in the OMIEC matrix.[32,204]

The most comprehensive example of use EQCM-D to study the mass and charge transport kinetics was published in ref. 32 (Fig. 6). In this study, the authors quantified the viscoelastic properties of PEDOT:PSS thin and thick films in contact with an aqueous electrolyte and uncovered an asymmetry between the de-doping and re-doping kinetics. They attributed this behaviour to the combination of rapid ion migration (on the subsecond timescale) and slower ion reorganisation within the CP matrix.

The kinetic parameters obtained from EQCM-D analysis were compared with those derived from electrical characterisation and structural studies of OECTs. To ensure temporal consistency between methods, the data were normalised using RC time constants. This integrative methodology enabled a detailed reconstruction of the sequential evolution of mass transport, charge modulation, and structural rearrangement processes occurring within the OECT channel during the electrochemical process. Furthermore, the transient responses of PEDOT:PSS films to potential perturbations were decomposed into three distinct subprocesses: rapid polarisation, intermediate carrier population and macroscopic transport, and a slower relaxation stage.[32] This separation highlights the interdependent ionic, electronic, and mechanical phenomena that collectively determine the functional characteristics of OMIECs under operating conditions.

Time-resolved EQCM data provide direct insight into the kinetics of charge and mass transfer in OMIEC layers. When a step potential is applied, a sharp current transient is followed by an exponential decay, from which the RC time constant is determined. As shown in Fig. 6a and b, both mass (represented by the QCM frequency shift) and charge (normalised charge density) vary during de-doping and re-doping. The mass response exhibits a two-step profile: a rapid transition within fractions of a second, and a slower process lasting up to several tens of seconds. The dominant, fast component, completing in approximately half the RC time, arises from rapid ion migration induced by the applied field (Fig. 6c1, 2, 4, 5), challenging previous assumptions that ion motion inherently limits the dynamic performance of such devices. The slower component, characterised by a smaller f increase (indicating mass loss), corresponds to the gradual reorganisation of ions and water molecules, followed by structural relaxation after charge injection (Fig. 6c3 and b).

In thicker OMIEC layers, the kinetics become spatially non-uniform, as confirmed by the overtone-dependent frequency

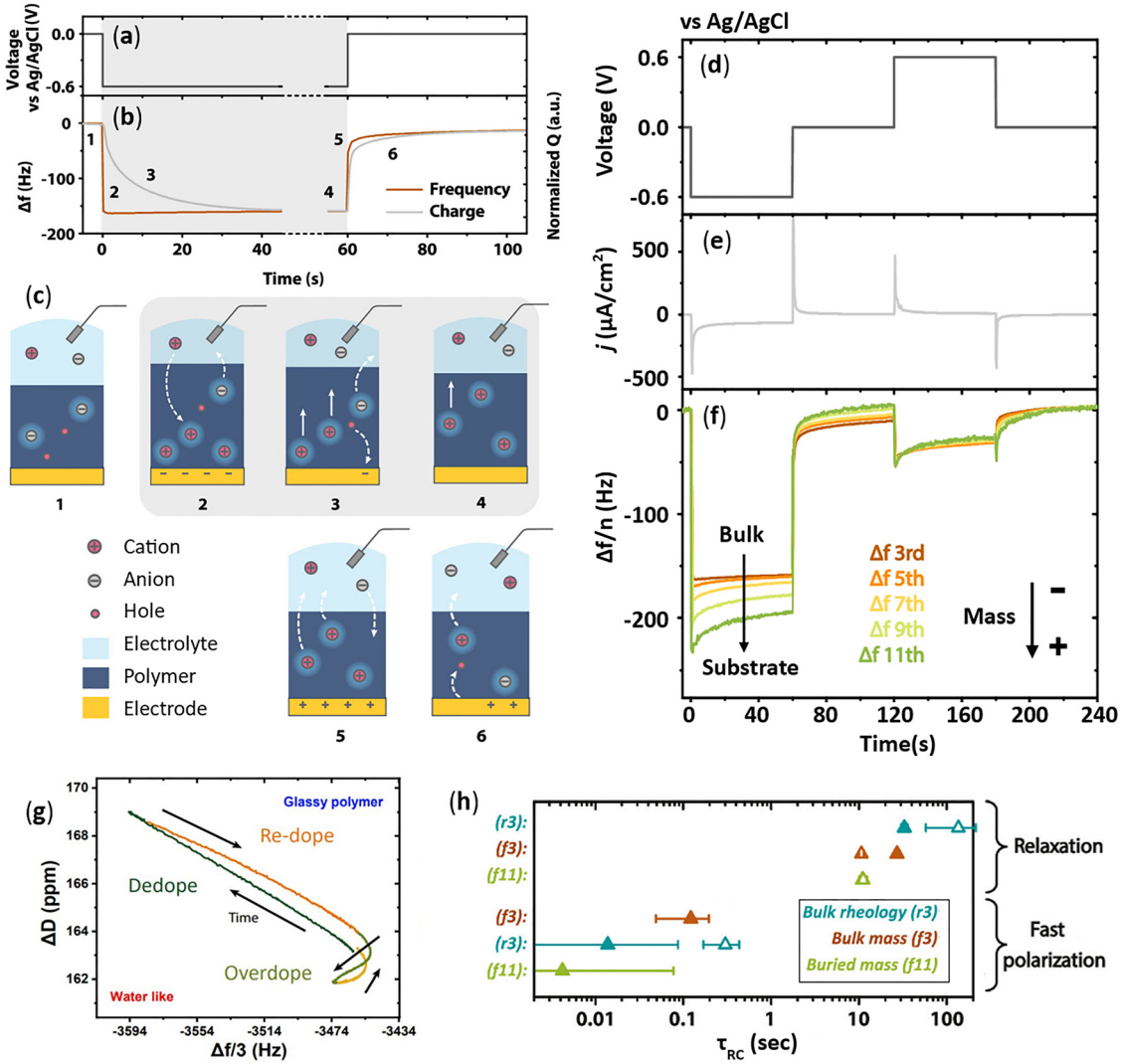

Fig. 6 (a) Potential profile during de-doping and re-doping with corresponding charging curve (grey) and third-overtone frequency shift (brown) (b). (c) Schematics of sequential steps in de-doping (1–3) and re-doping (4–5); blue halos indicate ionic hydration shells, dashed arrows show ion/charge migration, and solid arrows depict ion–water reorganisation. The grey background marks the de-doping phase. (d)–(f) Time-resolved EQCM data for a thick acid-treated PEDOT:PSS film: potential (d), current density (e), and frequency shifts of overtones—3rd (brown), 5th (orange), 7th (yellow), 9th (light green), 11th (dark green). (g) Frequency–dissipation plot from CV EQCM-D data. (h) RC-normalised time constants for de-doping (filled) and re-doping (open) processes. Reproduced from ref. 32 with permission from the American Chemical Society, copyright 2022.

characteristics (Fig. 6d–f). Higher overtones, probing regions located closer to the substrate, reveal greater mass accumulation near the electrode interface, consistent with depth profiles obtained *via* X-ray photoelectron spectroscopy (XPS). A stratified kinetic model (Fig. 6g) was proposed to describe this depth-dependent ion migration dynamics. Dissipation trajectories obtained using EQCM-D further indicate that the viscoelastic behaviour of the film develops through both fast and slow regimes. The normalised ratio of frequency shift to dissipation serves as a rheological indicator, revealing an initial liquid-like response that gradually transitions to a more solid-like state, indicative of persistent microstructural rearrangements. When normalising the kinetic parameters to RC time, three distinct time domains become apparent: fast polarisation, charge transfer, and slow mechanical relaxation (Fig. 6h). Among these, mass transfer occurs most rapidly, followed by charge redistribution and structural recovery. Upon re-doping, the fast events overlap, whereas the slower relaxation remains temporally separated and significantly delayed.

7. Study the efficiency of coupling between ionic and electronic charges and the charge storage mechanism in OMIEC films during electrochemical doping/de-doping

The efficiency of converting ionic charges to electronic charges (or holes, depending on the type of OMIEC conductivity) during

the penetration of electrolyte ions into the OMIEC film and their interaction with electrically active centers of the OMIEC material is a crucial factor influencing the performance of OECT.[33,206] This coupling efficiency impacts the ability of the OECT channel material to accumulate charges through electrochemical processes, thereby determining its capacitance. Additionally, it influences the limits and possibilities of channel conductivity modulation, which in turn affects the transconductance, a critical characteristic of OECT devices. For maximal efficiency in coupling between ionic and electronic charges, it is necessary that all injected ions contribute to the OECT channel's conductivity. However, in reality, not all electrolyte ions that penetrate into the OMIEC layer activate and contribute to conductivity changes. This activation efficiency can depend on the choice of OMIEC material, its thickness, and the composition of the electrolyte. Moreover, some ions that penetrate into the OMIEC film during doping may not be effectively removed from the OECT channel during de-doping. This incomplete reversibility in the electrochemical doping/de-doping process during cyclic operation reduces the lifetime of the transistor device. Hence, it is essential to monitor the process of ion-electron conversion and identify the associated loss mechanisms, wherein ions from the electrolyte penetrate into the OMIEC layer but do not actively participate in charge generation-recombination processes.[33] Quantitatively assessing the efficiency of ion–electron coupling in OMIECs during the doping/de-doping process poses a challenge due to multiparticle phenomena involving electrons (or holes) and ions, each possessing distinct physical properties, and charge transfer occurring across various geometric scales.[206] The analysis of ion-electron coupling is of interest for understanding the performance and stability of OECT. Insights gained from such analyses are valuable for optimizing OMIEC materials, selecting organic semiconductor–electrolyte systems, and enhancing the performance of OECT devices. EQCM-D has proven to be an excellent analytical tool for addressing these challenges, as demonstrated in the study.[33]

The use of EQCM-D enables the quantification of ion-electron coupling efficiency by simultaneously measuring two key parameters: the number of ions penetrating the film (assessed *via* the mass change of the OMIEC film, adjusted for water uptake) and the resulting current generated during the electrochemical doping/de-doping process. The measurement process is as follows: initially, in the absence of external electric fields (no electrode potentials applied), the OMIEC–electrolyte system is allowed to reach equilibrium where mass transfer between the SP film and the electrolyte stabilizes (monitored *via* QCM-D until resonance frequency and loss measurements stabilize). Subsequently, a potentiostat is connected to the QCM-D electrochemical cell, and an electrical voltage is applied to the OMIEC–electrolyte system, initiating the electrochemical doping of the film. The applied bias voltage is typically increased linearly over time, then reduced below to commence the re-verse process of electrochemical de-doping. This cyclic process repeats multiple times. During this process, the QCM-D sensor continuously monitors resonant frequency and loss values, while electric current is also measured. By employing a suitable model for the OMIEC–electrolyte system as the acoustic load on the QCM-D sensor, frequency and loss measurements are translated into changes in film mass associated with electrolyte ion injection during doping and ion escape during de-doping. These measurements are then compared with concurrent current measurements at specific voltage values. Studying the relationship between the number of ions entering the OMIEC film (derived from mass accumulation adjusted for water content) and the number of charges extracted (derived from reduction current) allows estimation of ion-to-electron coupling efficiency. This efficiency is calculated as the ratio of charges extracted from the electrode to ions injected into the OMIEC film. An efficiency ratio of unity would indicate that all injected ions contribute to the film's conductivity change, though in practice, this value typically falls below one.

One of the most striking examples of a comprehensive study based on combined EQCM-D and voltammetry measurements of PEDOT:PSS films in the 0.1 M NaCl AS is the work (Fig. 7).[33] The three-electrode EQCM-D setup included Au-coated quartz crystal sensor, potentiostat coupled with the Q-sense electrochemistry module and Ag/AgCl RE (see Table 2). During the measurements, the filtered electrolyte was continuously pumped into the chamber at a constant speed (100 μL min^{-1} flow rate), providing continuous renewal of the NaCl solution over the microacoustic sensor with PEDOT:PSS film. The authors applied a voltage to the PEDOT:PSS/electrolyte system that varied cyclically with time and had a triangular amplitude-time relationship (Fig. 7b and i), thereby subjecting the PEDOT:PSS to alternating first doping potentials (greater than the open circuit potential of 0.29 V), and then delimiting ($V <$ 0.29 V).

During cyclic doping and de-doping, both the current response (Fig. 7c and j, left axis) and the quartz crystal sensor signals were recorded simultaneously. Using the viscoelastic Kelvin–Voigt model, these data were converted into changes in the PEDOT:PSS film mass (Fig. 7c and j, right axis), reflecting the ingress and egress of ions under the applied potential. The highlighted points in Fig. 7c and j correspond to the open-circuit potential (V_{oc}). The coloured regions in Fig. 7b, c, i and j illustrate two characteristic regimes observed in the EQCM-D data curves.

In the first regime, de-doping is governed by the prevailing egress of Na^+ ions combined with the injection of Cl^-, which leads to a decrease in film mass and an increase in the current. In the second regime, occurring at negative potentials, Na^+ uptake predominates, the mass increases as cations penetrate the PEDOT:PSS–electrolyte interface and migrate towards the holes on PSS^-, while holes are removed through the underlying electrode. The extent of mass gain and the magnitude of the current are determined by the applied de-doping potential. Based on these data, a relationship was established between the number of Na^+ ions incorporated into the polymer and the charge of the extracted holes.

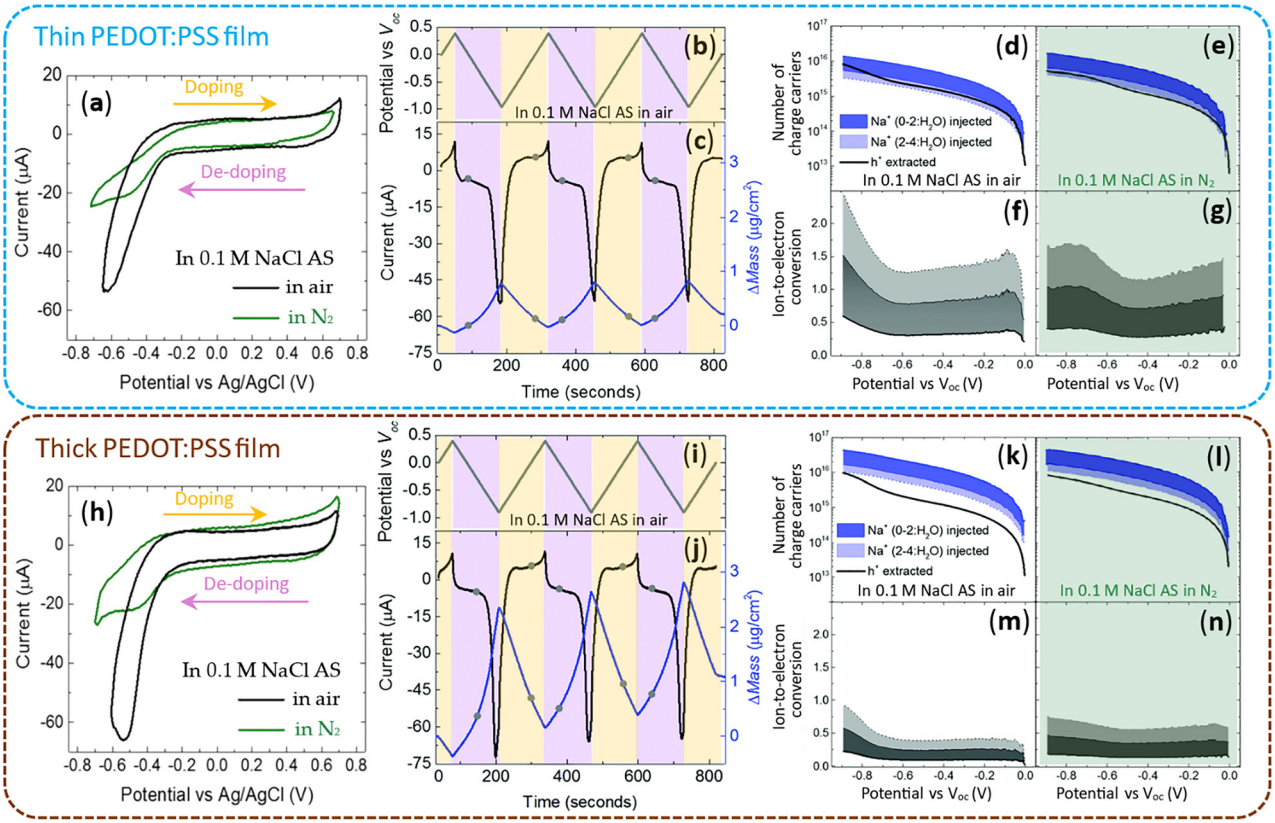

Fig. 7 An example of combined EQCM-D and CV measurements of thin (a)–(g) and thick (h)–(n) PEDOT:PSS films in contact with 0.1 M NaCl aqueous solution (AS) to evaluate the efficiency of ion-to-electron coupling: CV data (a) and (h); triangular shape of cycling potential (b) and (i) to ensure doping/de-doping processes, where V_{oc} is the open circuit potential; corresponding measurements of current and polymer film mass changes (c) and (j), where grey points mark times when $V(t) = V_{oc}$; dependence of the number of extracted holes (black line) and sodium cations introduced into PEDOT:PSS (shaded areas, the color of which becomes lighter as the amount of water involved by Na^+ increases) on the value of the de-doping potential in normal (d) and (k) and N_2 saturated environment (e) and (l); ratio of extracted holes to injected Na^+ in normal air (f) and (m) and N_2 saturated environment (g) and (n). Reproduced and adapted from ref. 33 under the Creative Commons Attribution 3.0 Licence.

To assess ion–hole coupling, the mass increase was converted into the number of injected Na^+ ions, while the number of extracted holes was derived from the reduction current (Fig. 7d and k). Since Na^+ can retain hydration shells, three scenarios were considered: bare Na^+, Na^+ coordinated to two H_2O molecules, and Na^+ coordinated to four H_2O molecules (shown by darker to lighter blue lines in Fig. 7d and k). Assuming that Na^+ substitutes for h^+:PSS^- sites in PEDOT:PSS, the total hole density was derived by considering the maximum de-doping potential (here is −0.9 V *vs.* V_{oc}), at which the number of injected Na^+ ions corresponds to the maximum number of sites capable of hosting holes. Thus, the hole density can be estimated directly from the number of injected cations, providing a physically meaningful measure of the electronic charge accumulation within the polymer. Thicker films absorb more water during de-doping than thinner ones. A sharp increase in Na^+ uptake above V_{oc} indicates efficient ion injection without a significant interfacial energy barrier.

Note, that in the earlier analysis (see eqn (9) and Fig. 5), the injected mass was estimated under the simplifying assumption of a 1 : 1 electron-to-ion coupling ratio. This first-order approximation provides a rough estimate of the mass changes associated with ionic injection but does not capture the full complexity of the coupled ionic–electronic transport processes. In contrast, the present section aims to determine the actual electron-to-ion coupling efficiency without imposing a fixed ratio.

The efficiency of ion–electron charge coupling was quantified by comparing the number of incorporated Na^+ ions with the number of extracted holes. A one-to-one ratio corresponds to complete conversion (Fig. 7f and m). For thin films, when each Na^+ ion is accompanied by two water molecules, the coupling efficiency remains nearly constant and close to unity over most of the potential range (Fig. 7c). This implies that for every extracted hole, approximately one Na^+ ion and two H_2O molecules are removed. In contrast, in thick films, this ratio at low de-doping voltages ($-0.7 < V < V_{oc}$) is around 0.2, meaning that for every removed hole, roughly three Na^+ ions and four water molecules are incorporated into the film (Fig. 7d). Therefore, although thicker films generate higher currents, a smaller fraction of the injected cations effectively participates in PEDOT reduction, indicating a decrease in ion–electron charge coupling efficiency and an increase in water co-transport.

These results demonstrate pronounced thickness-dependent variations in the interaction between Na^+ ions and PEDOT:PSS. Measurements conducted under N_2-saturated conditions (Fig. 7e, g, l and n) further reveal deviations from the data obtained under air exposure, confirming the contribution of the ORR discussed in Section 9.

8. Electrochemical stability of OMIECs: reversible and irreversible processes analysis

Ion penetration from the electrolyte into the OMIEC bulk during the electrochemical doping/de-doping process should ideally be fully reversible, as this is one of the key objectives in OMIEC development for OECT applications. However, in practice, this process can be accompanied by ion trapping,[74] irreversible morphological changes,[160] and even alterations in the chemical composition of the channel material,[17] leading to degradation of the long-term stability of OMIEC properties and, consequently, of OECT performance.

Electrochemical stability studies using EQCM-D involve monitoring changes in current, mass, and dissipation over time while subjecting the OMIEC to repeated doping and de-doping cycles. These measurements allow simultaneous evaluation of both electronic and mechanical stability, capturing processes such as irreversible mass uptake, swelling, or structural degradation. In addition, repeated EQCM-D measurements performed after long-term storage under controlled conditions can provide valuable insights into the shelf-life and long-term stability of OMIECs by revealing potential degradation or aging effects that may not be apparent under short-term cycling.

An example of using EQCM-D to study the reversibility of electrochemical processes is shown in Fig. 8a–f.[74] During 50 CV cycles with a repeated triangular voltage signal (Fig. 8b) applied to two regiorandom p-type (RRa) P3HT thin-film samples in 100 mM aqueous potassium trifluoromethanesulfonimide (KTFSI) electrolyte, the evolution of accumulated charge (Fig. 8c) and mass increase (Fig. 8d) is shown, both exhibiting a gradual rise over successive cycles. The differences between the two samples likely arise from typical batch-to-batch variations in film morphology and microstructure inherent to the spin-coating and annealing processes. These mass and charge changes indicate irreversible ion trapping, which has been independently proven by other methods.[74] The corresponding plots of all 50 CV cycles are shown in Fig. 8e, where the CV loop shape changes irreversibly from cycle to cycle. A series of AFM thickness measurements taken after every 10 CV cycles is consistent with the EQCM data, showing that the RRa P3HT film thickness increases from 53 $\pm$ 5 nm before cycling to 105 $\pm$ 12 nm after 50 cycles (Fig. 8f). The authors note that the observed irreversible ion trapping may create electron-disconnected regions upon re-doping and reduce the overall volumetric capacitance of CP films.[74]

EQCM-D studies of the hydrophobic n-type ladder polymer BBL (Fig. 8g) with different molecular weights, low molecular weight (BBL_L) and high molecular weight (BBL_H), in aqueous KCl electrolyte revealed irreversible film active swelling due to hydration during the initial electrochemical doping cycle (Fig. 8h), which persists throughout subsequent CV cycles (Fig. 8i).[41] Due to the hydrophobic nature of BBL, passive swelling was negligible. The authors explain that significant irreversible active swelling during the first reduction step creates a hydrophilic environment, enabling rapid transport of hydrated ions in subsequent cycles even in the absence of hydrophilic side chains typically employed in many other CPs. Calculations of the effects of water and cations on irreversible BBL film mass increase based on EQCM-D data indicate that it was mainly due to water uptake. Therefore, this electrochemically irreversible first step in water uptake could be regenerated on the same BBL film after drying under a vacuum.

During subsequent CV cycles, both BBL_H and BBL_L films exhibit reversible mass changes. Upon electrochemical doping, BBL_H incorporates more charge and mass, consistent with its higher volumetric capacitance. BBL_H also uptakes more cations and water compared to BBL_L. The mass data were converted into the number of water molecules per cation, showing that BBL_H incorporates 20–30 waters per cation, while BBL_L incorporates 5–7 at the doped state. Since K^+ ions typically carry about $6H_2O$ molecules in their hydration shell, the excess water in BBL_H indicates additional free water uptake during doping beyond the ion hydration shells.[41]

In another study,[160] EQCM-D was employed to assess the influence of side chain substitution on the electrochemical stability of CPs in aqueous electrolytes. A series of three polymers, based on 3,3′-dialkoxy(triethylene glycol)bithiophene (g3T2) and NDI units with varying hydrophilic-to-hydrophobic side chain ratios (Fig. 8k), were synthesized and investigated. EQCM-D measurements were initiated after the initial passive swelling reached equilibrium, and current (Fig. 8i), frequency and dissipation of energy of the CPs were monitored during cycling to quantify water uptake during charging and discharging. Continuous cycling between 0.2 and −0.4 V *vs.* Ag/AgCl was performed for three cycles at a scan rate of 10 mV s^{-1} for the p([g7:a]NDI-g3T2) polymers in a 0.1 M NaCl aqueous solution with low O_2 concentration. The corresponding, *in situ*, mass changes (Fig. 8j) were calculated from the EQCM-D data using viscoelastic model. As expected, mass increased during charging (due to cation uptake) and decreased during discharging (cation release). In addition, a net mass increase was observed after consecutive charge–discharge cycles, strongly dependent on the polarity of the side chains (Fig. 8i). For p([100:0]NDI-g3T2), baseline drift corresponded to a 343% mass increase after the first cycle, rising to 604% after three cycles. In contrast, p([90:10]NDI-g3T2) and p([75:25]NDI-g3T2) exhibited smaller mass increases of 87% to 162%, and 11% to 32%, respectively. The irreversible mass uptake was attributed to water molecules entering the polymer bulk and forming hydrogen bonds with glycol side chains; additional cation trapping may also contribute. Substitution with alkyl

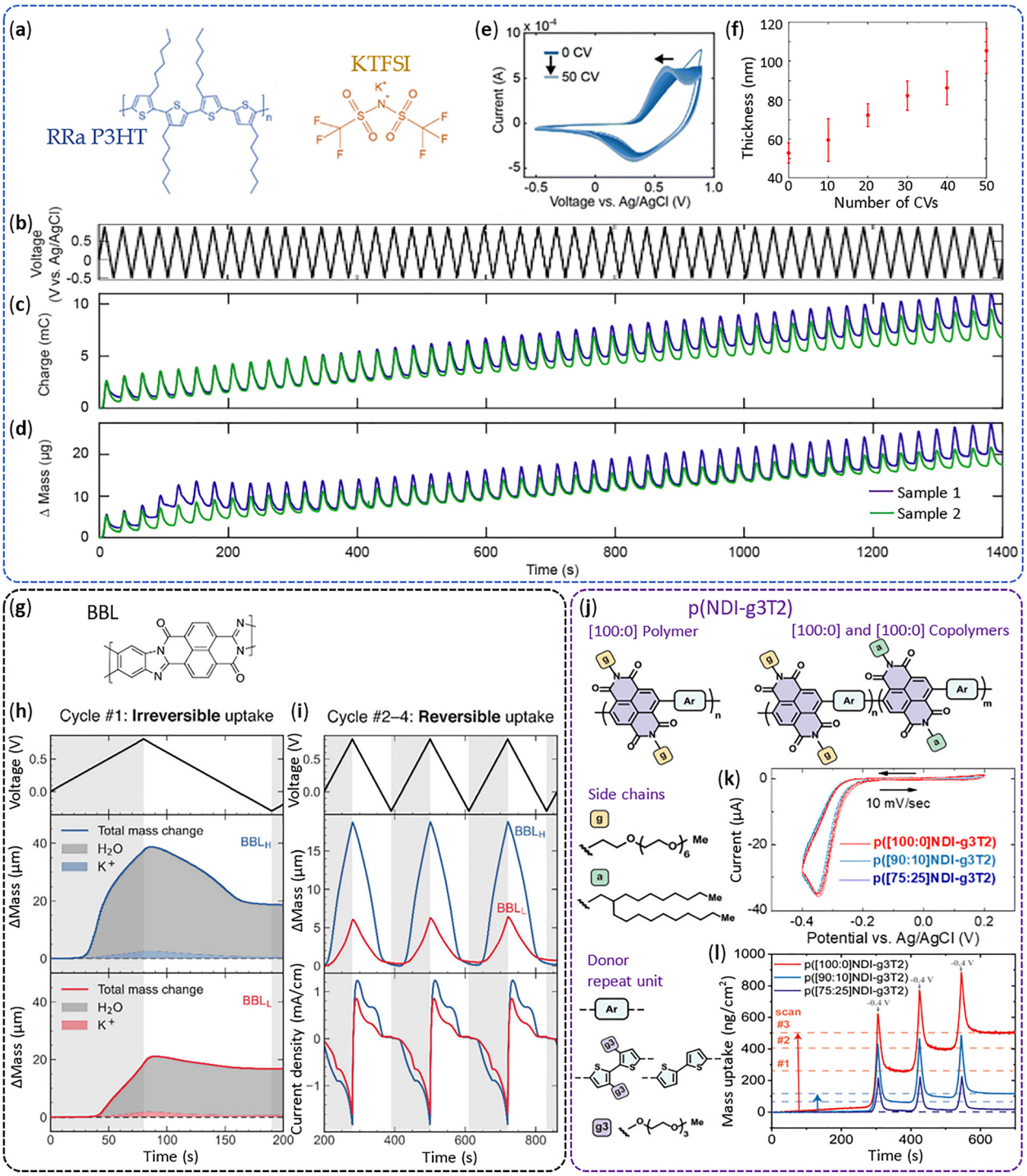

Fig. 8 Chemical structures of RRa P3HT and KTFSI (a); EQCM measurements of two RRa P3HT films in 100 mM aqueous KTFSI over 50 CV cycles: applied potential *vs.* Ag/AgCl (b), accumulated charge (c), and mass change (d), and corresponding 50 CV cycles (e). AFM measurements (in agree with the EQCM data) of film thickness after every 10 CV cycles are shown, with error bars representing standard deviations based on surface roughness (f). Reproduced from ref. 74 with permission from the Royal Society of Chemistry, copyright 2024. Chemical structure of BBL (g); irreversible (h) and reversible (i) water uptake of BBL_H and BBL_L films during the first (h) and subsequent (i) doping/de-doping cycles. Reproduced from ref. 41 with permission from the American Chemical Society, copyright 2023. Chemical structure of the polymers p([100:0]NDI-g3T2) (top left), and p([90:10]NDI-g3T2) and p([75:25]NDI-g3T2) (top right), and the side chains used (bottom) (j); EQCM-D measurements of polymer series charging to −0.4 V *vs.* Ag/AgCl in a 0.1 M NaCl with low O_2 conc.: CV (k) and mass changes (l). Reproduced from ref. 160 under the Creative Commons Attribution 4.0 (CC-BY 4.0) License.

side chains reduced swelling and mass uptake during cycling, improving electrochemical stability and enabling reversible bipolaron formation in aqueous electrolytes. At potentials below −0.4 V *vs.* Ag/AgCl, EQCM-D revealed significant changes for all polymers, suggesting a transition to a hydrogel-like state with altered mechanical properties.[160]

In several studies,[41,87] EQCM-D has been employed as an independent method to monitor OMIEC stability, particularly when degradation is linked to parasitic side reactions between the OMIEC and the electrolyte. Ideally, stable electrochemical doping and de-doping of OMIECs can be described as a reversible capacitive faradaic charging/discharging process. However, this reversibility is lost in the presence of non-capacitive faradaic processes, where side reactions and the formation of by-products alter the chemical composition of the OMIEC, ultimately affecting the performance and stability of OECTs. EQCM-D was applied to track changes in the behaviour of OMIECs in oxygen and low-oxygen environments, thereby revealing the influence of ORR induced degradation, which is discussed in more detail in Section 9.

The examples considered demonstrate the capabilities of the EQCM-D method for analyzing irreversible changes in OMIECs during electrochemical processes. Depending on the nature of OMIECs, the degree of their adhesion to the substrate, the electrode material, the type and composition of the electrolyte, and the operating modes during electrochemical doping/de-doping, the mechanisms of irreversible changes may differ. As for the main reasons for irreversible changes in OMIECs, they include irreversible morphological and microstructural changes associated with the ions trapping and irreversible absorption of excess water, degradation of the interface at the OMIEC-metal boundary and deterioration of adhesion to the substrate, and accumulation of by-products of side chemical reactions.

9. Contribution of oxygen reduction reaction to EQCM measurements of OMIECs

Although ORR with hydrogen peroxide formation does not play a key role in the primary processes governing OECT operation, it can occur under certain conditions. As a non-capacitive faradaic side reaction, ORR is typically considered a parasitic process in the context of OECTs.[87] In OECTs, ORR manifests as an electron-transfer reaction from redox-active OMIECs to molecular oxygen.[17]

The ORR can take place according to the two- and four-electron ORR pathways, one of which involves the reduction of O_2 to H_2O_2 (eqn (10a)), and the second to H_2O (eqn (10b)), respectively:

$$O_2 + 2(H^+ + e^-) \rightarrow \ldots \rightarrow H_2O_2 \quad (10a)$$

$$O_2 + 4(H^+ + e^-) \rightarrow \ldots \rightarrow 2H_2O \quad (10b)$$

The ORR proceeds through several steps *via* the formation of different reaction intermediates, which is indicated in eqn (10) by three dots. The 4-electron ORR pathway is thermodynamically more preferable than the $2e^-$ one. However, depending on the catalytic properties of some redox-active OMIECs, specifically, due to the low rate of the multistep $4e^-$ pathway, ORR may be inhibited at intermediate steps and thereby make it possible to implement a shorter H_2O_2 formation pathway.

Numerous OMIEC materials serves as a catalyst for the direct reduction of oxygen to hydrogen peroxide. *E.g.*, the mechanisms governing the PEDOT-catalyzed reduction of O_2 to H_2O_2 were investigated using *in situ* spectroscopic techniques and theoretical calculations.[207] Both approaches provided evidence for the existence of a chemisorbed reactive intermediate on the polymer chains, which kinetically favors the selective reduction reaction to produce H_2O_2. It is shown that,[208] depending on the method of polymerisation in PEDOT films ORR can proceed by the H_2O_2 and/or H_2O formation pathways. The results of the research performed on thiophene-based OECT indicate that an increase in pH during ORR leads to the degradation of the CP backbone and as a consequence to a dramatic decrease in drain current.[77] Significant oxygen degradation of n-type p(C-V) and p(C2F-V) CPs and its improvement in a N-saturated environment were demonstrated.[65] The work ref. 209 demonstrated that BBL exhibits electrocatalytic activity, fully reducing oxygen to water *via* a (2 + 2)-electron transfer mechanism, with electron transfer occurring exclusively from the reduced BBL species. Investigation of ORR in CPs with different ionisation potentials (IPs):[17] PEDOT:PSS with IP = 4 eV, p(g2T-TT) with IP = 4.5 eV and p(gPyDPP-MeOT2) with IP = 5 eV contributed to understanding ORR in OECTs in in the context IP value. Experiments on PEDOT:PSS, p(g2T-TT), and p(gPyDPP-MeOT2) using various methods demonstrated that while PEDOT:PSS and p(g2T-TT) undergo spontaneous ORR to produce H_2O_2, p(gPyDPP-MeOT2) avoids this reaction, even when exposed to a NaCl aqueous electrolyte under ambient conditions.[17]

EQCM-D enables indirect monitoring of ORR in OMIECs by simultaneously recording the electrochemical current and the corresponding Δf and ΔD shifts during CV. The mass contribution of ORR can be expected due to the formation of reaction products and changes in the layer chemical composition, and hydration state of the OMIEC layer. In addition, interactions between the OMIEC and ORR products (*e.g.* peroxide species or water) may alter the viscoelastic properties of the film, which is reflected in changes in dissipation. Moreover, the recorded current represents the total electron transfer, including both OMIEC doping/de-doping processes and ORR. During electrochemical doping, a rapid capacitive current associated with OMIEC charging is typically observed, whereas a sustained current at longer times indicates an additional contribution from ORR. Typically, the effect on current from ORR is more pronounced than changes in mass during EQCM measurements. Control experiments performed under oxygen-saturated and deoxygenated conditions allow differentiation between ORR-related processes and intrinsic ion–electron interactions within the OMIEC. Together, these correlations enable estimation of the ORR contribution to the overall electrochemical response.

In the study ref. 33, one of the goals of which was to elucidate the influence of the ORR in EQCM-D measurements, PEDOT:PSS films were subjected to cycling in a deoxygenated 0.1 M NaCl AS, which was then compared with a standard solution. The authors observed lower reduction currents with an onset around −0.25 V *vs.* Ag/AgCl in a N_2-purged environment compared to air-saturated conditions, irrespective of the film thickness. The disparity between the two environments, representing the current contribution attributable to the ORR, becomes more pronounced above −0.4 V (Fig. 7). The authors concluded that, during the reduction process, the number of cations injected into the films remains constant, independent of the occurrence of ORR. However, due to lower reduction currents, a modest decrease in ion-to-electron coupling efficiency was noted when the measurements were conducted in a N_2-saturated environment.

Subsequent works also demonstrated the ORR contribution to EQCM-D measurements of such OMIECs as: PEDOT:Tos,[72] BBL,[41] p(g2T-TT):$PrC_{60}MA$ composite films,[40] and *etc.* On the contrary, in other studies, authors tried to prevent effect of ORR on the current values in EQCM-D measurements *via* degassing electrolyte,[60] or making passivation layers.[87]

For BBL films, the impact of ORR was detected in EQCM measurements by analyzing the charge calculated from the de-doping current (Fig. 9a–c).[41] Due to the significant electrocatalytic activity of negatively doped BBL, the electrode current during doping includes contributions from both BBL reduction and oxygen reduction, causing an overestimation of the charge stored in BBL when calculated from the doping process. During de-doping, charge can be transferred either to the current collector or to the oxygen in the electrolyte, potentially leading to an underestimation of the actual BBL charge. EQCM data analysis revealed that the ORR contribution accounts for 10% to 18% of the total charge, depending on the molecular mass of the synthesized BBL.[41]

In subsequent work by other authors,[87] the use of a passivating PCBM layer was proposed to minimize the effect of ORR in BBL films. The contribution of ORR was monitored using EQCM, active swelling and penetration of ions and water were measured on BBL films and bilayer BBL/PCBM films, and non-capacitive faradaic currents on CVs were observed for the two cases of oxygen-rich and oxygen-poor electrolytes. It has been shown that the SOMS passivation layer reduces the susceptibility of BBL layer to ORR by retaining water and oxygen, but does not significantly interfere with doping.

In another study,[40] the authors investigated an ambipolar blend OMIEC composed of the p-type polymer p(g2T-TT) and the n-type small molecule fullerene derivative $PrC_{60}MA$, along with the corresponding OECT devices. Particular attention was given to the impact of ORR on the measured currents. Cyclic

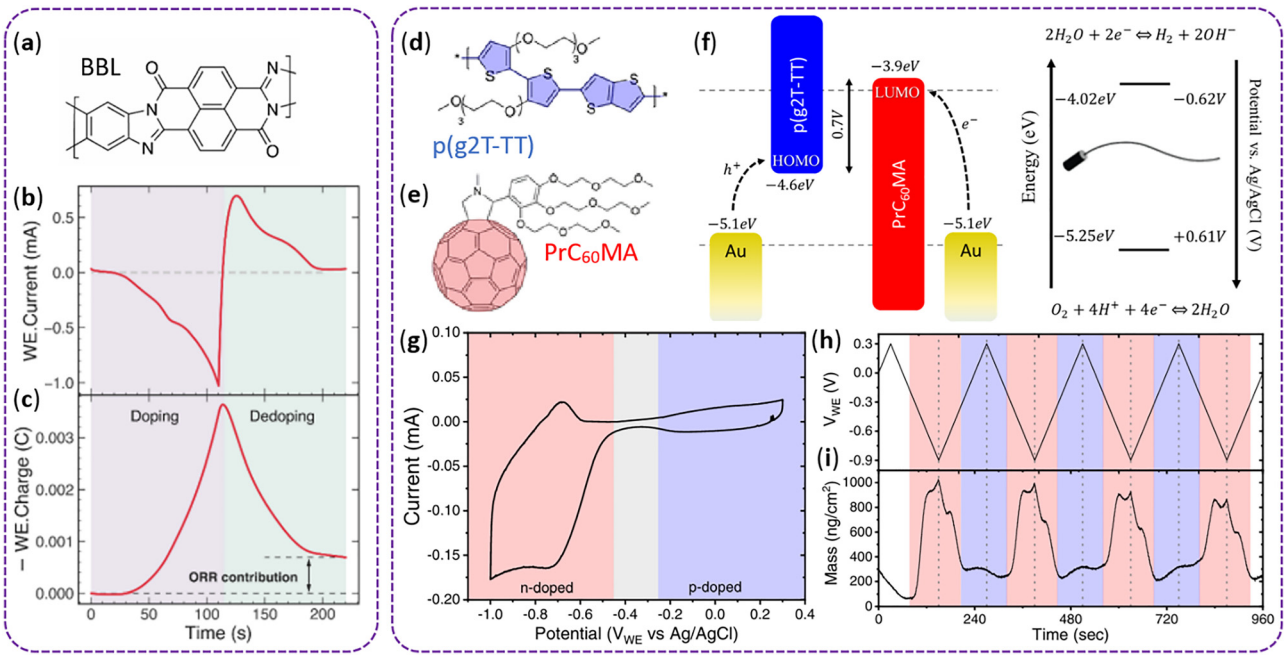

Fig. 9 Chemical structure of BBL (a), and ORR impact in the QCM measurements of BBL film: the recorded electrode current (b) and corresponding integrated charge (c). Reproduced from ref. 41 with permission from the American Chemical Society, copyright 2023. Chemical structures of the p-type polymer p(g2T-TT) (d) and the n-type fullerene derivative $PrC_{60}MA$ (e); the energy levels of p(g2T-TT) and $PrC_{60}MA$, work function of Au electrodes and the corresponding water electrochemical window at pH = 7 *vs.* Vacuum level and *vs.* Ag/AgCl reference electrode. The HOMO of p(g2T-TT) and the LUMO of $PrC_{60}MA$ are symmetric about −4.25 eV, which corresponds to a voltage of +0.35 V *vs.* Ag/AgCl (f). Cyclic voltammetry of the ambipolar 95 : 5 blend in an EQCM cell at 0.1 V s^{-1}, showing the p- and n-doped current as well as a "neutral" zone where there is no doping (g). While performing CV in an EQCM cell at 0.01 V s^{-1} (h), the mass changes in the 95 : 5 blend (i), where red areas belong to $PrC_{60}MA$ response with injection/expulsion of K^+ cations, and blue to p(g2T-TT) response with injection/expulsion of Cl^- anions. Reproduced from ref. 40 under the Creative Commons Attribution (CC BY) License.

voltammetry confirmed the electrochemical activity of both components in the blend, revealing three distinct regions corresponding to n-doping, p-doping, and film neutrality (Fig. 9g). EQCM measurements showed mass gain under both polarities within the same voltage range (Fig. 9h and i). The mass gain during p-doping was significantly lower than during n-doping ($\sim$100 *vs.* $\sim$700), reflecting the lower polymer content in the blend. To support the assignment of the low mass gain on the p-type side to chloride ion injection/extraction, the authors compared these results with EQCM data from pristine materials and blends with higher polymer content. These observations demonstrate the injection and expulsion of both anions and cations as doping agents in the same film, as confirmed by EQCM. The combined spectroelectrochemical and electrochemical results suggest no significant chemical interaction between the two blended materials, and that the steady-state doping of each component remains largely unaffected by the presence of the other, as initially hypothesized during material selection. The reduction current of $PrC_{60}MA$ includes a significant ORR contribution due to its relatively shallow LUMO level (Fig. 9f). The clear separation between the p-type and n-type signals, enabled by the large energy offset between the $PrC_{60}MA$ LUMO and the p(g2T-TT) HOMO, offers opportunities for independent tuning of the doping processes.

10. Insights into the growth mechanisms of OMIEC films: deposition, polymerisation, and assembly

OMIEC layers growth and formation kinetics study is essential for the rational design and optimisation of such films.[139,210] Understanding how OMIEC films assemble, polymerize, or deposit on substrates enables precise control over their morphology, composition, and functional properties, which critically affect their performance in bioelectronics, sensors, and other applications. QCM-D and EQCM-D are powerful, *in situ* techniques for investigating these processes in real time. These methods allow the simultaneous monitoring of mass changes and viscoelastic properties of the growing film with nanogram sensitivity and millisecond resolution, under controlled environmental or electrochemical conditions. By employing (E)QCM-D, researchers can elucidate key mechanisms such as monomer deposition, polymer chain growth, ion transport, swelling, or structural rearrangements during film formation. This level of insight is particularly valuable for tailoring OMIEC properties such as mixed conductivity, mechanical compliance, and interfacial stability. As a result, (E)QCM-D provides important insights that support the understanding and optimisation of OMIEC-based materials and devices.

Below, we discuss the electrochemical polymerisation of EDOT in more detail, as PEDOT derivatives are among the most widely used materials in the fabrication of OECT channels.

QCM-D measurements revealed four distinct stages in the growth of PEDOT films *via* vapour phase polymerisation on oxidant-coated substrates.[210] These stages differ in both mass increase rates and dissipation values, reflecting changes in growth kinetics and viscoelastic properties. The dissipation factor (Fig. 10a) serves as an indicator of the packing density and mechanical rigidity of the forming PEDOT layer: a low dissipation corresponds to a rigid, well-attached film, whereas a high dissipation indicates a soft, loosely bound layer due to increased energy damping. At the onset of polymerisation, the dissipation was initially high and decreased rapidly within the first minute, reflecting the transition from the soft, tacky Fe(III) tosylate oxidant layer to the formation of early PEDOT structures. As polymer growth proceeded, the dissipation increased again, indicating the development of a more viscoelastic film. To gain a comprehensive understanding of the growth mechanism, the authors combined QCM-D with AFM, electrical conductivity measurements, and optical transmission/electrochromic switching analysis. Stage I corresponds to the nucleation of small, loosely bound PEDOT nodules, formed under high polymerisation rates limited primarily by monomer and water vapour transport. Stage II marks the transition to a confluent layer as these nodules coalesce. Although the growth rate slows due to limited electron transport through the emerging PEDOT network, the doping level remains high, resulting in increased conductivity. In Stage III, once the percolation threshold is reached, improved interconnectivity facilitates more efficient electron transfer to oxidant sites, accelerating growth. However, this rapid polymerisation introduces structural defects along the polymer backbone, reducing doping levels and thus lowering conductivity. Stage IV is characterized by the accumulation of such defects, leading to disrupted conjugation and the formation of electrochemically inactive regions. These defect-rich areas exhibit reduced doping and poor electronic transport, resulting in further decline in conductivity and diminished redox activity. This study highlights the critical role of QCM-D in elucidating the growth kinetics and structure–property relationships of PEDOT films during vapour phase polymerisation, demonstrating that precise control of polymerisation can optimize conductivity and performance of PEDOT films and minimizing defect formation associated with late-stage growth.

Electrochemical polymerisation of EDOT monomers into PEDOT films has been extensively studied using EQCM techniques.[144,211–213]

In one of the earliest works,[212] PEDOT films were potentiostatically synthesized (1.1–1.3 V *vs.* SHE) on a gold-coated EQCM sensor from aqueous solutions containing EDOT, lithium perchlorate, and a non-ionic surfactant. EQCM monitoring during redox cycling revealed equilibrium ion exchange during reduction, while oxidation exhibited non-equilibrium behaviour, with mass changes lagging behind charge due to slow water dynamics. Approximately 40% of perchlorate ions incorporated during polymerisation remained bound within the film. Deviations from the Sauerbrey equation were attributed to viscoelastic effects, and the acoustic decay length of the

growing film was estimated at 2.45 μm. Under the studied conditions, Na^+ ions were excluded from the film, whereas tosylate anions were able to exchange with water molecules during redox cycling.

In a subsequent study,[213] electropolymerisation of EDOT in aqueous solution without surfactants was investigated using EQCM and spectroelectrochemistry. These combined techniques enabled detailed analysis of the different stages of polymer growth, including oligomer formation, chain propagation, polymer deposition with p-doping, and eventual overoxidation. Frequency–charge and absorbance–charge relationships revealed that charge consumption does not always directly correlate with PEDOT growth, highlighting the importance of careful data interpretation. The applied anodic potential critically influenced the polymerisation process, with higher potentials leading to overoxidation and charge losses unrelated to film formation. The study demonstrated the utility of EQCM and spectroelectrochemistry in resolving the complex kinetics and mechanisms of EDOT electropolymerisation.

In another investigation,[211] the electropolymerisation of EDOT was performed in KCl solution. A progressive increase in the area of the CV loops with the number of electropolymerisation cycles was observed, along with a linear correlation between the charge passed through the electrode and mass increase. These findings confirm successful growth of high-conducting PEDOT film (Fig. 10b). After 20 CV cycles, the deposited film had a cumulative charge of ~29.8 mC and a mass of ~8.4 μg. Extending to 100 CV cycles led to higher values (~77.6 mC and ~20.9 μg). However, to maintain film rigidity during later redox steps, thinner PEDOT films synthesized with 20 CV cycles were preferred. These thinner films allowed accurate mass measurements using the Sauerbrey equation, avoiding the limitations of EQCM with swelling-prone thick films.

More recently,[144] EQCM-D was employed to monitor the *in situ* formation of the phenylboronic acid-functionalized polymer PEDOT-PBA films and their subsequent behaviour under specific conditions (Fig. 10c–f). Two film types were fabricated: a non-imprinted polymer (NIP) and a molecularly imprinted polymer (MIP) in the presence of a sugar template, using the same electropolymerisation modes (1.2 V for 45 seconds). EQCM-D enabled real-time tracking of frequency and dissipation changes during polymer growth (Fig. 10c and d). The NIP film exhibited a frequency shift corresponding to a deposited mass of 12 618 ng cm^{-2} (Fig. 10e), while the MIP film showed a lower mass of 8294 ng cm^{-2} (Fig. 10f). The reduced mass in the MIP film was attributed to the presence of a non-conductive glucose template during polymerisation. An increase in dissipation during both processes indicated the deposition of soft, viscoelastic polymer films. Following template removal from the MIP was confirmed by a further mass loss (~306 ng cm^{-2}) upon washing (Fig. 10f). QCM-D analysis also revealed differences in the interaction of NIP and MIP films with glucose (Fig. 10e and f, inserts). These results demonstrated that polymerisation efficiency and film mass are influenced by the presence of template molecules, what and can be successfully used to tune the mechanical and sensing properties of the polymer film.

The discussed studies highlighted EQCM-D as a powerful tool for characterizing electropolymerisation dynamics and film properties in real time.

QCM was also employed to study the layer-by-layer (LbL) assembly on PEDOT–PAH films.[155] In this work, the assembly process began with a PSS layer, followed by poly(diallyldimethylammonium chloride) (PDDA), and the bilayer deposition was repeated several times (Fig. 10g). To quantify the mass and estimate the thickness of multilayers assembled on PEDOT–PAH-based OECTs (Fig. 10h and i), QCM measurements were performed using gold-coated 5 MHz quartz sensors with 56.6 Hz cm^2 μg^{-1} sensitivity factor.[155] A PEDOT–PAH film was first deposited onto cleaned sensors (acetone, ethanol, Milli-Q water under sonication), using the same 1 : 5 dilution protocol as for OECT fabrication. LbL assembly of PSS and PDDA was then carried out by alternating 15-minute incubations in 0.1 mg mL^{-1} polyelectrolyte solutions (in 0.1 M KCl), followed by rinsing and drying under nitrogen. All measurements were conducted under dry conditions to eliminate viscoelastic contributions from the solvent. Mass adsorption during each deposition step was observed as a decrease in resonance frequency (Fig. 10h), with PEDOT–PAH serving as the baseline reference. A small increase in dissipation (~2 Ω) after PEDOT–PAH deposition and negligible changes upon further layering indicated a predominantly elastic film behaviour. This validated the application of Sauerbrey's equation for calculating the surface mass density and estimating film thickness. The resulting thickness values are shown in Fig. 10i, calculated under the commonly assumed unit density for polyelectrolyte assemblies. The mass density changes derived from QCM closely matched SPR data for equivalent multilayers deposited on $PySO_3$-functionalized graphene FETs (Fig. 10j).[197] This agreement supports the hypothesis that beyond the initial PSS layer, which is known to penetrate the PEDOT–PAH matrix, subsequent layers are deposited uniformly on the surface, similar to assemblies on flat substrates. These results demonstrate that QCM is a robust and complementary method for monitoring LbL assembly on conducting polymer films, providing quantitative insight into mass absorption and film growth and supporting the development of OECT designs.

In addition to PEDOT, there are many examples of other OMIECs materials whose growth and formation have been successfully monitored using EQCM. *E.g.*, the QCM was used to control the formation and stability of the small molecule PCBM layer on top of a BBL film.[87] In another study,[28] the growth of self-assembled three-dimensional nanofiber arrays of SOMSs were monitored. In the work ref. 139, authors demonstrate EQCM-D capabilities in tracking and characterizing *in situ* electropolymerisation processes of conjugated trithiophene monomers such as ETE-S, ETE-PC, and their blends. During electropolymerisation, EQCM-D effectively detects distinct stages of film formation. Initial monomer adhesion to the gold electrode was observed as minor shifts in f and D. Electropolymerisation kinetics were captured during applied potential steps, revealing monomer-specific growth rates and saturation behaviours. For example, ETE-S samples show rapid

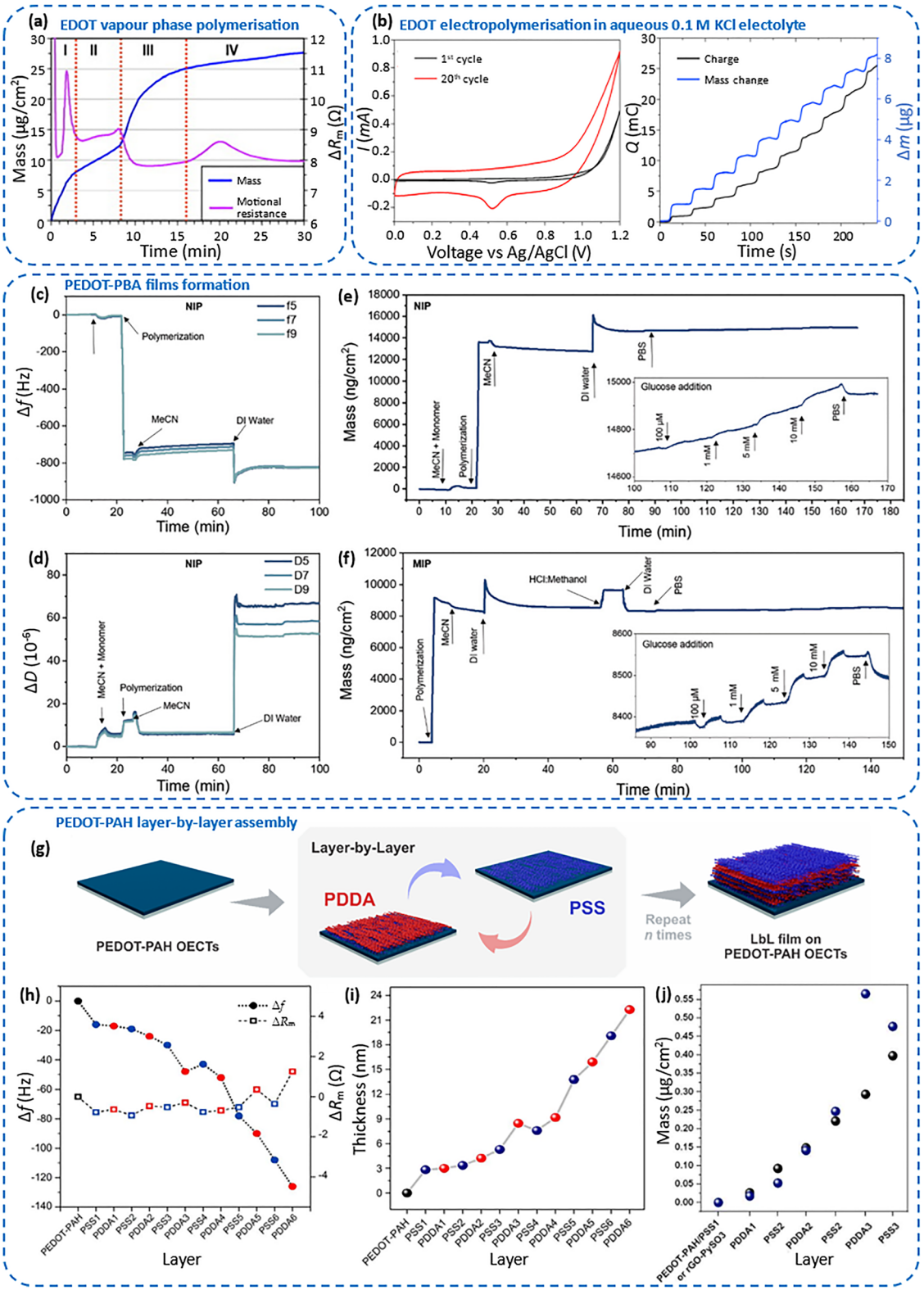

Fig. 10 QCM-D measurements of EDOT vapour phase polymerisation at 60 °C showing four distinct growth rate stages (I–IV) (a). Reproduced from ref. 210 with permission from Elsevier, copyright 2010. CV curves and corresponding charge and mass changes over time recorded during the electropolymerisation of EDOT in 0.1 M KCl aqueous electrolyte (b). Reproduced from ref. 211 with permission from Elsevier, copyright 2016. QCM-D monitoring of PEDOT-PBA film electrodeposition shows changes in frequency (c) and dissipation (d) during NIP polymerisation across multiple overtones, while the right plots present calculated mass changes for NIP (e) and MIP (f) films with insets illustrating glucose-induced mass uptake after polymerisation. Reproduced from ref. 144 under the Creative Commons Attribution (CC BY) License. Frequency and motional resistance changes during PSS/PDDA assembly on PEDOT-PAH-modified QCM (g) and (h) and corresponding film thickness at each modification step (i); PSS/PDDA assembly mass density changes from QCM (blue dots) *vs.* SPR (black dotes) data on different surfaces. Reproduced from ref. 155 with permission from the American Chemical Society, copyright 2022.

initial growth followed by saturation, while ETE-PC films grow more steadily. Swelling and structural changes in the polymer films upon potential reversal were also visible, particularly for sulfonated ETE-S films, which show a pronounced frequency decrease due to electrolyte uptake. Moreover, EQCM-D supported post-deposition analysis. After rinsing with NaCl, *via* EQCM-D authors quantified film stability by measuring the mass loss attributed to loosely bound or residual monomers. The ratio $\Delta D/\Delta f$ provides insights into film rigidity, showing clear differences between ETE-PC and ETE-S components. Coupled with Kelvin–Voigt viscoelastic modeling, EQCM-D allowed estimation of specific mass and supports calculation of gravimetric capacitance, correlating electromechanical data with electrochemical performance (from CV data). Here, EQCM-D analysis played a pivotal role in optimizing the electropolymerisation process for OECT fabrication. By correlating EQCM-D data with electrochemical performance, the authors were able to fine-tune deposition conditions and better understand how monomer composition influences film structure and stability. This analytical feedback enabled precise control over the resulting OECT properties, such as threshold voltage, through modulation of monomer ratios, ultimately supporting the rational design of high-performance OECTs.

11. Study the adhesion and delamination of OMIECs films

Adhesion between different layers and components in the device structure is critical for long-term stability. In particular, strong adhesion of OMIECs to the underlying substrate is essential to ensure reliable operation in biological recording applications.[214] Poor adhesion can lead to delamination and degradation, ultimately compromising OECT device performance.[215,216] For OMIECs, adhesion issues are especially important, as one of the key application areas for OECTs is flexible and wearable electronics, where devices must remain functional under mechanical stress. Even in the absence of additional external mechanical stress, delamination often results from mechanical mismatch between the OMIEC film and the substrate, triggered by changes in environmental conditions such as humidity, temperature, or pH.

During QCM-D monitoring, delamination of the OMIEC film can interfere with data interpretation and typically terminates further measurements. However, characteristic changes in frequency and dissipation can serve as indicators of delamination events. Thus, (E)QCM-D can also be used as a sensitive tool to assess OMIEC film adhesion to substrates.[22,89,217]

In the work ref. 217 the authors showed that the water-soluble, self-doped polymer PEDOT-S:H detaches from electrodes upon electrochemical oxidation due to a combination of swelling from ion and water uptake and internal chain rearrangements. This detachment behaviour was influenced by electrolyte properties, temperature, and pH. EQCM-D measurements provided insight into the detachment mechanism of PEDOT-S:H films by simultaneously tracking mass changes and viscoelastic properties during electrochemical oxidation. The technique revealed that detachment was preceded by significant ion and water uptake, leading to swelling and softening of the film. Mass increases were correlated with Cl^- and Na^+ intercalation, and modeling (Sauerbrey and Voigt) confirmed substantial hydration effects. The sharp rise in dissipation and frequency shifts around 600 s marked the onset of detachment.

A recent illustrative example of the analysis of OMIEC adhesion using QCM-D is given in the work,[22] where the authors studied ethylene glycol side chains with bridged-carbonyl ester in polythiophene-based CPs (Fig. 11a–c) to tune their adhesion properties. Polythiophene-based films used in OECTs typically suffer from excessive swelling and insufficient adhesion, largely due to the incorporation of PEG side chains. To address these limitations, it is essential to maintain charge-carrier mobility under swelling conditions and simultaneously enhance film-to-substrate adhesion. The authors note that improving the interfacial adhesion of polythiophene-based layers not only prevents delamination but also reduces the contact resistance between the conjugated polymer and the electrode surface, thereby improving the stability and reproducibility of the OECT's electrical characteristics. To evaluate the ion uptake/release dynamics and mechanical robustness of these conjugated polymer coatings while minimising delamination, experiments were carried out using QCM-D, following a three-step protocol during CV on quartz resonators coated with three different fabricated CP films: P1, P2, and P3 (Fig. 11d–f). The procedure comprised: initial equilibration in an AS of 0.1 M NaCl (step #1); five consecutive CV scans over the potential range from −0.5 to +0.5 V (step #2); and subsequent rinsing with the same AS (step #3). All these 3 steps are highlited in Fig. 11d–f. The experimental data show that, compared with P1 and P3, the P2 layer exhibits more pronounced and reversible ion exchange, manifested by larger shifts in resonance frequency during the second measurement step. This enhanced electrochemical response is attributed to the higher surface concentration of unbound polar PEG moieties in P2, which facilitates efficient ion transport while mitigating excessive volume expansion. Increasing the applied positive potential promoted cation penetration, reflected by substantial changes in f and D, whereas negative potentials induced ion expulsion over successive cycles. During the initial stabilisation step, P2 rapidly accommodated ions, reaching equilibrium faster than the other films. After CV cycling, P2 retained fewer residual ions, as evidenced by smaller negative f shifts than P1, indicating improved operational stability. In contrast, P3 exhibited noticeable film lifting or delamination, as indicated by a positive f shift during the rinsing phase, confirming its poorer adhesion stability.

12. Exploring OMIEC interactions with proteins, cells, glucose, and other biomaterials and biomolecules

Due to their ability to transport both ionic and electronic charge carriers, OMIECs exhibit unique properties that make

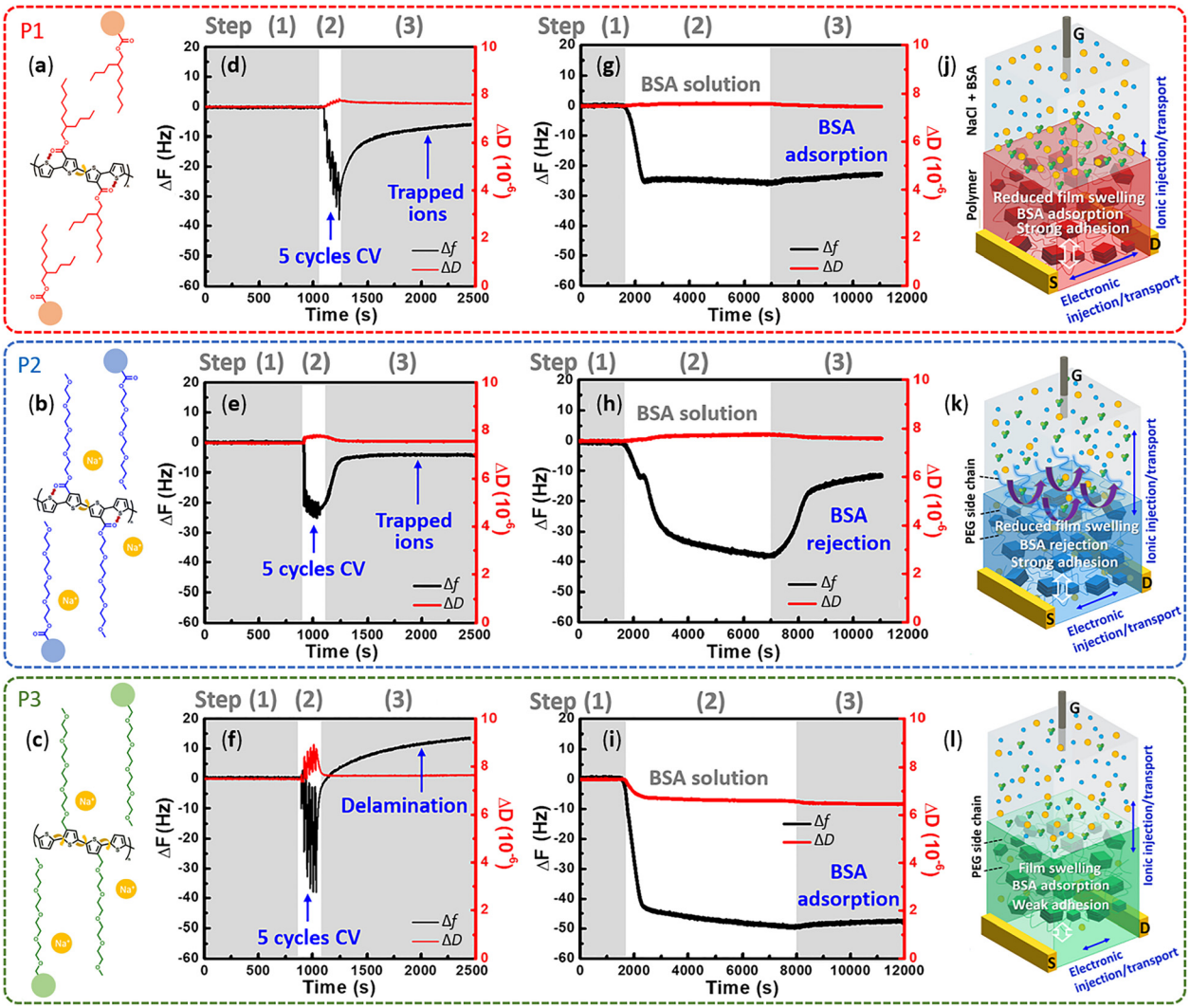

Fig. 11 Chemical structures of polythiophene-based polymers: P1 (a), P2 (b) and P3 (c). Time-resolved frequency and dissipation variations recorded from QCM-D sensors coated with polythiophene films during five CV cycles between −0.5 and +0.5 V (*vs.* Ag/AgCl) in 0.1 M NaCl aqueous solution for P1 (d), P2 (e), and P3(f). Measurements were conducted through three consecutive steps: (1) equilibration in 0.1 M NaCl, (2) five CV scans within the defined potential window, and (3) rinsing with the same electrolyte. Plots (g)–(i) depict the evaluation of BSA adsorption and desorption on P1 (g), P2(h), and P3(i) films, following a similar three-step sequence: (1) initial stabilisation, (2) BSA exposure, and (3) final washing. Schematics (j)–(l) summarise the operation of OECTs based on P1 (j), P2 (k), and P3 (l), highlighting mixed ionic–electronic transport in 0.1 M NaCl and the corresponding BSA adsorption/rejection behaviour. Reproduced from ref. 22 with permission from Elsevier, copyright 2024.

them particularly suitable for interfacing with biological systems. Understanding their interactions with proteins, cells, glucose, and other biomolecules is critical for advancing applications in biosensing, biointerfaces, and biomedical devices. QCM-D and EQCM-D are the powerful tool for probing these interactions with high sensitivity and temporal resolution.

Protein adsorption on OMIEC surfaces is particularly significant for bioelectronic applications. The use of OMIECs, rather than conventional polymers, enables the investigation of protein–material interactions under electrochemically relevant conditions.[68] Owing to their mixed ionic–electronic conduction, OMIECs can reversibly adjust their charge state in response to external bias or biomolecular binding. Protein adsorption can induce local ionic redistribution, local changes in oxidation level, and modulation of conductivity or capacitance. Consequently, QCM-D responses reflect not only variations in mass and viscoelasticity but also internal electrochemical processes such as swelling or redox transitions. When combined with electrical control (EQCM-D), these measurements reveal the coupled ion–electron dynamics and mass transfer underlying protein adsorption.[135] Additionally, the ionic and electronic states of the OMIEC can modulate surface charge and hydrophilicity. Applying a gate bias can promote or suppress protein detachment by altering electrostatic and chemical interactions at the interface. Thus, the use of organic semiconductors allows to: investigate not only the physical adsorption and detachment of proteins, but also the electrochemical interaction between the protein and the active material; study the influence of potential, ionic environment, and doping state on biocompatibility and binding; simulate

conditions of bioelectronic devices (OECT, bioelectrodes, biosensors), where mixed ion-electronic processes occur.[22]

E.g., in the work ref. 218, QCM-D was used to study how fibronectin (FN) and collagen (CG) interact with PEDOT films doped with dextran sulfate (DS), chondroitin sulfate (CS), and alginate (ALG). FN showed a two-phase adsorption: a fast initial binding followed by saturation. The highest FN adsorption was on PEDOT-DS (1287 ng cm^{-2}), while PEDOT-ALG and PEDOT-CS showed lower levels. FN formed a more rigid layer on PEDOT-DS and a softer, more hydrated layer on PEDOT-ALG. In contrast, CG showed a single-phase adsorption, with the highest adsorption on PEDOT-ALG (1935 ng cm^{-2}), followed by PEDOT-CS and PEDOT-DS. The viscoelasticity of CG layers increased with the hydrophobicity of the surface. QCM-D revealed how the chemical nature of the dopant influences protein binding and the mechanical properties of the adsorbed protein layers. Additionally, it found multi-stage adsorption behaviour of FN on some surfaces, linked to conformational changes and protein–protein interactions during layer formation.

In a later study,[219] Poly(EDOT-N^+-*co*-EDOT-COOH) copolymer films with varying ratios of positively charged EDOT-N^+ and negatively charged EDOT-COOH were synthesized and studied using QCM-D to investigate protein adsorption. Toluidine blue O staining confirmed the copolymer composition, showing that a monomer feed ratio of 8 : 2 ([EDOT-N^+] : [EDOT-COOH]) resulted in an actual 1 : 1 polymer composition. QCM-D measurements demonstrated that this composition exhibited the lowest adsorption of both bovine serum albumin (BSA: ~48 ng cm^{-2}) and lysozyme (LYZ: ~26 ng cm^{-2}). In contrast, maximum BSA adsorption (~869 ng cm^{-2}) occurred on the 1 : 1 [EDOT-N^+] : [EDOT-COOH] feed ratio, likely due to the synergistic effect of electrostatic attraction and specific recognition between BSA and COOH groups. LYZ, being positively charged, showed strongest binding to negatively charged poly(EDOT-COOH) (~301 ng cm^{-2}) due to electrostatic attraction. These findings reveal two key mechanisms of protein adsorption: (1) electrostatic interactions between protein charge and surface charge, and (2) specific molecular recognition, particularly between COOH groups and BSA. The antifouling performance of the zwitterionic copolymer at [EDOT-N^+] : [EDOT-COOH] = 8 : 2 results from a balanced combination of these effects, confirming that optimal surface charge tuning can minimize non-specific protein adsorption.

In another study,[220] QCM-D was used to investigate protein adsorption on nanopatterned PEDOT films functionalized with hydroxyl (PEDOT-OH) or phosphorylcholine (PEDOT-PC) groups. Nanostructured surfaces were fabricated using colloidal lithography with polystyrene (PS) nanospheres. Nonspecific proteins (BSA, lysozyme, cytochrome *c*) showed different adsorption behaviours depending on surface charge, roughness, and chemistry. BSA, being negatively charged, exhibited stronger adsorption on positively charged PEDOT-OH due to electrostatic attraction, while positively charged lysozyme and cytochrome *c* showed reduced binding, especially on smoother surfaces. However, nanopatterns (especially 200 nm) increased their retention *via* hydrogen bonding and physical trapping. PEDOT-PC surfaces showed lower nonspecific protein adsorption due to their antifouling properties, but nanostructuring reduced this effect by disrupting the water layer. Specific adsorption of C-reactive protein (CRP) in the presence of Ca^{2+} revealed a unique dissipation drop on PEDOT-PC, attributed to water molecule release during CRP binding. This behaviour was suppressed on nanopatterned PEDOT-PC, indicating that surface structure affects interfacial hydration and protein recognition. QCM-D thus revealed multi-step adsorption, water–protein exchange, and the role of nanostructuring in modulating protein-surface interactions.

In ref. 22, QCM-D was used to investigate the interaction of bovine serum albumin (BSA) with three polythiophene-based polymer films (P1, P2, and P3) (Fig. 11a–c) deposited on QCM-D sensors. The experimental protocol comprised three main stages, including stabilisation in 0.1 M NaCl AS (step #1), BSA adsorption (step #2), and buffer rinsing to evaluate protein adsorption and desorption behaviour (step #3) (Fig. 11g–i). QCM-D data revealed that, during the rinsing step, the P2 film demonstrated markedly improved resistance to BSA adsorption compared with P1 and P3. This antifouling performance was attributed to the presence of extended polyethylene glycol (PEG) side chains on the P2 surface, which suppress nonspecific protein attachment, an essential feature for biosensing applications. Complementary surface analyses (XPS, AFM, and time-of-flight secondary ion mass spectrometry) corroborated the QCM-D observations. Notably, QCM-D proved crucial for identifying the dynamic nature of the protein–surface interactions and differentiating the antifouling capabilities of the polymer coatings. The technique enabled real-time, label-free quantification of mass changes associated with BSA adsorption and desorption, providing valuable insight into the biointerface properties of the conducting polymer films.

EQCM-D demonstrates the unique advantage over QCM-D method: it allows simultaneous control of surface potential while monitoring protein adsorption in real time.[135] Using electrified poly(EDOT-PC) electrodes, EQCM-D revealed that C-reactive protein (CRP) binding is highly potential-dependent, increasing at both +0.5 V and −0.5 V, unlike nonspecific proteins (BSA, LYZ); ΔD measured by EQCM-D distinguished specific protein recognition (rigid layers, water release) from nonspecific adsorption (soft, hydrated layers).[135] Combined with EC-AFM, EQCM-D showed that surface potential modulates layer thickness, viscoelasticity, and packing, providing mechanistic insights inaccessible to conventional QCM-D. Overall, this work highlights EQCM-D's ability to correlate electrochemical state with protein adsorption behaviour, revealing subtle interactions between proteins and zwitterionic conducting polymers.

Similarly, OMIEC interfaces with cells can be probed using (E)QCM-D to track cell adhesion, spreading, and detachment. The electrochemical control of OMIEC properties enables the modulation of cell–surface interactions in real time, providing insights into bio-interactive OMIECs for neural and tissue engineering applications.

In the previously mentioned work,[218] QCM-D has been effectively used to investigate interactions between PC12 neural cells and PEDOT films doped with biological compounds (DS, CS, ALG). Distinct Δf and ΔD shifts were observed as cells adhered to and spread on the films, with PEDOT-DS exhibiting the largest shifts, indicating stronger binding and more extensive spreading compared with PEDOT-CS and PEDOT-ALG. Minimal or negative dissipation shifts on PEDOT-ALG suggested limited interaction and possible substrate stiffening. The QCM-D responses correlated with fluorescence microscopy, confirming that greater Δf and ΔD shifts reflected increased cell attachment and spreading. QCM-D proved highly effective in differentiating cellular responses to various PEDOT-based materials.

The later study[221] investigated how surface morphology and zwitterionic functionalisation of PEDOT films influence cellular behaviour, using QCM-D as a key analytical tool. PEDOT was modified with phosphorylcholine (PC) groups, hydrophilic headgroups that mimic cell membrane components, to control antifouling properties and cellular interactions. Smooth and nanostructured PEDOT–PC films demonstrated decreasing cell attachment with increasing PC content (50–70%), reduced spreading, increased aggregation, and, at high PC content, signs of apoptosis. Among tested lines, MG-63 cells were most tolerant to PC-rich surfaces. QCM-D provided sensitive, real-time detection of these differences, highlighting the impact of PEDOT surface chemistry and morphology on adhesion and viability.

Zwitterionic Parylene-encapsulated OECT arrays complement these approaches by providing ultralow biofouling, tissue-like wet softness, and excellent conformability.[38] QCM-D measurements on Parylene-coated sensors, monitoring Δf and ΔD at multiple harmonics, confirmed site-specific cell coupling and minimal nonspecific adsorption. Devices maintained excellent wet conformability, enabling accurate real-time detection of cells in complex biological fluids. Integrating such coatings with OMIEC devices offers a robust strategy for flexible bioelectronics with controllable biointerfaces and precise monitoring of cellular responses.

The detection of glucose and other small biomolecules constitutes an important application area for OMIECs, particularly when such materials are functionalised with selective enzymes or receptors.[152] The QCM-D and EQCM-D provides a powerful technique to investigate *in situ* the kinetics of glucose oxidation and enzyme–substrate interactions.[222] Furthermore, the combined ionic and electronic conductivity of OMIECs facilitates efficient coupling between biochemical activity and measurable electrical signals, thereby enhancing the sensitivity and overall performance of such biosensors.[222,223]

For example, QCM-D was used to monitor the adsorption of glucose oxidase (GOx) on PEDOT:PSS:PVA films, enabling quantification of immobilised enzyme mass and optimisation of the biostack architecture.[223] Frequency shifts indicated increased enzyme loading when PLL spacers were used, which enhanced sensor sensitivity and long-term stability. The technique allowed real-time observation of glucose binding, providing kinetic insights into the interaction between glucose and the organic semiconductor. QCM-D confirmed that the stacked enzyme system, with HRP/Cat as a secondary layer, prevented excess H_2O_2 from diffusing into the medium, ensuring non-toxic operation for live cell cultures while maintaining accurate glucose detection.

In another characteristic study,[152] QCM-D was employed to monitor real-time adsorption of glucose oxidase (GOx) on n-type polymer films. Surface wettability and polymer side-chain chemistry strongly influenced enzyme adsorption: hydrophobic surfaces (*e.g.*, P-75) retained the most GOx, while hydrophilic or zwitterionic surfaces (*e.g.*, P-100, P-ZI) showed lower adsorption and more flattened enzyme conformations. Δf and ΔD measurements revealed layer rigidity and packing density, with high enzyme mass correlating with clustered or denatured proteins on hydrophobic films, whereas hydrophilic films promoted softer, more uniform layers. Analysis of adsorption kinetics using QCM-D allowed distinction between high-affinity *versus* low-affinity surfaces and highlighted the role of steric hindrance and protein footprint in enzyme–polymer interactions. QCM-D results were consistent with XPS and circular dichroism analyses, confirming that surface chemistry controls enzyme loading and conformation, directly impacting the sensitivity and performance of OECT-based glucose sensors.

In the study reported in ref. 144, the glucose-binding behaviour of polymer films based on the EDOT-PBA monomer was studied *via* QCM-D (Fig. 10e and f). The NIP and MIP films were developed for non-enzymatic glucose sensing without requiring complex composite materials. QCM-D was used to assess glucose uptake, showing a dose-dependent decrease in frequency upon glucose exposure, which corresponds to mass gain from glucose binding. Although the MIP film absorbed less glucose (48 ng cm^{-2} *vs.* 79 ng cm^{-2} for NIP), it exhibited faster response stabilisation and improved signal consistency, suggesting more well-defined and selective binding characteristics. QCM-D provided critical insights into glucose–polymer interaction kinetics, confirming its value in optimising OMIEC-based glucose sensors and guiding the future design of sensor materials.

Beyond individual molecules, (E)QCM-D also facilitates the study of complex media such as blood, extracellular matrix components, or synthetic hydrogels interfacing with OMIEC films. This capability is instrumental for developing bioinspired materials and understanding biophysical phenomena at bioelectronic interfaces.

In summary, EQCM-D provides a versatile and informative platform for exploring how OMIECs interact with a wide range of biomaterials. By coupling electrochemical modulation with precise measurements of mass and viscoelasticity, researchers can gain detailed mechanistic insights into bioelectronic processes. This knowledge is crucial for the rational design of OMIEC-based OECT biosensor devices.

13. Conclusions

The application of EQCM-D has become a powerful tool for investigating the complex electrochemical, mass transport, and

mechanical processes occurring in OMIECs during doping and de-doping. Its unique ability to simultaneously monitor ionic/electronic charging processes, swelling behaviour, ion–solvent co-transport, and changes in film viscoelasticity provides valuable mechanistic insights that are not accessible through electrochemical measurements alone. EQCM-D enables quantitative analysis of reversible and irreversible mass changes, swelling-induced mechanical instabilities, and degradation pathways such as delamination or parasitic faradaic side reactions (*e.g.*, ORR), all of which critically influence OMIEC stability and OECT device performance.

Despite these advances, further development of EQCM-D methodologies is needed to fully capture the complex behaviour of modern OMIEC systems. This includes:

– *In situ* coupling with spectroscopic techniques (*e.g.*, UV-Vis, Raman, spectroelectrochemistry) to correlate mass and mechanical changes with structural and electronic transitions.

– Time-resolved measurements for analyzing transient doping processes at faster timescales, closer to real device operation.

– Integration with *in operando* OECT measurements to directly correlate EQCM-D data with device performance metrics.

– Extension to multicomponent OMIEC systems (*e.g.*, blends, dopant-host systems, ambipolar materials), where ion dynamics, phase separation, and interfacial effects become more complex.

– Advanced modeling of viscoelastic properties for better decoupling of solvent uptake, ion insertion, and mechanical softening.

Numerous OECT and OMIECs studies already include the EQCM-D as a necessary tool; however, most of them have not fully exploited its potential. We hope this review will inspire researches in the field of OMIECs and OECTs to explore the full capabilities of EQCM-D.

Author contributions

The first draft of the manuscript was written by N. M.; A. D. contributed to conceptual discussions and proofreading. L. B. edited manuscript. V. I. and L. B. supervised and were responsible for funding acquisition. All authors read and approved the final manuscript.

Conflicts of interest

There are no conflicts to declare.

Data availability

All data discussed in this review article is derived from peer-reviewed published sources, which are properly cited within the manuscript. No new datasets were created for this study. Any additional information, in case it is needed, is available from the corresponding author upon request.

Acknowledgements

This work was supported by UNLOOC HORIZON-KDT-JU-2023-IA-101140192.

References

1 S. Fabiano, L. Flagg, T. C. Hidalgo Castillo, S. Inal, L. G. Kaake, L. V. Kayser, S. T. Keene, S. Ludwigs, C. Muller, B. M. Savoie, B. Lüssem, J. L. Lutkenhaus, M. Matta, D. Meli, S. N. Patel, B. D. Paulsen, J. Rivnay and J. Surgailis, On the fundamentals of organic mixed ionic/electronic conductors, *J. Mater. Chem. C*, 2023, **11**, 14527–14539, DOI: **10.1039/D3TC03058J**.

2 Y. Wang, S. Wustoni, J. Surgailis, Y. Zhong, A. Koklu and S. Inal, Designing organic mixed conductors for electrochemical transistor applications, *Nat. Rev. Mater.*, 2024, **9**, 249–265, DOI: **10.1038/s41578-024-00652-7**.

3 P. Belleri, J. Pons, I. Tarrés, I. McCulloch, P. W. M. Blom, Z. M. Kovács-Vajna, P. Gkoupidenis and F. Torricelli, Unravelling the operation of organic artificial neurons for neuromorphic bioelectronics, *Nat. Commun.*, 2024, **15**, 5350, DOI: **10.1038/s41467-024-49668-1**.

4 C. G. Tang, R. Wu, Y. Chen, Z. Zhou, Q. He, T. Li, X. Wu, K. Hou, C. J. Kousseff, I. McCulloch and W. L. Leong, A Universal Biocompatible and Multifunctional Solid Electrolyte in p-Type and n-Type Organic Electrochemical Transistors for Complementary Circuits and Bioelectronic Interfaces, *Adv. Mater.*, 2024, 2405556, DOI: **10.1002/adma.202405556**.

5 Z. Jiang, D. Ye, L. Xiang, Z. He, X. Dai, J. Yang, Q. Xiong, Y. Ma, D. Zhi, Y. Zou, Q. Peng, S. Wang, J. Li, F. Zhang and C. Di, A drug-mediated organic electrochemical transistor for robustly reusable biosensors, *Nat. Mater.*, 2024, **23**, 1547–1555, DOI: **10.1038/s41563-024-01970-5**.

6 Z. Hu, P. Gu, X. Yang, Z. Sun, L. Lu, X. Liang, X. Zhang, Z. Deng, M. Liu, G. Zu and J. Huang, Nanoporous Conjugated Polymer Aerogel Films for High-Performance Electrochemical Transistors, *Adv. Funct. Mater.*, 2024, **34**, 2410788, DOI: **10.1002/adfm.202410788**.

7 D. A. Koutsouras, F. Torricelli and P. W. M. Blom, Submicron Vertical Channel Organic Electrochemical Transistors with Ultrahigh Transconductance, *Adv. Electron. Mater.*, 2023, **9**, 2200868, DOI: **10.1002/aelm.202200868**.

8 F. Torricelli, D. Z. Adrahtas, Z. Bao, M. Berggren, F. Biscarini, A. Bonfiglio, C. A. Bortolotti, C. D. Frisbie, E. Macchia, G. G. Malliaras, I. McCulloch, M. Moser, T.-Q. Nguyen, R. M. Owens, A. Salleo, A. Spanu and L. Torsi, Electrolyte-gated transistors for enhanced performance bioelectronics, *Nat. Rev. Methods Primers*, 2021, **1**, 66, DOI: **10.1038/s43586-021-00065-8**.

9 A. Mehrehjedy, J. Eaton, K. Tang, S. Upreti, A. Sanders, V. LaRoux, X. Gu, X. He and S. Guo, Selective and Sensitive OECT Sensors with Doped MIP-Modified GCE/MWCNT Gate Electrodes for Real-Time Detection of Serotonin,

ACS Omega, 2025, **10**, 4154–4162, DOI: **10.1021/acsomega.4c10918**.

10 F. Gentile, F. Vurro, M. Janni, R. Manfredi, F. Cellini, A. Petrozza, A. Zappettini and N. Coppedè, A Biomimetic, Biocompatible OECT Sensor for the Real-Time Measurement of Concentration and Saturation of Ions in Plant Sap, *Adv. Electron. Mater.*, 2022, **8**, 2200092, DOI: **10.1002/aelm.202200092**.

11 W. Xu, Y. Zhu, X. Zhou, H. Guo, J. Wang, R. Zhu, Z. Hu, W. Ma, X. Ma, X. Li and X. Xu, High-density, ultraflexible organic electrochemical transistor array for brain activity mapping, *J. Mater. Chem. C*, 2025, **13**, 4385–4397, DOI: **10.1039/D4TC02839B**.

12 Z. Zhou, X. Wu, T. L. D. Tam, C. G. Tang, S. Chen, K. Hou, T. Li, Q. He, J. Sit, J. Xu and W. L. Leong, Highly Stable Ladder-Type Conjugated Polymer Based Organic Electrochemical Transistors for Low Power and Signal Processing-Free Surface Electromyogram Triggered Robotic Hand Control, *Adv. Funct. Mater.*, 2024, **34**, 2305780, DOI: **10.1002/adfm.202305780**.

13 E. A. Schafer, R. Wu, D. Meli, J. Tropp, M. Moser, I. McCulloch, B. D. Paulsen and J. Rivnay, Sources and Mechanism of Degradation in p-Type Thiophene-Based Organic Electrochemical Transistors, *ACS Appl. Electron. Mater.*, 2022, **4**, 1391–1404, DOI: **10.1021/acsaelm.1c01171**.

14 J. Xu, M. Xie, X. Wu, K. Xiao, Y. Ding, L. Bai, C.-G. Huang and W. Huang, Remaining useful life prediction towards cycling stability of organic electrochemical transistors, *Mater. Res. Express*, 2024, **11**, 015101, DOI: **10.1088/2053-1591/ad20a7**.

15 X. Wu, Q. He, Z. Zhou, T. L. D. Tam, C. Tang, M. Lin, M. Moser, S. Griggs, A. Marks, S. Chen, J. Xu, I. McCulloch and W. L. Leong, Stable n-Type Perylene Derivative Ladder Polymer with Antiambipolarity for Electrically Reconfigurable Organic Logic Gates, *Adv. Mater.*, 2024, **36**, 2308823, DOI: **10.1002/adma.202308823**.

16 E. Zeglio, J. Eriksson, R. Gabrielsson, N. Solin and O. Inganäs, Highly Stable Conjugated Polyelectrolytes for Water-Based Hybrid Mode Electrochemical Transistors, *Adv. Mater.*, 2017, **29**, 1605787, DOI: **10.1002/adma.201605787**.

17 A. Giovannitti, R. B. Rashid, Q. Thiburce, B. D. Paulsen, C. Cendra, K. Thorley, D. Moia, J. T. Mefford, D. Hanifi, D. Weiyuan, M. Moser, A. Salleo, J. Nelson, I. McCulloch and J. Rivnay, Energetic Control of Redox-Active Polymers toward Safe Organic Bioelectronic Materials, *Adv. Mater.*, 2020, **32**, 1908047, DOI: **10.1002/adma.201908047**.

18 T. C. Hidalgo Castillo, M. Moser, C. Cendra, P. D. Nayak, A. Salleo, I. McCulloch and S. Inal, Simultaneous Performance and Stability Improvement of a p-Type Organic Electrochemical Transistor through Additives, *Chem. Mater.*, 2022, **34**, 6723–6733, DOI: **10.1021/acs.chemmater.2c00632**.

19 M. Skowrons, A. Schander, A. G. P. Negron and B. Lüssem, The Trade-Off between Transconductance and Speed for Vertical Organic Electrochemical Transistors, *Adv. Electron. Mater.*, 2024, **10**, 2300673, DOI: **10.1002/aelm.202300673**.

20 A. Savva, R. Hallani, C. Cendra, J. Surgailis, T. C. Hidalgo, S. Wustoni, R. Sheelamanthula, X. Chen, M. Kirkus, A. Giovannitti, A. Salleo, I. McCulloch and S. Inal, Balancing Ionic and Electronic Conduction for High-Performance Organic Electrochemical Transistors, *Adv. Funct. Mater.*, 2020, **30**, 1907657, DOI: **10.1002/adfm.201907657**.

21 N. P. Menezes, T. Nicolini, M. Barker, A. A. Mariano, C. A. Dartora, G. Wantz, N. Stingelin, M. Abbas, O. J. Dautel and D. Thuau, Improved stability of organic electrochemical transistor performance with a low swelling mixed conducting polymer: a comparative study with PEDOT:PSS, *J. Mater. Chem. C*, 2023, **11**, 6296–6300, DOI: **10.1039/D3TC00108C**.

22 H.-S. Tseng, T. Puangniyom, C.-Y. Chang, J. A. Janardhanan, H. Yu, W.-C. Chen, C.-C. Chueh and Y.-S. Hsiao, Strategically tailoring ethylene glycol side chains with bridged-carbonyl ester in polythiophene-based organic electrochemical transistors for bioelectronics, *Chem. Eng. J.*, 2024, **486**, 150371, DOI: **10.1016/j.cej.2024.150371**.

23 A. X. Chen, G. L. Esparza, I. Simon, S. P. Dunfield, Y. Qie, J. A. Bunch, R. Blau, A. Lim, H. Zhang, S. E. Brew, F. M. O'Neill, D. P. Fenning and D. J. Lipomi, Effect of Additives on the Surface Morphology, Energetics, and Contact Resistance of PEDOT:PSS, *ACS Appl. Mater. Interfaces*, 2023, **15**, 38143–38153, DOI: **10.1021/acsami.3c08341**.

24 L. Taussig, M. Ghasemi, S. Han, A. L. Kwansa, R. Li, S. T. Keene, N. Woodward, Y. G. Yingling, G. G. Malliaras, E. D. Gomez and A. Amassian, Electrostatic self-assembly yields a structurally stabilized PEDOT:PSS with efficient mixed transport and high-performance OECTs, *Matter*, 2024, **7**, 1071–1091, DOI: **10.1016/j.matt.2023.12.021**.

25 X. Wu, Q. Liu, A. Surendran, S. E. Bottle, P. Sonar and W. L. Leong, Enhancing the Electrochemical Doping Efficiency in Diketopyrrolopyrrole-Based Polymer for Organic Electrochemical Transistors, *Adv. Electron. Mater.*, 2021, **7**, 2000701, DOI: **10.1002/aelm.202000701**.

26 H. Wu, C. Yang, Q. Li, N. B. Kolhe, X. Strakosas, M. Stoeckel, Z. Wu, W. Jin, M. Savvakis, R. Kroon, D. Tu, H. Y. Woo, M. Berggren, S. A. Jenekhe and S. Fabiano, Influence of Molecular Weight on the Organic Electrochemical Transistor Performance of Ladder-Type Conjugated Polymers, *Adv. Mater.*, 2022, **34**, 2106235, DOI: **10.1002/adma.202106235**.

27 Y. Yu, G. Zhu, L. Lan, J. Chen, X. Zhu, J. Duan, S. Cong, Z. Li, Y. Wang, Z. Wang, I. McCulloch and W. Yue, n-Type Glycolated Imide-Fused Polycyclic Aromatic Hydrocarbons with High Capacity for Liquid/Solid-Electrolyte-based Electrochemical Devices, *Adv. Funct. Mater.*, 2023, **33**, 2300012, DOI: **10.1002/adfm.202300012**.

28 E. D. Quiñones, J. Yu, R.-Z. Liu, Y.-S. Li, Y.-C. Lu and Y.-S. Hsiao, Versatile Organic Electrochemical Transistors with Self-Assembled Coronene Nanofiber Arrays for the Isolation and Detection of Circulating Tumor Cells and

Enhanced Secretion of Extracellular Vesicles, *ACS Appl. Mater. Interfaces*, 2025, **17**, 33592–33605, DOI: **10.1021/acsami.5c05442**.

29 C. Zhang, J. Meng, Y. Chen, C. Hou, K. Li, Q. Zhang, Y. Li and H. Wang, Carbon nanotube/polymer hybrid film for optimizing electron transport in organic electrochemical transistor, *J. Mater. Sci.*, 2023, **58**, 15727–15737, DOI: **10.1007/s10853-023-09036-8**.

30 D. Ohayon, V. Druet and S. Inal, A guide for the characterization of organic electrochemical transistors and channel materials, *Chem. Soc. Rev.*, 2023, **52**, 1001–1023, DOI: **10.1039/D2CS00920J**.

31 D. A. Bernards and G. G. Malliaras, Steady-State and Transient Behavior of Organic Electrochemical Transistors, *Adv. Funct. Mater.*, 2007, **17**, 3538–3544, DOI: **10.1002/adfm.200601239**.

32 R. Wu, B. D. Paulsen, Q. Ma and J. Rivnay, Mass and Charge Transport Kinetics in an Organic Mixed Ionic–Electronic Conductor, *Chem. Mater.*, 2022, **34**, 9699–9710, DOI: **10.1021/acs.chemmater.2c02476**.

33 A. Savva, S. Wustoni and S. Inal, Ionic-to-electronic coupling efficiency in PEDOT:PSS films operated in aqueous electrolytes, *J. Mater. Chem. C*, 2018, **6**, 12023–12030, DOI: **10.1039/C8TC02195C**.

34 A. D. Easley, T. Ma, C. I. Eneh, J. Yun, R. M. Thakur and J. L. Lutkenhaus, A practical guide to quartz crystal microbalance with dissipation monitoring of thin polymer films, *J. Polym. Sci.*, 2022, **60**, 1090–1107, DOI: **10.1002/pol.20210324**.

35 M. V. Voinova, M. Jonson and B. Kasemo, 'Missing mass' effect in biosensor's QCM applications, *Biosens. Bioelectron.*, 2002, **17**, 835–841, DOI: **10.1016/S0956-5663(02)00050-7**.

36 R. Colucci, B. D. A. Feitosa and G. C. Faria, Impact of Ionic Species on the Performance of Pedot:PSS-Based Organic Electrochemical Transistors, *Adv. Electron. Mater.*, 2024, **10**, 2300235, DOI: **10.1002/aelm.202300235**.

37 J. Surgailis, L. Q. Flagg, L. J. Richter, V. Druet, S. Griggs, X. Wu, S. Moro, D. Ohayon, C. J. Kousseff, A. Marks, I. P. Maria, H. Chen, M. Moser, G. Costantini, I. McCulloch and S. Inal, The Role of Side Chains and Hydration on Mixed Charge Transport in n-Type Polymer Films, *Adv. Mater.*, 2024, **36**, 2313121, DOI: **10.1002/adma.202313121**.

38 S. Qian, S. Zhang, Q. Pan, Q. Sun, R. Song, Y. Zhang, S. Zhang, Z. Geng, J. Huang, L. Wang, Y. He and B. Zhu, Conformable thin film organic electrochemical transistor array featuring tissue-like softness and ultralow biofouling, *Appl. Surf. Sci.*, 2024, **660**, 160032, DOI: **10.1016/j.apsusc.2024.160032**.

39 X. Ji, X. Lin and J. Rivnay, Organic electrochemical transistors as on-site signal amplifiers for electrochemical aptamer-based sensing, *Nat. Commun.*, 2023, **14**, 1665, DOI: **10.1038/s41467-023-37402-2**.

40 E. Stein, O. Nahor, M. Stolov, V. Freger, I. M. Petruta, I. McCulloch and G. L. Frey, Ambipolar blend-based organic electrochemical transistors and inverters, *Nat. Commun.*, 2022, **13**, 5548, DOI: **10.1038/s41467-022-33264-2**.

41 J. Guo, L. Q. Flagg, D. K. Tran, S. E. Chen, R. Li, N. B. Kolhe, R. Giridharagopal, S. A. Jenekhe, L. J. Richter and D. S. Ginger, Hydration of a Side-Chain-Free n-Type Semiconducting Ladder Polymer Driven by Electrochemical Doping, *J. Am. Chem. Soc.*, 2023, **145**, 1866–1876, DOI: **10.1021/jacs.2c11468**.

42 D. Ohayon, A. Hamidi-Sakr, J. Surgailis, S. Wustoni, B. Dereli, N. Wehbe, S. Nastase, X. Chen, I. McCulloch, L. Cavallo and S. Inal, Impact of Noncompensating Ions on the Electrochemical Performance of n-Type Polymeric Mixed Conductors, *J. Am. Chem. Soc.*, 2025, **147**, 12523–12533, DOI: **10.1021/jacs.4c17579**.

43 J. Bisquert, B. Ilyassov and N. Tessler, Switching Response in Organic Electrochemical Transistors by Ionic Diffusion and Electronic Transport, *Adv. Sci.*, 2024, 2404182, DOI: **10.1002/advs.202404182**.

44 A. Shirinskaya, G. Horowitz, J. Rivnay, G. G. Malliaras and Y. Bonnassieux, Numerical Modeling of an Organic Electrochemical Transistor, *Biosensors*, 2018, **8**, 103, DOI: **10.3390/bios8040103**.

45 A. F. Paterson, H. Faber, A. Savva, G. Nikiforidis, M. Gedda, T. C. Hidalgo, X. Chen, I. McCulloch, T. D. Anthopoulos and S. Inal, On the Role of Contact Resistance and Electrode Modification in Organic Electrochemical Transistors, *Adv. Mater.*, 2019, **31**, 1902291, DOI: **10.1002/adma.201902291**.

46 J. Surgailis, A. Savva, V. Druet, B. D. Paulsen, R. Wu, A. Hamidi-Sakr, D. Ohayon, G. Nikiforidis, X. Chen, I. McCulloch, J. Rivnay and S. Inal, Mixed Conduction in an N-Type Organic Semiconductor in the Absence of Hydrophilic Side-Chains, *Adv. Funct. Mater.*, 2021, **31**, 2010165, DOI: **10.1002/adfm.202010165**.

47 S. T. Keene, A. Rao and G. G. Malliaras, The relationship between ionic–electronic coupling and transport in organic mixed conductors, *Sci. Adv.*, 2023, **9**, eadi3536, DOI: **10.1126/sciadv.adi3536**.

48 M. Berggren, X. Crispin, S. Fabiano, M. P. Jonsson, D. T. Simon, E. Stavrinidou, K. Tybrandt and I. Zozoulenko, Ion Electron–Coupled Functionality in Materials and Devices Based on Conjugated Polymers, *Adv. Mater.*, 2019, **31**, 1805813, DOI: **10.1002/adma.201805813**.

49 A. Khot and B. M. Savoie, How side-chain hydrophilicity modulates morphology and charge transport in mixed conducting polymers, *J. Polym. Sci.*, 2022, **60**, 610–620, DOI: **10.1002/pol.20210773**.

50 X. Wu, M. Stephen, T. C. Hidalgo, T. Salim, J. Surgailis, A. Surendran, X. Su, T. Li, S. Inal and W. L. Leong, Ionic-Liquid Induced Morphology Tuning of PEDOT:PSS for High-Performance Organic Electrochemical Transistors, *Adv. Funct. Mater.*, 2022, **32**, 2108510, DOI: **10.1002/adfm.202108510**.

51 F. Bonafè, M. Bazzani, B. Fraboni and T. Cramer, Dissipative charge transport in organic mixed ionic–electronic

conductor channels, *Nat. Commun.*, 2025, **16**, 2499, DOI: **10.1038/s41467-025-57528-9**.

52 P. D. Nayak, B. Dereli, D. Ohayon, S. Wustoni, T. C. Hidalgo Castillo, V. Druet, Y. Wang, A. Hama, C. Combe, S. Griggs, M. Alsufyani, R. Sheelamanthula, I. McCulloch, L. Cavallo and S. Inal, Understanding Oxygen-Induced Reactions and Their Impact on n-Type Polymeric Mixed Conductor-Based Devices, *ACS Cent. Sci.*, 2024, **10**, 2229–2241, DOI: **10.1021/acscentsci.4c00654**.

53 J. Ko, X. Wu, A. Surendran, B. T. Muhammad and W. L. Leong, Self-Healable Organic Electrochemical Transistor with High Transconductance, Fast Response, and Long-Term Stability, *ACS Appl. Mater. Interfaces*, 2020, **12**, 33979–33988, DOI: **10.1021/acsami.0c07913**.

54 O. Bardagot, B. T. DiTullio, A. L. Jones, J. Speregen, J. R. Reynolds and N. Banerji, Balancing Electroactive Backbone and Oligo(Ethylene Oxy) Side-Chain Content Improves Stability and Performance of Soluble PEDOT Copolymers in Organic Electrochemical Transistors, *Adv. Funct. Mater.*, 2025, **35**, 2412554, DOI: **10.1002/adfm.202412554**.

55 M. Li, W. Feng, Y. Lan, Y. Sun, P. Li, J. Li, W. Yang, H. Li, J. Ding and J. Chen, Effects of selenium incorporation on the performance of polythiophene based organic electrochemical transistors, *J. Mater. Chem. C*, 2024, **12**, 7935–7942, DOI: **10.1039/D4TC01226G**.

56 L. Lan, J. Chen, Y. Wang, P. Li, Y. Yu, G. Zhu, Z. Li, T. Lei, W. Yue and I. McCulloch, Facilely Accessible Porous Conjugated Polymers toward High-Performance and Flexible Organic Electrochemical Transistors, *Chem. Mater.*, 2022, **34**, 1666–1676, DOI: **10.1021/acs.chemmater.1c03797**.

57 H. Jia, Z. Huang, P. Li, S. Zhang, Y. Wang, J.-Y. Wang, X. Gu and T. Lei, Engineering donor–acceptor conjugated polymers for high-performance and fast-response organic electrochemical transistors, *J. Mater. Chem. C*, 2021, **9**, 4927–4934, DOI: **10.1039/D1TC00440A**.

58 H.-Y. Wu, J.-D. Huang, S. Y. Jeong, T. Liu, Z. Wu, T. Van Der Pol, Q. Wang, M.-A. Stoeckel, Q. Li, M. Fahlman, D. Tu, H. Y. Woo, C.-Y. Yang and S. Fabiano, Stable organic electrochemical neurons based on p-type and n-type ladder polymers, *Mater. Horiz.*, 2023, **10**, 4213–4223, DOI: **10.1039/D3MH00858D**.

59 I. Jo, D. Jeong, Y. Moon, D. Lee, S. Lee, J. Choi, D. Nam, J. H. Kim, J. Cho, S. Cho, D. Kim, H. Ahn, B. J. Kim and M. Yoon, High-Performance Organic Electrochemical Transistors Achieved by Optimizing Structural and Energetic Ordering of Diketopyrrolopyrrole-Based Polymers, *Adv. Mater.*, 2024, **36**, 2307402, DOI: **10.1002/adma.202307402**.

60 D. Ohayon, L. Q. Flagg, A. Giugni, S. Wustoni, R. Li, T. C. Hidalgo Castillo, A.-H. Emwas, R. Sheelamanthula, I. McCulloch, L. J. Richter and S. Inal, Salts as Additives: A Route to Improve Performance and Stability of n-Type Organic Electrochemical Transistors, *ACS Mater. Au*, 2023, **3**, 242–254, DOI: **10.1021/acsmaterialsau.2c00072**.

61 S. Cong, J. Chen, L. Wang, L. Lan, Y. Wang, H. Dai, H. Liao, Y. Zhou, Y. Yu, J. Duan, Z. Li, I. McCulloch and W. Yue, Donor Functionalization Tuning the N-Type Performance of Donor–Acceptor Copolymers for Aqueous-Based Electrochemical Devices, *Adv. Funct. Mater.*, 2022, **32**, 2201821, DOI: **10.1002/adfm.202201821**.

62 K. Feng, W. Shan, J. Wang, J. Lee, W. Yang, W. Wu, Y. Wang, B. J. Kim, X. Guo and H. Guo, Cyano-Functionalized n-Type Polymer with High Electron Mobility for High-Performance Organic Electrochemical Transistors, *Adv. Mater.*, 2022, **34**, 2201340, DOI: **10.1002/adma.202201340**.

63 P. Li, J. Shi, Y. Lei, Z. Huang and T. Lei, Switching p-type to high-performance n-type organic electrochemical transistors via doped state engineering, *Nat. Commun.*, 2022, **13**, 5970, DOI: **10.1038/s41467-022-33553-w**.

64 Y. Wang, G. Zhu, E. Zeglio, T. C. H. Castillo, S. Haseena, M. K. Ravva, S. Cong, J. Chen, L. Lan, Z. Li, A. Herland, I. McCulloch, S. Inal and W. Yue, n-Type Organic Electrochemical Transistors with High Transconductance and Stability, *Chem. Mater.*, 2023, **35**, 405–415, DOI: **10.1021/acs.chemmater.2c02447**.

65 Y. Wang, A. Koklu, Y. Zhong, T. Chang, K. Guo, C. Zhao, T. C. H. Castillo, Z. Bu, C. Xiao, W. Yue, W. Ma and S. Inal, Acceptor Functionalization via Green Chemistry Enables High-Performance n-Type Organic Electrochemical Transistors for Biosensing, Memory Applications, *Adv. Funct. Mater.*, 2024, **34**, 2304103, DOI: **10.1002/adfm.202304103**.

66 X. Chen, A. Marks, B. D. Paulsen, R. Wu, R. B. Rashid, H. Chen, M. Alsufyani, J. Rivnay and I. McCulloch, n-Type Rigid Semiconducting Polymers Bearing Oligo(Ethylene Glycol) Side Chains for High-Performance Organic Electrochemical Transistors, *Angew. Chem., Int. Ed.*, 2021, **60**, 9368–9373, DOI: **10.1002/anie.202013998**.

67 Y. Liang, C. Che, H. Tang, K. Zhang, L. Lan, C. Zhou, Y. Ma and F. Huang, Influence of Interaction between Electrolyte with Side-Chain Free Conjugated Polymer on the Performance of Organic Electrochemical Transistors, *ACS Appl. Mater. Interfaces*, 2024, **16**, 19977–19986, DOI: **10.1021/acsami.3c13781**.

68 S. Zhang, C. Xia, J. Wang, S. Chen, Y. Wang, S. Zhang, Z. Geng, K. Tang, A. Erdem and B. Zhu, Ready-to-Use OECT Biosensor toward Rapid and Real-Time Protein Detection in Complex Biological Environments, *ACS Sens.*, 2025, **10**, 3369–3380, DOI: **10.1021/acssensors.4c03072**.

69 S. Zhang, S.-H. Qian, G. Zhao, Q.-C. Pan, R. Song, T. Zhang, S. Zhang, Z. Geng, J. Huang, L. Wang and B. Zhu, Intrinsically Antifouling, soft and conformal bioelectronic from scalable fabrication of Thin-Film OECT arrays by zwitterionic polymers, *Chem. Eng. J.*, 2024, **483**, 148980, DOI: **10.1016/j.cej.2024.148980**.

70 R. Colucci, D. A. Koutsouras, S. Morsbach, P. Gkoupidenis, P. W. M. Blom and U. Kraft, Organic Electrochemical Transistor-Based Immunosensors for SARS-CoV-2 Detection, *ACS Appl. Electron. Mater.*, 2024, **6**, 2739–2748, DOI: **10.1021/acsaelm.4c00260**.

71 J. Cameron and P. J. Skabara, The damaging effects of the acidity in PEDOT:PSS on semiconductor device

performance and solutions based on non-acidic alternatives, *Mater. Horiz.*, 2020, **7**, 1759–1772, DOI: **10.1039/C9MH01978B**.

72 N. Delavari, J. Gladisch, I. Petsagkourakis, X. Liu, M. Modarresi, M. Fahlman, E. Stavrinidou, M. Linares and I. Zozoulenko, Water Intake and Ion Exchange in PEDOT:Tos Films upon Cyclic Voltammetry: Experimental and Molecular Dynamics Investigation, *Macromolecules*, 2021, **54**, 6552–6562, DOI: **10.1021/acs.macromol.1c00723**.

73 Š. Tumová, R. Malečková, L. Kubáč, J. Akrman, V. Enev, L. Kalina, E. Vojtková, M. Pešková, J. Víteček, M. Vala and M. Weiter, Novel highly stable conductive polymer composite PEDOT:DBSA for bioelectronic applications, *Polym. J.*, 2023, **55**, 983–995, DOI: **10.1038/s41428-023-00784-7**.

74 S. R. Jackson, G. W. Collins, R. L. Kingsford, P. W. Martin, J. N. Keller and C. G. Bischak, Disorder-to-order transition of regiorandom P3HT upon electrochemical doping, *J. Mater. Chem. C*, 2024, **12**, 9804–9813, DOI: **10.1039/D4TC01029A**.

75 T. Nicolini, J. Surgailis, A. Savva, A. D. Scaccabarozzi, R. Nakar, D. Thuau, G. Wantz, L. J. Richter, O. Dautel, G. Hadziioannou and N. Stingelin, A Low-Swelling Polymeric Mixed Conductor Operating in Aqueous Electrolytes, *Adv. Mater.*, 2021, **33**, 2005723, DOI: **10.1002/adma.202005723**.

76 Y. Zhang, B. D. Paulsen, E. A. Schafer, Q. Zeng, F. Yu, L. Yang, Y. Xue, J. Rivnay and N. Zhao, Combined Optical, Gravimetric, and Electrical Operando Investigation of Structural Variations in Polymeric Mixed Conductors, *Adv. Funct. Mater.*, 2023, **33**, 2214380, DOI: **10.1002/adfm.202214380**.

77 S. Zhang, P. Ding, T. Ruoko, R. Wu, M. Stoeckel, M. Massetti, T. Liu, M. Vagin, D. Meli, R. Kroon, J. Rivnay and S. Fabiano, Toward Stable p-Type Thiophene-Based Organic Electrochemical Transistors, *Adv. Funct. Mater.*, 2023, **33**, 2302249, DOI: **10.1002/adfm.202302249**.

78 M. Moser, T. C. Hidalgo, J. Surgailis, J. Gladisch, S. Ghosh, R. Sheelamanthula, Q. Thiburce, A. Giovannitti, A. Salleo, N. Gasparini, A. Wadsworth, I. Zozoulenko, M. Berggren, E. Stavrinidou, S. Inal and I. McCulloch, Side Chain Redistribution as a Strategy to Boost Organic Electrochemical Transistor Performance and Stability, *Adv. Mater.*, 2020, **32**, 2002748, DOI: **10.1002/adma.202002748**.

79 B. Ding, I.-Y. Jo, H. Yu, J. H. Kim, A. V. Marsh, E. Gutiérrez-Fernández, N. Ramos, C. L. Rapley, M. Rimmele, Q. He, J. Martín, N. Gasparini, J. Nelson, M.-H. Yoon and M. Heeney, Enhanced Organic Electrochemical Transistor Performance of Donor–Acceptor Conjugated Polymers Modified with Hybrid Glycol/Ionic Side Chains by Post-polymerization Modification, *Chem. Mater.*, 2023, **35**, 3290–3299, DOI: **10.1021/acs.chemmater.3c00327**.

80 P. Li and T. Lei, Molecular design strategies for high-performance organic electrochemical transistors, *J. Polym. Sci.*, 2022, **60**, 377–392, DOI: **10.1002/pol.20210503**.

81 Z. Chen, X. Ding, J. Wang, X. Guo, S. Shao and K. Feng, π-Conjugated Polymers for High-Performance Organic Electrochemical Transistors: Molecular Design Strategies, Applications and Perspectives, *Angew. Chem., Int. Ed.*, 2025, **64**, e202423013, DOI: **10.1002/anie.202423013**.

82 N. Mukhin, A. Dietzel, V. Issakov and L. Bakhchova, Balancing performance and stability characteristics in organic electrochemical transistor, *Biosens. Bioelectron.*, 2025, **281**, 117476, DOI: **10.1016/j.bios.2025.117476**.

83 K. Matura, R. D'Orsi, L. Spagnuolo, F. Mayr, M. Cobet, C. Putz, A. Operamolla and S. Tekoglu, Nanocrystalline cellulose-based mixed ionic–electronic conductor for bioelectronics, *J. Mater. Chem. C*, 2024, **12**, 16701–16713, DOI: **10.1039/D4TC03264K**.

84 M. Huang, S. Lee, I.-Y. Jo, H. Park, B. S. Shim and M.-H. Yoon, One-step wet-spinning of conducting polymer and cellulose nanofiber composites for fiber-type organic electrochemical transistors, *Carbohydr. Polym.*, 2024, **324**, 121559, DOI: **10.1016/j.carbpol.2023.121559**.

85 Y. Cho, L. Gao, Y. Yao, J. Kim, D. Zhang, G. Forti, I. Duplessis, Y. Wang, R. M. Pankow, X. Ji, J. Rivnay, T. J. Marks and A. Facchetti, Small-Molecule Mixed Ionic–Electronic Conductors for Efficient N-Type Electrochemical Transistors: Structure-Function Correlations, *Angew. Chem., Int. Ed.*, 2025, **64**, e202414180, DOI: **10.1002/anie.202414180**.

86 X. Zhu, J. Chen, R. Liu, C. Chen, J. Tan, C. Ran, Y. Wang, R. Wang, Z. Li and W. Yue, Modulating crystallinity and mixed ionic–electronic conduction properties *via* terminal side chain engineering of n-type small molecules, *J. Mater. Chem. C*, 2025, **13**, 1784–1792, DOI: **10.1039/D4TC04230A**.

87 J. Baek, J. G. Oh, K. Lee, D. Kim, D. Lee, S. B. Kim and J. Jang, Enhanced Stability of N-Type Organic Electrochemical Transistors Via Small-Molecule Passivation, *Adv. Funct. Mater.*, 2025, **35**, 2414916, DOI: **10.1002/adfm.202414916**.

88 E. Stein, S. Simotko, Y. Yadav, P. Cavassin, I. McCulloch, N. Banerji and G. L. Frey, Synergistic effects in ambipolar blends of mixed ionic–electronic conductors, *Mater. Horiz.*, 2025, **12**, 5733–5748, DOI: **10.1039/D5MH00293A**.

89 L. Q. Flagg, W. Cho, J. Woodcock, R. Li, H. W. Ro, D. M. Delongchamp and L. J. Richter, Improved Organic Electrochemical Transistors *via* Directed Crystallizable Small Molecule Templating, *Chem. Mater.*, 2024, **36**, 1352–1361, DOI: **10.1021/acs.chemmater.3c02489**.

90 P. Y. Ho, O. Ditzer, A. Solgi, H. Zhang, R. Thümmler, M. Al-Hussein, H. Kleemann, N. Sun and F. S.-C. Lissel, Boosting OECT Performance with PEGylated Gold Nanoparticles in Hydrophobic Channels, *Adv. Funct. Mater.*, 2025, **35**, 2412559, DOI: **10.1002/adfm.202412559**.

91 R. Bharti, J. Gupta, P. Rajamani, R. G. Moulick and J. Bhattacharya, Iron oxide nanoparticles/PEDOT: PSS nanocomposite-based modification of both glassy carbon electrode and flexible cotton fiber OECT for highly sensitive multi-analytes detection, *Appl. Nanosci.*, 2022, **12**, 3823–3833, DOI: **10.1007/s13204-022-02565-9**.

92 L. Zhang, L. Wang, S. He, C. Zhu, Z. Gong, Y. Zhang, J. Wang, L. Yu, K. Gao, X. Kang, Y. Song, G. Lu and

H.-D. Yu, High-Performance Organic Electrochemical Transistor Based on Photo-annealed Plasmonic Gold Nanoparticle-Doped PEDOT:PSS, *ACS Appl. Mater. Interfaces*, 2023, **15**, 3224–3234, DOI: **10.1021/acsami.2c19867**.

93 Y. J. Lee, Y. H. Kim and E. K. Lee, PEDOT:PSS-Based Prolonged Long-Term Decay Synaptic OECT with Proton-Permeable Material, Nafion, *Macromol. Rapid Commun.*, 2024, **45**, 2400165, DOI: **10.1002/marc.202400165**.

94 L. Zhang, S. Khayour, G. Ren, S. He, J. Wang, L. Yu, Y. Song, C. Zhu, X. Kang, Y. Zhang, Z. Gong, K. Gao, J. Wang, H. Sheng, G. Lu and H.-D. Yu, Proton-penetrable Nafion-induced phase separation in organic semiconductors for high-performance organic electrochemical transistors, *J. Mater. Chem. C*, 2023, **11**, 7272–7282, DOI: **10.1039/D3TC01194A**.

95 P. Xu, C. Lu, D. Wang and D. Fu, Combination of ultrathin micro-patterned MXene and PEDOT:Poly(styrenesulfonate) enables organic electrochemical transistor for amperometric determination of survivin protein in children osteosarcoma, *Microchim. Acta*, 2021, **188**, 301, DOI: **10.1007/s00604-021-04947-2**.

96 R. Lucklum and P. Hauptmann, The quartz crystal microbalance: mass sensitivity, viscoelasticity and acoustic amplification, *Sens. Actuators, B*, 2000, **70**, 30–36, DOI: **10.1016/S0925-4005(00)00550-5**.

97 I. R. Jang and H. J. Kim, Short Review on Quartz Crystal Microbalance Sensors for Physical, Chemical, and Biological Applications, *J. Sens. Sci. Technol.*, 2022, **31**, 389–396, DOI: **10.46670/JSST.2022.31.6.389**.

98 J. S. R. Hartz, N. W. Emanetoglu, C. Howell and J. F. Vetelino, Lateral field excited quartz crystal microbalances for biosensing applications, *Biointerphases*, 2020, **15**, 030801, DOI: **10.1116/6.0000144**.

99 D. Johannsmann, A. Langhoff and C. Leppin, Studying Soft Interfaces with Shear Waves: Principles and Applications of the Quartz Crystal Microbalance (QCM), *Sensors*, 2021, **21**, 3490, DOI: **10.3390/s21103490**.

100 N. Alanazi, M. Almutairi and A. N. Alodhayb, A Review of Quartz Crystal Microbalance for Chemical and Biological Sensing Applications, *Sens. Imaging*, 2023, **24**, 10, DOI: **10.1007/s11220-023-00413-w**.

101 S. Na Songkhla and T. Nakamoto, Overview of Quartz Crystal Microbalance Behavior Analysis and Measurement, *Chemosensors*, 2021, **9**, 350, DOI: **10.3390/chemosensors9120350**.

102 X. Huang, Q. Chen, W. Pan and Y. Yao, Advances in the Mass Sensitivity Distribution of Quartz Crystal Microbalances: A Review, *Sensors*, 2022, **22**, 5112, DOI: **10.3390/s22145112**.

103 M. Pohanka, Quartz Crystal Microbalance (QCM) Sensing Materials in Biosensors Development, *Int. J. Electrochem. Sci.*, 2021, **16**, 211220, DOI: **10.20964/2021.12.15**.

104 S. Ju, C. Zhang, P. Zahedinejad and H. Zhang, SC-Cut Quartz Resonators for Dynamic Liquid Viscosity Measurements, *IEEE Trans. Ultrason., Ferroelect., Freq. Contr.*, 2021, **68**, 3616–3623, DOI: **10.1109/TUFFC.2021.3096782**.

105 P. A. Topart, M. A. M. Noël and H.-D. Liess, High frequency impedance analysis of quartz crystal microbalances coated with conducting polymers, *Thin Solid Films*, 1994, **239**, 196–204, DOI: **10.1016/0040-6090(94)90851-6**.

106 F. Josse, Y. Lee, S. J. Martin and R. W. Cernosek, Analysis of the Radial Dependence of Mass Sensitivity for Modified-Electrode Quartz Crystal Resonators, *Anal. Chem.*, 1998, **70**, 237–247, DOI: **10.1021/ac9706032**.

107 W. Pan, X. Huang and Q. Chen, Analysis of the Uniformization of the QCM Mass Sensitivity Distribution through a Dot Multiring Electrode Structure, *Anal. Chem.*, 2021, **93**, 16828–16834, DOI: **10.1021/acs.analchem.1c03443**.

108 S. J. Martin, K. O. Wessendorf, C. T. Gebert, G. C. Frye, R. W. Cernosek, L. Casaus and M. A. Mitchell, Measuring liquid properties with smooth- and textured-surface resonators, in 1993 IEEE International Frequency Control Symposium, IEEE, Salt Lake City, UT, USA, 1993, pp. 603–608.

109 W. Pan, X.-H. Huang, Q. Chen, Z.-C. Fan and Y. Xu, Analysis and Verification of the Relationship between the Maximum Mass Sensitivity of Quartz Crystal Microbalance and Electrode Parameters, *Chin. Phys. Lett.*, 2019, **36**, 070701, DOI: **10.1088/0256-307X/36/7/070701**.

110 J. Liang, D. Kong and C. Liu, Study on Dual Channel Lateral Field Excitation Quartz Crystal Microbalance for Measuring Liquid Electrical Properties, *Sensors*, 2019, **19**, 1253, DOI: **10.3390/s19051253**.

111 M. Baù, M. Ferrari and V. Ferrari, Analysis and Validation of Contactless Time-Gated Interrogation Technique for Quartz Resonator Sensors, *Sensors*, 2017, **17**, 1264, DOI: **10.3390/s17061264**.

112 F. R. Lack, G. W. Willard and I. E. Fair, Some Improvements in Quartz Crystal Circuit Elements, *Bell Syst. Tech. J.*, 1934, **13**, 453–463, DOI: **10.1002/j.1538-7305.1934.tb00674.x**.

113 in *Acoustic wave sensors: theory, design, and physico-chemical applications, Acoustic wave sensors: theory, design, and physico-chemical applications*, ed. D. S. Ballantine, Academic Press, San Diego, 1997.

114 C. Behling, R. Lucklum and P. Hauptmann, The non-gravimetric quartz crystal resonator response and its application for determination of polymer shear modulus, *Meas. Sci. Technol.*, 1998, **9**, 1886–1893, DOI: **10.1088/0957-0233/9/11/014**.

115 R. Lucklum and P. Hauptmann, Transduction mechanism of acoustic-wave based chemical and biochemical sensors, *Meas. Sci. Technol.*, 2003, **14**, 1854–1864, DOI: **10.1088/0957-0233/14/11/002**.

116 R. Lucklum, C. Behling and P. Hauptmann, Role of Mass Accumulation and Viscoelastic Film Properties for the Response of Acoustic-Wave-Based Chemical Sensors, *Anal. Chem.*, 1999, **71**, 2488–2496, DOI: **10.1021/ac981245l**.

117 R. Lucklum, C. Behling, R. W. Cernosek and S. J. Martin, Determination of complex shear modulus with thickness shear mode resonators, *J. Phys. D: Appl. Phys.*, 1997, **30**, 346–356, DOI: **10.1088/0022-3727/30/3/006**.

118 G. Sauerbrey, Verwendung von Schwingquarzen zur Wagung dunner Schichten und zur Mikrowagung, *Z. Physik*, 1959, **155**, 206–222, DOI: **10.1007/BF01337937**.

119 K. K. Kanazawa and J. G. Gordon, Frequency of a quartz microbalance in contact with liquid, *Anal. Chem.*, 1985, **57**, 1770–1771, DOI: **10.1021/ac00285a062**.

120 M. Meléndez, A. Vázquez-Quesada and R. Delgado-Buscalioni, Load Impedance of Immersed Layers on the Quartz Crystal Microbalance: A Comparison with Colloidal Suspensions of Spheres, *Langmuir*, 2020, **36**, 9225–9234, DOI: **10.1021/acs.langmuir.0c01429**.

121 M. V. Voinova, Modelling of the response of acoustic piezoelectric resonators in biosensor applications – Part 1: the general theoretical analysis, *J. Sens. Sens. Syst.*, 2015, **4**, 137–142, DOI: **10.5194/jsss-4-137-2015**.

122 A. Oseev, N. Mukhin, C. Elie-Caille, W. Boireau, R. Lucklum, T. Lecompte, F. Remy-Martin, J.-F. Manceau, F. Chollet and T. Leblois, Topology Challenge for the Assessment of Living Cell Deposits with Shear Bulk Acoustic Biosensor, *Nanomaterials*, 2020, **10**, 2079, DOI: **10.3390/nano10102079**.

123 M. Rodahl, F. Höök, C. Fredriksson, C. A. Keller, A. Krozer, P. Brzezinski, M. Voinova and B. Kasemo, Simultaneous frequency and dissipation factor QCM measurements of biomolecular adsorption and cell adhesion, *Faraday Disc.*, 1997, **107**, 229–246, DOI: **10.1039/a703137h**.

124 N.-J. Cho, C. W. Frank, B. Kasemo and F. Höök, Quartz crystal microbalance with dissipation monitoring of supported lipid bilayers on various substrates, *Nat. Protoc.*, 2010, **5**, 1096–1106, DOI: **10.1038/nprot.2010.65**.

125 G. G. Muñoz, M. J. Millicovsky, J. M. Reta, J. I. Cerrudo, A. Peñalva, M. Machtey, R. M. Torres and M. A. Zalazar, Quartz crystal Microbalance with dissipation monitoring for biomedical applications: open source and low cost prototype with active temperature control, *HardwareX*, 2023, **14**, e00416, DOI: **10.1016/j.ohx.2023.e00416**.

126 A. Alassi, M. Benammar and D. Brett, Quartz Crystal Microbalance Electronic Interfacing Systems: A Review, *Sensors*, 2017, **17**, 2799, DOI: **10.3390/s17122799**.

127 I. Plikusiene, V. Maciulis, A. Ramanavicius and A. Ramanaviciene, Spectroscopic Ellipsometry and Quartz Crystal Microbalance with Dissipation for the Assessment of Polymer Layers and for the Application in Biosensing, *Polymers*, 2022, **14**, 1056, DOI: **10.3390/polym14051056**.

128 G. Zhang and C. Wu, Quartz Crystal Microbalance Studies on Conformational Change of Polymer Chains at Interface, *Macromol. Rapid Commun.*, 2009, **30**, 328–335, DOI: **10.1002/marc.200800611**.

129 J. Fang, T. Zhu, J. Sheng, Z. Jiang and Y. Ma, Thickness Dependent Effective Viscosity of a Polymer Solution near an Interface Probed by a Quartz Crystal Microbalance with Dissipation Method, *Sci. Rep.*, 2015, **5**, 8491, DOI: **10.1038/srep08491**.

130 N. Elgrishi, K. J. Rountree, B. D. McCarthy, E. S. Rountree, T. T. Eisenhart and J. L. Dempsey, A Practical Beginner's Guide to Cyclic Voltammetry, *J. Chem. Educ.*, 2018, **95**, 197–206, DOI: **10.1021/acs.jchemed.7b00361**.

131 N. Shpigel, M. D. Levi and D. Aurbach, EQCM-D technique for complex mechanical characterization of energy storage electrodes: background and practical guide, *Energy Storage Mater.*, 2019, **21**, 399–413, DOI: **10.1016/j.ensm.2019.05.026**.

132 C. Cendra, A. Giovannitti, A. Savva, V. Venkatraman, I. McCulloch, A. Salleo, S. Inal and J. Rivnay, Role of the Anion on the Transport and Structure of Organic Mixed Conductors, *Adv. Funct. Mater.*, 2019, **29**, 1807034, DOI: **10.1002/adfm.201807034**.

133 Y. Zhang, Q. Zeng, Y. Shen, L. Yang and F. Yu, Electrochemical Stability Investigations and Drug Toxicity Tests of Electrolyte-Gated Organic Field-Effect Transistors, *ACS Appl. Mater. Interfaces*, 2020, **12**, 56216–56221, DOI: **10.1021/acsami.0c15024**.

134 V. V. Shumyantseva, T. V. Bulko, L. V. Sigolaeva, A. V. Kuzikov and A. I. Archakov, Electrosynthesis and binding properties of molecularly imprinted poly-*o*-phenylenediamine for selective recognition and direct electrochemical detection of myoglobin, *Biosens. Bioelectron.*, 2016, **86**, 330–336, DOI: **10.1016/j.bios.2016.05.101**.

135 J. Wu, S. Wei and S. Luo, *In Situ* Probing Unusual Protein Adsorption Behavior on Electrified Zwitterionic Conducting Polymers, *Adv. Mater. Interfaces*, 2020, **7**, 2000470, DOI: **10.1002/admi.202000470**.

136 M. Wang, J. Fan, M. Bilodeau-Calame, C. Kim, C.-L. Chiang, A. F. C. Segura, V. Vurro, I. Bargigia, J. Mauzeroll and F. Cicoira, Robust and flexible organic electrochemical transistors enabled by electropolymerized PEDOT, *npj Flex Electron.*, 2025, **9**, 74, DOI: **10.1038/s41528-025-00457-w**.

137 Y. Wang, W. Shan, H. Li, Y. Zhong, S. Wustoni, J. Uribe, T. Chang, V. E. Musteata, T. C. H. Castillo, W. Yue, H. Ling, N. El-Atab and S. Inal, An optoelectrochemical synapse based on a single-component n-type mixed conductor, *Nat. Commun.*, 2025, **16**, 1615, DOI: **10.1038/s41467-025-56814-w**.

138 L. Zhang, Y. Kuang, G. Ye and J. Liu, Tailoring the Density of State of n-Type Conjugated Polymers through Solvent Engineering for Organic Electrochemical Transistors, *ACS Appl. Mater. Interfaces*, 2024, **16**, 39693–39700, DOI: **10.1021/acsami.4c04917**.

139 D. Priyadarshini, C. Li, R. Rilemark, T. Abrahamsson, M. J. Donahue, X. Strakosas, F. Ek, R. Olsson, C. Musumeci, S. Fabiano, M. Berggren, E. Olsson, D. T. Simon and J. Y. Gerasimov, Tuning the Organic Electrochemical Transistor (OECT) Threshold Voltage with Monomer Blends, *Adv. Electron. Mater.*, 2024, 2400681, DOI: **10.1002/aelm.202400681**.

140 T. C. Hidalgo Castillo, W. Shan, G. Ma, H. Zhao, Y. Wang, V. Druet, A. Saleh, X. Gu and S. Inal, Thermal Annealing for High Performance and Memory Behavior in n-Type Organic Electrochemical Transistors, *Adv. Mater.*, 2025, **37**, 2411214, DOI: **10.1002/adma.202411214**.

141 B. Ding, V. Le, H. Yu, G. Wu, A. V. Marsh, E. Gutiérrez-Fernández, N. Ramos, M. Rimmele, J. Martín, J. Nelson, A. F. Paterson and M. Heeney, Development of Synthetically Accessible Glycolated Polythiophenes for High-Performance Organic Electrochemical Transistors, *Adv. Electron. Mater.*, 2024, **10**, 2300580, DOI: **10.1002/aelm.202300580**.

142 M. M. Durbin, A. H. Balzer, J. R. Reynolds, E. L. Ratcliff, N. Stingelin and A. M. Österholm, Role of Side-Chain Free Volume on the Electrochemical Behavior of Poly(propylenedioxythiophenes), *Chem. Mater.*, 2024, **36**, 2634–2641, DOI: **10.1021/acs.chemmater.3c02122**.

143 E. Zeglio, Y. Wang, S. Jain, Y. Lin, A. E. Avila Ramirez, K. Feng, X. Guo, H. Ose, G. Mozolevskis, D. Mawad, W. Yue, M. M. Hamedi and A. Herland, Mixing Insulating Commodity Polymers with Semiconducting n-type Polymers Enables High-Performance Electrochemical Transistors, *Adv. Mater.*, 2024, **36**, 2302624, DOI: **10.1002/adma.202302624**.

144 C. J. Kousseff, S. Wustoni, R. K. S. Silva, A. Lifer, A. Savva, G. L. Frey, S. Inal and C. B. Nielsen, Single-Component Electroactive Polymer Architectures for Non-Enzymatic Glucose Sensing, *Adv. Sci.*, 2024, **11**, 2308281, DOI: **10.1002/advs.202308281**.

145 R. Halaksa, J. H. Kim, K. J. Thorley, P. A. Gilhooly-Finn, H. Ahn, A. Savva, M. Yoon and C. B. Nielsen, The Influence of Regiochemistry on the Performance of Organic Mixed Ionic and Electronic Conductors, *Angew. Chem., Int. Ed.*, 2023, **62**, e202304390, DOI: **10.1002/anie.202304390**.

146 P. Huang, Y. Zhou, E. B. Porter, R. G. Saxena, A. Gomez, M. Ykema, N. L. Senehi, D. Lee, C. Tseng, P. J. Alvarez, Y. J. Tao, Y. Li and R. Verduzco, Organic Electrochemical Transistors functionalized with Protein Minibinders for Sensitive and Specific Detection of SARS-CoV-2, *Adv. Mater. Interfaces*, 2023, **10**, 2202409, DOI: **10.1002/admi.202202409**.

147 S. Qian, S. Zhang, D. Chen, J. Wang, W. Wu, S. Zhang, Z. Geng, Y. He and B. Zhu, Phosphorylcholine-Functionalized PEDOT-Gated Organic Electrochemical Transistor Devices for Ultra-Specific and Sensitive C-Reactive Protein Detection, *Polymers*, 2023, **15**, 3739, DOI: **10.3390/polym15183739**.

148 X. Teng, J. Sun, J. Jiang, S. Ke, J. Li, Z. Lou, Y. Hou, Y. Hu and F. Teng, Ion effects on salt-in-water electrolyte gated polymer electrochemical transistors, *Org. Electron.*, 2023, **120**, 106859, DOI: **10.1016/j.orgel.2023.106859**.

149 Z. Sun, B. Khau, H. Dong, C. J. Takacs, S. Yuan, M. Sun, B. Mosevitzky Lis, D. Nguyen and E. Reichmanis, Carboxyl-Alkyl Functionalized Conjugated Polyelectrolytes for High Performance Organic Electrochemical Transistors, *Chem. Mater.*, 2023, **35**, 9299–9312, DOI: **10.1021/acs.chemmater.3c02103**.

150 J. Tropp, D. Meli, R. Wu, B. Xu, S. B. Hunt, J. D. Azoulay, B. D. Paulsen and J. Rivnay, Revealing the Impact of Molecular Weight on Mixed Conduction in Glycolated Polythiophenes through Electrolyte Choice, *ACS Mater. Lett.*, 2023, **5**, 1367–1375, DOI: **10.1021/acsmaterialslett.2c01114**.

151 S. Cong, J. Chen, B. Ding, L. Lan, Y. Wang, C. Chen, Z. Li, M. Heeney and W. Yue, Tunable control of the performance of aqueous-based electrochemical devices by post-polymerization functionalization, *Mater. Horiz.*, 2023, **10**, 3090–3100, DOI: **10.1039/D3MH00418J**.

152 D. Ohayon, D. Renn, S. Wustoni, K. Guo, V. Druet, A. Hama, X. Chen, I. P. Maria, S. Singh, S. Griggs, B. C. Schroeder, M. Rueping, I. McCulloch and S. Inal, Interactions of Catalytic Enzymes with n-Type Polymers for High-Performance Metabolite Sensors, *ACS Appl. Mater. Interfaces*, 2023, **15**, 9726–9739, DOI: **10.1021/acsami.2c20502**.

153 V. Druet, D. Ohayon, C. E. Petoukhoff, Y. Zhong, N. Alshehri, A. Koklu, P. D. Nayak, L. Salvigni, L. Almulla, J. Surgailis, S. Griggs, I. McCulloch, F. Laquai and S. Inal, A single n-type semiconducting polymer-based photo-electrochemical transistor, *Nat. Commun.*, 2023, **14**, 5481, DOI: **10.1038/s41467-023-41313-7**.

154 J. Shi, P. Li, X.-Y. Deng, J. Xu, Z. Huang, Y. Lei, Y. Wang, J.-Y. Wang, X. Gu and T. Lei, Revealing the Role of Polaron Distribution on the Performance of n-Type Organic Electrochemical Transistors, *Chem. Mater.*, 2022, **34**, 864–872, DOI: **10.1021/acs.chemmater.1c04037**.

155 G. E. Fenoy, J. Scotto, J. A. Allegretto, E. Piccinini, A. L. Cantillo, W. Knoll, O. Azzaroni and W. A. Marmisollé, Layer-by-Layer Assembly Monitored by PEDOT-Polyamine-Based Organic Electrochemical Transistors, *ACS Appl. Electron. Mater.*, 2022, **4**, 5953–5962, DOI: **10.1021/acsaelm.2c01124**.

156 I. P. Maria, S. Griggs, R. B. Rashid, B. D. Paulsen, J. Surgailis, K. Thorley, V. N. Le, G. T. Harrison, C. Combe, R. Hallani, A. Giovannitti, A. F. Paterson, S. Inal, J. Rivnay and I. McCulloch, Enhancing the Backbone Coplanarity of n-Type Copolymers for Higher Electron Mobility and Stability in Organic Electrochemical Transistors, *Chem. Mater.*, 2022, **34**, 8593–8602, DOI: **10.1021/acs.chemmater.2c01552**.

157 D. Jeong, I. Jo, S. Lee, J. H. Kim, Y. Kim, D. Kim, J. R. Reynolds, M. Yoon and B. J. Kim, High-Performance n-Type Organic Electrochemical Transistors Enabled by Aqueous Solution Processing of Amphiphilicity-Driven Polymer Assembly, *Adv. Funct. Mater.*, 2022, **32**, 2111950, DOI: **10.1002/adfm.202111950**.

158 A. Koklu, S. Wustoni, K. Guo, R. Silva, L. Salvigni, A. Hama, E. Diaz-Galicia, M. Moser, A. Marks, I. McCulloch, R. Grünberg, S. T. Arold and S. Inal, Convection Driven Ultrarapid Protein Detection via Nanobody-Functionalized Organic Electrochemical Transistors, *Adv. Mater.*, 2022, **34**, 2202972, DOI: **10.1002/adma.202202972**.

159 R. M. Thakur, A. D. Easley, S. Wang, Y. Zhang, C. K. Ober and J. L. Lutkenhaus, Real time quantification of mixed ion and electron transfer associated with the doping of poly(3-hexylthiophene), *J. Mater. Chem. C*, 2022, **10**, 7251–7262, DOI: **10.1039/D2TC00001F**.

160 A. A. Szumska, I. P. Maria, L. Q. Flagg, A. Savva, J. Surgailis, B. D. Paulsen, D. Moia, X. Chen, S. Griggs, J. T. Mefford, R. B. Rashid, A. Marks, S. Inal, D. S. Ginger, A. Giovannitti and J. Nelson, Reversible Electrochemical Charging of n-Type Conjugated Polymer Electrodes in Aqueous Electrolytes, *J. Am. Chem. Soc.*, 2021, **143**, 14795–14805, DOI: **10.1021/jacs.1c06713**.

161 I. P. Maria, B. D. Paulsen, A. Savva, D. Ohayon, R. Wu, R. Hallani, A. Basu, W. Du, T. D. Anthopoulos, S. Inal, J. Rivnay, I. McCulloch and A. Giovannitti, The Effect of

Alkyl Spacers on the Mixed Ionic–Electronic Conduction Properties of N-Type Polymers, *Adv. Funct. Mater.*, 2021, **31**, 2008718, DOI: **10.1002/adfm.202008718**.

162 M. Kawan, T. C. Hidalgo, W. Du, A.-M. Pappa, R. M. Owens, I. McCulloch and S. Inal, Monitoring supported lipid bilayers with n-type organic electrochemical transistors, *Mater. Horiz.*, 2020, **7**, 2348–2358, DOI: **10.1039/D0MH00548G**.

163 A. F. Paterson, A. Savva, S. Wustoni, L. Tsetseris, B. D. Paulsen, H. Faber, A. H. Emwas, X. Chen, G. Nikiforidis, T. C. Hidalgo, M. Moser, I. P. Maria, J. Rivnay, I. McCulloch, T. D. Anthopoulos and S. Inal, Water stable molecular n-doping produces organic electrochemical transistors with high transconductance and record stability, *Nat. Commun.*, 2020, **11**, 3004, DOI: **10.1038/s41467-020-16648-0**.

164 P. Schmode, A. Savva, R. Kahl, D. Ohayon, F. Meichsner, O. Dolynchuk, T. Thurn-Albrecht, S. Inal and M. Thelakkat, The Key Role of Side Chain Linkage in Structure Formation and Mixed Conduction of Ethylene Glycol Substituted Polythiophenes, *ACS Appl. Mater. Interfaces*, 2020, **12**, 13029–13039, DOI: **10.1021/acsami.9b21604**.

165 A. Savva, C. Cendra, A. Giugni, B. Torre, J. Surgailis, D. Ohayon, A. Giovannitti, I. McCulloch, E. Di Fabrizio, A. Salleo, J. Rivnay and S. Inal, Influence of Water on the Performance of Organic Electrochemical Transistors, *Chem. Mater.*, 2019, **31**, 927–937, DOI: **10.1021/acs.chemmater.8b04335**.

166 P. Schmode, D. Ohayon, P. M. Reichstein, A. Savva, S. Inal and M. Thelakkat, High-Performance Organic Electrochemical Transistors Based on Conjugated Polyelectrolyte Copolymers, *Chem. Mater.*, 2019, **31**, 5286–5295, DOI: **10.1021/acs.chemmater.9b01722**.

167 A. Savva, D. Ohayon, J. Surgailis, A. F. Paterson, T. C. Hidalgo, X. Chen, I. P. Maria, B. D. Paulsen, A. J. Petty, J. Rivnay, I. McCulloch and S. Inal, Solvent Engineering for High-Performance n-Type Organic Electrochemical Transistors, *Adv. Electron. Mater.*, 2019, **5**, 1900249, DOI: **10.1002/aelm.201900249**.

168 J. Slauf and J. Reboun, Effect of the Gate Electrode/Electrolyte Interface on OECT performance, in 2022 45th International Spring Seminar on Electronics Technology (ISSE), IEEE, Vienna, Austria, 2022, pp. 1–5.

169 S. Yu and E. L. Ratcliff, Tuning Organic Electrochemical Transistor (OECT) Transconductance toward Zero Gate Voltage in the faradaic Mode, *ACS Appl. Mater. Interfaces*, 2021, **13**, 50176–50186, DOI: **10.1021/acsami.1c13009**.

170 F. Bonafè, F. Decataldo, T. Cramer and B. Fraboni, Ionic Solvent Shell Drives Electroactuation in Organic Mixed Ionic–Electronic Conductors, *Adv. Sci.*, 2024, **11**, 2308746, DOI: **10.1002/advs.202308746**.

171 Z. Sun, M. Sun, S. Qin, M. Wang, Y. Zheng, B. Khau, H. Li, T. E. Gartner, C. J. Takacs and E. Reichmanis, Controlling Ion Uptake in Carboxylated Mixed Conductors, *Adv. Mater.*, 2025, **37**, 2414963, DOI: **10.1002/adma.202414963**.

172 J. R. Vélez-Cordero, S. Jonguitud Flores and B. Yáñez Soto, Finite element simulations of quartz crystal microbalances (QCM): from Sauerbrey to fractional viscoelasticity under water, *Phys. Scr.*, 2024, **99**, 115963, DOI: **10.1088/1402-4896/ad82b7**.

173 I. Reviakine, D. Johannsmann and R. P. Richter, Hearing What You Cannot See and Visualizing What You Hear: Interpreting Quartz Crystal Microbalance Data from Solvated Interfaces, *Anal. Chem.*, 2011, **83**, 8838–8848, DOI: **10.1021/ac201778h**.

174 K. Keiji Kanazawa and J. G. Gordon, The oscillation frequency of a quartz resonator in contact with liquid, *Anal. Chim. Acta*, 1985, **175**, 99–105, DOI: **10.1016/S0003-2670(00)82721-X**.

175 S. Wang, F. Li, A. D. Easley and J. L. Lutkenhaus, Real-time insight into the doping mechanism of redox-active organic radical polymers, *Nat. Mater.*, 2019, **18**, 69–75, DOI: **10.1038/s41563-018-0215-1**.

176 M. V. Voinova, M. Rodahl, M. Jonson and B. Kasemo, Viscoelastic Acoustic Response of Layered Polymer Films at Fluid-Solid Interfaces: Continuum Mechanics Approach, *Phys. Scr.*, 1999, **59**, 391–396, DOI: **10.1238/Physica.Regular.059a00391**.

177 K. Sadman, C. G. Wiener, R. A. Weiss, C. C. White, K. R. Shull and B. D. Vogt, Quantitative Rheometry of Thin Soft Materials Using the Quartz Crystal Microbalance with Dissipation, *Anal. Chem.*, 2018, **90**, 4079–4088, DOI: **10.1021/acs.analchem.7b05423**.

178 I. Furikado, J. Forsman and T. Nylander, Particle Adsorption Using a Quartz Crystal Microbalance with Dissipation by Applying a Kelvin–Voigt-Based Viscoelastic Model and the Gauss–Newton Method, *Anal. Chem.*, 2023, **95**, 15286–15292, DOI: **10.1021/acs.analchem.3c02642**.

179 K. R. Shull, M. Taghon and Q. Wang, Investigations of the high-frequency dynamic properties of polymeric systems with quartz crystal resonators, *Biointerphases*, 2020, **15**, 021012, DOI: **10.1116/1.5142762**.

180 R. Van Der Westen, P. K. Sharma, H. De Raedt, I. Vermue, H. C. Van Der Mei and H. J. Busscher, Elastic and viscous bond components in the adhesion of colloidal particles and fibrillated streptococci to QCM-D crystal surfaces with different hydrophobicities using Kelvin–Voigt and Maxwell models, *Phys. Chem. Chem. Phys.*, 2017, **19**, 25391–25400, DOI: **10.1039/C7CP04676F**.

181 T. Li, J. Y. Cheryl Koh, A. Moudgil, H. Cao, X. Wu, S. Chen, K. Hou, A. Surendran, M. Stephen, C. Tang, C. Wang, Q. J. Wang, C. Y. Tay and W. L. Leong, Biocompatible Ionic Liquids in High-Performing Organic Electrochemical Transistors for Ion Detection and Electrophysiological Monitoring, *ACS Nano*, 2022, **16**, 12049–12060, DOI: **10.1021/acsnano.2c02191**.

182 B. Paul Kunnel and S. Demuru, An epidermal wearable microfluidic patch for simultaneous sampling, storage, and analysis of biofluids with counterion monitoring, *Lab Chip*, 2022, **22**, 1793–1804, DOI: **10.1039/D2LC00183G**.

183 R. Giridharagopal, L. Q. Flagg, J. S. Harrison, M. E. Ziffer, J. Onorato, C. K. Luscombe and D. S. Ginger, Electrochemical strain microscopy probes morphology-induced

variations in ion uptake and performance in organic electrochemical transistors, *Nat. Mater.*, 2017, **16**, 737–742, DOI: **10.1038/nmat4918**.

184 N. Shpigel, M. D. Levi, S. Sigalov, L. Daikhin and D. Aurbach, *In Situ* Real-Time Mechanical and Morphological Characterization of Electrodes for Electrochemical Energy Storage and Conversion by Electrochemical Quartz Crystal Microbalance with Dissipation Monitoring, *Acc. Chem. Res.*, 2018, **51**, 69–79, DOI: **10.1021/acs.accounts.7b00477**.

185 T. E. Alexander, L. D. Lozeau and T. A. Camesano, QCM-D characterization of time-dependence of bacterial adhesion, *Cell Surf.*, 2019, **5**, 100024, DOI: **10.1016/j.tcsw.2019.100024**.

186 S. X. Liu and J.-T. Kim, Application of Kevin—Voigt Model in Quantifying Whey Protein Adsorption on Polyethersulfone Using QCM-D, *JALA*, 2009, **14**, 213–220, DOI: **10.1016/j.jala.2009.01.003**.

187 Z. M. Pawlak and A. Denisiewicz, Identification of the Fractional Zener Model Parameters for a Viscoelastic Material over a Wide Range of Frequencies and Temperatures, *Materials*, 2021, **14**, 7024, DOI: **10.3390/ma14227024**.

188 A. El Baroudi, J. Y. Le Pommellec and V. Couanet, Love waves propagation in layered viscoelastic waveguides characterized by a Zener model, *Sens. Actuators, A*, 2024, **369**, 115209, DOI: **10.1016/j.sna.2024.115209**.

189 T. Lima De Sousa, J. Da Silva and J. Tomas Pereira, Statistical analysis of identification of linear viscoelastic models, *Rheol. Acta*, 2024, **63**, 301–318, DOI: **10.1007/s00397-024-01442-2**.

190 F. Tanaka, Viscoelastic Properties of Stimuli-Responsive Transient Polymer Networks, *Macromolecules*, 2024, **57**, 10600–10614, DOI: **10.1021/acs.macromol.4c02222**.

191 E. Sharifzadeh, F. Ader and G. Moradi, Multi-layer structural representation of polymer/particle interphase region based on De Gennes's scaling theory, *J. Reinf. Plast. Compos.*, 2024, 07316844241279685, DOI: **10.1177/07316844241279685**.

192 N. B. Eisele, F. I. Andersson, S. Frey and R. P. Richter, Viscoelasticity of Thin Biomolecular Films: A Case Study on Nucleoporin Phenylalanine-Glycine Repeats Grafted to a Histidine-Tag Capturing QCM-D Sensor, *Biomacromolecules*, 2012, **13**, 2322–2332, DOI: **10.1021/bm300577s**.

193 Y. J. Gagnon, J. C. Burton and C. B. Roth, Physically intuitive continuum mechanics model for quartz crystal microbalance: viscoelasticity of rubbery polymers at MHz frequencies, *J. Polym. Sci.*, 2022, **60**, 244–257, DOI: **10.1002/pol.20210763**.

194 Z. Adamczyk, M. Sadowska and P. Żeliszewska, Applicability of QCM-D for Quantitative Measurements of Nano- and Microparticle Deposition Kinetics: Theoretical Modeling and Experiments, *Anal. Chem.*, 2020, **92**, 15087–15095, DOI: **10.1021/acs.analchem.0c03115**.

195 J. J. J. Gillissen, S. R. Tabaei, J. A. Jackman and N.-J. Cho, A model derived from hydrodynamic simulations for extracting the size of spherical particles from the quartz crystal microbalance, *Analyst*, 2017, **142**, 3370–3379, DOI: **10.1039/C7AN00456G**.

196 M. V. Voinova, M. Jonson and B. Kasemo, On dissipation of quartz crystal microbalance as a mechanical spectroscopy tool, *J. Spectrosc.*, 2004, **18**, 537–544, DOI: **10.1155/2004/591036**.

197 J. Scotto, A. L. Cantillo, E. Piccinini, G. E. Fenoy, J. A. Allegretto, J. M. Piccinini, W. A. Marmisollé and O. Azzaroni, Using Graphene Field-Effect Transistors for Real-Time Monitoring of Dynamic Processes at Sensing Interfaces. Benchmarking Performance against Surface Plasmon Resonance, *ACS Appl. Electron. Mater.*, 2022, **4**, 3988–3996, DOI: **10.1021/acsaelm.2c00624**.

198 S. Yamamoto, R. Miyako, R. Maeda, Y. Ishizaki and M. Mitsuishi, Dip Coating of Water-Resistant PEDOT:PSS Films Based on Physical Crosslinking, *Macro Mater. Eng.*, 2023, **308**, 2300247, DOI: **10.1002/mame.202300247**.

199 J. Zhang, Y. Zhong, H. Jiang, Z. Zhao, H. Wang, R. Wang, Z. Chen, Q. Liang, X. Wang, F. Sun, Y. Xing, X. Duan, H. Li, L. Feng, M. Zhu, H. Sun and G. Wang, Trace Dual-Crosslinkable Additives Enable Direct Microlithography for Enhanced Organic Electrochemical Transistors, *Adv. Mater.*, 2025, 2417452, DOI: **10.1002/adma.202417452**.

200 L. Bynens, K. Zhang, P. Cavassin, A. Goossens, J. Vanderspikken, T. C. H. Castillo, D. Tsokkou, A. Marks, A. Magni, K. Weaver, L. Lutsen, S. Inal, K. Vandewal, N. Banerji and W. Maes, Organic Electrochemical Transistor Channel Materials: Copolymerization Versus Physical Mixing of Glycolated and Alkoxylated Polymers, *Adv. Funct. Mater.*, 2025, 2423913, DOI: **10.1002/adfm.202423913**.

201 C. Z. Salamat, B. Hu, N. Akmanşen-Kalayci, G. Diaz De La Cruz, L. Shu, A. Leon Ruiz, Q. M. Duong, B. C. Thompson, S. R. Narayan, B. J. Schwartz, B. S. Dunn and S. H. Tolbert, The Role of Dynamic Solvent Swelling in Electrochemical Doping of Semiconducting Polymers, *Adv. Mater. Interfaces*, 2025, 2500098, DOI: **10.1002/admi.202500098**.

202 L. Q. Flagg, R. Giridharagopal, J. Guo and D. S. Ginger, Anion-Dependent Doping and Charge Transport in Organic Electrochemical Transistors, *Chem. Mater.*, 2018, **30**, 5380–5389, DOI: **10.1021/acs.chemmater.8b02220**.

203 L. Q. Flagg, C. G. Bischak, R. J. Quezada, J. W. Onorato, C. K. Luscombe and D. S. Ginger, P-Type Electrochemical Doping Can Occur by Cation Expulsion in a High-Performing Polymer for Organic Electrochemical Transistors, *ACS Mater. Lett.*, 2020, **2**, 254–260, DOI: **10.1021/acsmaterialslett.9b00501**.

204 B. D. Paulsen, R. Wu, C. J. Takacs, H. Steinrück, J. Strzalka, Q. Zhang, M. F. Toney and J. Rivnay, Time-Resolved Structural Kinetics of an Organic Mixed Ionic–Electronic Conductor, *Adv. Mater.*, 2020, **32**, 2003404, DOI: **10.1002/adma.202003404**.

205 G. Rebetez, O. Bardagot, J. Affolter, J. Réhault and N. Banerji, What Drives the Kinetics and Doping Level in the Electrochemical Reactions of PEDOT:PSS?, *Adv. Funct. Mater.*, 2022, **32**, 2105821, DOI: **10.1002/adfm.202105821**.

206 S. T. Keene, V. Gueskine, M. Berggren, G. G. Malliaras, K. Tybrandt and I. Zozoulenko, Exploiting mixed conducting polymers in organic and bioelectronic devices, *Phys.*

Chem. Chem. Phys., 2022, **24**, 19144–19163, DOI: **10.1039/D2CP02595G**.

207 E. Mitraka, M. Gryszel, M. Vagin, M. J. Jafari, A. Singh, M. Warczak, M. Mitrakas, M. Berggren, T. Ederth, I. Zozoulenko, X. Crispin and E. D. Głowacki, Electrocatalytic Production of Hydrogen Peroxide with Poly(3,4-ethylenedioxythiophene) Electrodes, *Adv. Sustainable Syst.*, 2019, **3**, 1800110, DOI: **10.1002/adsu.201800110**.

208 R. Kerr, C. Pozo-Gonzalo, M. Forsyth and B. Winther-Jensen, Influence of the Polymerization Method on the Oxygen Reduction Reaction Pathway on PEDOT, *ECS Electrochem. Lett.*, 2013, **2**, F29–F31, DOI: **10.1149/2.010303eel**.

209 M. Vagin, V. Gueskine, E. Mitraka, S. Wang, A. Singh, I. Zozoulenko, M. Berggren, S. Fabiano and X. Crispin, Negatively-Doped Conducting Polymers for Oxygen Reduction Reaction, *Adv. Energy Mater.*, 2021, **11**, 2002664, DOI: **10.1002/aenm.202002664**.

210 M. Fabretto, M. Müller, C. Hall, P. Murphy, R. D. Short and H. J. Griesser, In situ QCM-D analysis reveals four distinct stages during vapour phase polymerisation of PEDOT thin films, *Polymer*, 2010, **51**, 1737–1743, DOI: **10.1016/j.polymer.2010.02.019**.

211 K. Krukiewicz, B. Bednarczyk-Cwynar, R. Turczyn and J. K. Zak, EQCM verification of the concept of drug immobilization and release from conducting polymer matrix, *Electrochim. Acta*, 2016, **212**, 694–700, DOI: **10.1016/j.electacta.2016.07.055**.

212 I. Efimov, S. Winkels and J. W. Schultze, EQCM study of electropolymerization and redox cycling of 3,4-polyethylenedioxythiophene, *J. Electroanal. Chem.*, 2001, **499**, 169–175, DOI: **10.1016/S0022-0728(00)00358-2**.

213 L. Pigani, A. Heras, Á. Colina, R. Seeber and J. López-Palacios, Electropolymerisation of 3,4-ethylenedioxythiophene in aqueous solutions, *Electrochem. Commun.*, 2004, **6**, 1192–1198, DOI: **10.1016/j.elecom.2004.09.021**.

214 L. Ouyang, B. Wei, C. Kuo, S. Pathak, B. Farrell and D. C. Martin, Enhanced PEDOT adhesion on solid substrates with electrografted P(EDOT-NH_2), *Sci. Adv.*, 2017, **3**, e1600448, DOI: **10.1126/sciadv.1600448**.

215 A. Takemoto, T. Araki, K. Nishimura, M. Akiyama, T. Uemura, K. Kiriyama, J. M. Koot, Y. Kasai, N. Kurihira, S. Osaki, S. Wakida, J. M. J. Den Toonder and T. Sekitani, Fully Transparent, Ultrathin Flexible Organic Electrochemical Transistors with Additive Integration for Bioelectronic Applications, *Adv. Sci.*, 2023, **10**, 2204746, DOI: **10.1002/advs.202204746**.

216 Y. Wang, E. Zeglio, H. Liao, J. Xu, F. Liu, Z. Li, I. P. Maria, D. Mawad, A. Herland, I. McCulloch and W. Yue, Hybrid Alkyl–Ethylene Glycol Side Chains Enhance Substrate Adhesion and Operational Stability in Accumulation Mode Organic Electrochemical Transistors, *Chem. Mater.*, 2019, **31**, 9797–9806, DOI: **10.1021/acs.chemmater.9b03798**.

217 K. M. Persson, R. Gabrielsson, A. Sawatdee, D. Nilsson, P. Konradsson and M. Berggren, Electronic Control over Detachment of a Self-Doped Water-Soluble Conjugated Polyelectrolyte, *Langmuir*, 2014, **30**, 6257–6266, DOI: **10.1021/la500693d**.

218 P. J. Molino, Z. Yue, B. Zhang, A. Tibbens, X. Liu, R. M. I. Kapsa, M. J. Higgins and G. G. Wallace, Influence of Biodopants on PEDOT Biomaterial Polymers: Using QCM-D to Characterize Polymer Interactions with Proteins and Living Cells, *Adv. Mater. Interfaces*, 2014, **1**, 1300122, DOI: **10.1002/admi.201300122**.

219 T.-Y. Lin, W.-Y. Lo, T.-Y. Kao, C.-H. Lin, Y.-K. Wu and S.-C. Luo, Manipulating the distribution of surface charge of PEDOT toward zwitterion-like antifouling properties, *Polymer*, 2022, **262**, 125507, DOI: **10.1016/j.polymer.2022.125507**.

220 C.-H. Lin, C.-Y. Wang, J.-R. Li and S.-C. Luo, Nanostructured Effect on Antifouling Conducting Polymers through Interfacial Adhesive Interaction and Protein Adsorption, *ACS Appl. Polym. Mater.*, 2023, **5**, 10105–10115, DOI: **10.1021/acsapm.3c01964**.

221 C.-H. Lin, X. Tang, P. Chen and S.-C. Luo, Unraveling the Adhesion Behavior of Different Cell Lines on Biomimetic PEDOT Interfaces: The Role of Surface Morphology and Antifouling Properties, *ACS Appl. Bio Mater.*, 2023, **6**, 5695–5707, DOI: **10.1021/acsabm.3c00833**.

222 D. Ohayon, G. Nikiforidis, A. Savva, A. Giugni, S. Wustoni, T. Palanisamy, X. Chen, I. P. Maria, E. Di Fabrizio, P. M. F. J. Costa, I. McCulloch and S. Inal, Biofuel powered glucose detection in bodily fluids with an n-type conjugated polymer, *Nat. Mater.*, 2020, **19**, 456–463, DOI: **10.1038/s41563-019-0556-4**.

223 X. Strakosas, M. J. Donahue, A. Hama, M. Braendlein, M. Huerta, D. T. Simon, M. Berggren, G. G. Malliaras and R. M. Owens, Biostack: Nontoxic Metabolite Detection from Live Tissue, *Adv. Sci.*, 2022, **9**, 2101711, DOI: **10.1002/advs.202101711**.

